POLITECNICO DI MILANO
School of Industrial and Information Engineering
Master of Science in Engineering Physics

POLITECNICO
MILANO 1863

Attosecond transient reflectivity spectroscopy for the study of electron dynamics in diamond

Supervisor:
Prof. Mauro NISOLI
Co-Supervisor:
Dr. Matteo LUCCHINI

Author:
Agata AZZOLIN
(940001)

Academic year 2020-2021

to my Family

Abstract

Thanks to the brilliant results obtained in the previous years, attoscience has shown its potential in unveiling electronic dynamics in matter with unprecedented time resolution. Transient absorption spectroscopy is now a well-established technique, however, it presents some major limitations for the investigation of condensed matter, that can be overcome by studying transient reflectance. In this work, I will present and discuss transient reflectivity measurements on a prototype insulator that is the monocrystalline diamond, starting from a theoretical characterization of the reflectivity and transmission of a pulse at a plane interface without plane-wave approximation, up to the description of the experiment itself and some preliminary considerations on the results obtained, passing through the definitions of the key parameters for a transient reflectivity experiment, i.e. the angle of incidence and the complex refractive index of the sample. Special consideration is reserved also to the description of the setup and the characterization of the polarization state of the IR pulse involved in the experiments.

Grazie ai brillanti risultati ottenuti negli scorsi anni, la scienza degli attosecondi ha mostrato tutto il suo potenziale nel rendere osservabili dinamiche elettroniche in atomi, molecole e solidi con una risoluzione temporale senza precedenti. La spettroscopia in assorbimento transiente è ormai una tecnica consolidata, tuttavia, presenta alcune grandi limitazioni nello studio dei solidi, che possono essere superate studiando la riflettività transiente. In questo lavoro, presenterò e discuterò alcune misure di riflettività transiente in un isolante modello, ovvero il diamante monocristallino, iniziando da una descrizione teorica della riflessione e trasmissione di un impulso su un'interfaccia piana senza approssimazione di onda piana, fino alla descrizione dell'esperimento in sé e alcune considerazioni preliminari sui risultati ottenuti, passando per la definizione dei parametri chiave in un esperimento di riflettività transiente, ovvero l'angolo di incidenza e l'indice di rifrazione complesso del campione. Particolare attenzione è riservata anche alla descrizione del setup e alla caratterizzazione della polarizzazione dell'impulso IR usato negli esperimenti.

Summary

The access to a direct observation of the electron dynamics in the attosecond timescale (10^{-18} s) has been possible thanks to the discovery and then, the exploitation, of a non-linear phenomenon: the *high-order harmonic generation (HHG)*. In the 2000s, this led to the first attosecond transient absorbance experiments, few of them regarding condensed matter and considered as pioneering, will be illustrated in the first chapter of this work, together with a detailed description of the HHG process. The thesis focuses on the attosecond transient reflectivity spectroscopy (ATRS), a relatively new technique which presents major advantages with respect to transient absorption spectroscopy, even though it is technically challenging and theoretically more complex. In particular, I will concentrate on its application to the study of electron dynamics in diamond. One of the ATRS complexity is given by the proper choice of the angle of incidence on the sample, that will be discussed in Chapter 5, as a general issue and in relation to the diamond case, that, with respect to other materials already studied, such as Germanium, seems to show a different behaviour. The setup I used for the experiments here reported is anything but standard with respect to other beamlines for ATRS and deserves special consideration. Its double-foci geometry, i.e. two interaction regions, one with a noble gas, and one with the solid sample under investigation, allows to characterize, at the same time, the laser pulses involved in the experiment and to collect a transient reflectance trace from the sample under investigation, calibrating with precision the absolute delay of the dynamics with respect to the pump infrared (IR) laser, which triggers them. Chapter 2 is completely dedicated to the description of the setup. Major upgrades are planned for the beamline, in order to study polarization-dependent dynamics in advanced material, using techniques such as the magnetic circular dichroism spectroscopy (MCD) and the time-resolved magneto-optical Kerr effect (TR-MOKE) spectroscopy. This makes necessary the development of an IR polarimeter, capable of fully characterize the polarization state of the IR laser pulse of the beamline. I dedicated part of the thesis to its development (setup and coding) and testing. The results are shown in Chapter 3 and confirm its efficiency in recognizing different states of polarization with

a sufficient degree of confidence.

Not only working at reflection requires the definitions of parameters not required in absorption, but it makes also necessary a higher degree of control on the laser pulses properties and their behavior at the interface with the sample. A first step going in this direction is provided in this thesis (see Chapter 4) with the description of the interaction of a Gaussian pulse with a plane interface, without using the plane-wave approximation. At the condition of the experiments on diamond (angle of incidence 44.6°), this model shows that the spatial properties of the pulse do not play a role in the reflection and propagation of the pulses, and the plane wave approximation can be considered valid. The model can be further developed in order to take into account the surface roughness at the interface and its effect on reflection/transmission. A possible way to treat this issue is provided in the above-mentioned chapter too.

The last part of the work is dedicated to the analysis of the experimental results obtained from a monocrystalline diamond sample. In particular, the final chapter focuses on the extraction of the energy-dependent phase delay between the observed dynamics in the sample and the IR pump pulse that induces that. Interesting results, in accordance with previous works, are obtained and suggest the observation of the dynamical Franz-Keldysh effect. A first theoretical explanation on the underlying induced physical processes is provided at the end of the chapter, relating it to the band-contribution decomposition of the dielectric function, its energy band structure, and the associated density of states.

To further develop the present work, several steps are planned, starting from a detailed theoretical description of the interaction of the pulses with the sample interface, up to the calculations in support of the experimental results, necessary to confirm the initial hypothesis here formulated and reported. Even though ATRS results are not of immediate application, their importance for the study of condensed matter, including quantum processes, is nowadays unquestionable. The results obtained with this thesis add another piece to this fascinating frame, helping in the comprehension of electron dynamics and effects in condensed matter that is not yet fully disclosed.

Sommario

L'osservazione diretta di dinamiche elettroniche nella scala temporale degli attosecondi (10^{-18} s) è stata resa possibile dalla scoperta e dallo sviluppo di un fenomeno non lineare chiamato *high-order harmonic generation (HHG)*, ovvero generazione di armoniche di ordine elevato. Negli anni 2000, questo ha portato ai primi esperimenti di spettroscopia di assorbimento transiente con una risoluzione temporale inferiore al femtosecondo, alcuni dei quali, considerati pionieristici per lo studio di campioni allo stato solido, saranno illustrati nel primo capitolo di questo lavoro, insieme ad una descrizione dettagliata del processo di HHG. La tesi si concentra sulla spettroscopia di riflessione transiente negli attosecondi (ATRS, secondo l'acronimo inglese di *attosecond transient reflectivity spectroscopy*), una tecnica relativamente nuova che presenta considerevoli vantaggi rispetto a quella di assorbimento, pur essendo tecnicamente complessa e di interpretazione teorica meno diretta, e la sua applicazione allo studio delle dinamiche elettroniche del diamante monoscristallino. Una delle complessità di questa tecnica è data dalla scelta dell'angolo di incidenza della luce laser sul campione, che sarà discussa nel capitolo 5, sia come tematica generale che applicata al diamante. Vedremo che, rispetto ad altri materiali già studiati, come ad esempio il germanio, in diamante l'effetto dell'angolo di incidenza sembra avere un comportamento differente. Il setup utilizzato in questa tesi è tutt'altro che standard rispetto ad altre beamline per ATRS e merita particolare considerazione. Infatti, la sua struttura a doppio fuoco, ovvero le sue due regioni di interazione, una in gas e l'altra con il campione solido, permette contemporaneamente di caratterizzare gli impulsi laser usati e di raccogliere il segnale di riflettività transiente dal campione, calibrando con precisione il ritardo assoluto tra le dinamiche osservate e l'impulso laser IR che le induce. Il capitolo 2 è dedicato interamente alla descrizione del setup. Sono previsti sostanziali upgrade alla linea in modo da poter studiare in materiali innovativi fenomeni dipendenti non solo dalle proprietà temporali e di intensità del fascio laser incidente, ma anche dalla sua polarizzazione, utilizzando tecniche come la spettroscopia di dicroismo magnetico (*magnetic circular dichroism (MCD)*) o la spettrocopia dell'effetto Kerr magneto-ottico risolta in tempo (*time-resolved magneto*

optical Kerr effect (TR-MOKE)). Per questo si è reso necessario lo sviluppo di un polarimetro per radiazione IR, in grado di caratterizzare lo stato di polarizzazione della luce IR incidente utilizzata nella beamline. Ho dedicato parte della tesi al suo sviluppo (setup e programmazione) e ai conseguenti test. I risultati sono riportati al capitolo 3 e confermano la sua efficacia nel riconoscere diversi stati di polarizzazione con un sufficiente grado di confidenza.
Lavorare in riflessione rende necessaria non solo la definizione di parametri non richiesti in assorbimento, ma anche un maggior controllo delle proprietà degli impulsi laser usati e del loro comportamento all'interfaccia con il campione. Un primo passo in questa direzione è fornito in questa tesi (si veda il capitolo 4) con la descrizione dell'interazione di un impulso Gaussiano con un'interfaccia piana, senza considerare l'approssimazione di onda piana. Alle condizioni dell'esperimento sul diamante (angolo di incidenza di 44.6°), il modello mostra che le proprietà spaziali dell'impulso non hanno impatto alcuno sulla sua trasmissione e riflessione e l'approssimazione di onda piana può considerarsi valida. Il modello può essere sviluppato ulteriormente in modo da considerare la rugosità della superficie e il suo effetto sulla riflessione/trasmissione. Un possibile modo di trattare questo punto è fornito alla fine dello stesso capitolo.
La parte finale della tesi è dedicata all'analisi dei risultati sperimentali di ATRS ottenuti da un campione di diamante monocristallino. In particolare, il capitolo finale si concentra sull'estrazione in funzione dell'energia del ritardo di fase tra la dinamica osservata nel materiale e l'impulso IR che la induce. Sono stati ottenuti interessanti risultati, in accordo con precedenti lavori, che sembrano suggerire l'osservazione dell'effetto Franz-Keldysh dinamico. Una prima spiegazione teorica del processo fisico in atto è fornita alla fine del capitolo, sfruttando la decomposizione della funzione dielettrica secondo i contributi delle bande energetiche del diamante e, quindi, della struttura energetica stessa e dell'associata densità di stati.
Per sviluppare ulteriormente il presente lavoro, sono programmati diversi ulteriori passaggi, a partire da una spiegazione teorica dell'interazione degli impulsi con il campione, fino ai calcoli teorici a sostegno dei risultati sperimentali osservati, necessari per confermare le ipotesi iniziali qui riportate riguardo l'interpretazione dei dati ottenuti. Nonostante i risultati della spettroscopia ad attosecondi in riflessione non siano di immediata applicazione, la loro importanza per gli studi sulla materia, inclusi processi quantistici, è ormai indubbia. I risultati di questa tesi si aggiungono a questo affascinante ambito, aiutando nella comprensione di effetti e dinamiche elettroniche nei solidi otticamente indotti, non ancora pienamente descritti e compresi.

Acknowledgements

First of all, I want to thank my supervisors, prof. Mauro Nisoli and Dr. Matteo Lucchini, without them this work would have not been possible, and Dr. Rocìo Borrego-Varillas, who has always been a source of support and inspiration in these years of Master's. My gratitude also to my lab-mates for their valuable suggestions during these months of work.
A special thank to my closest and wonderful friends, who did not hide in some of the worst moments of my life, but showed me the silver lining behind the clouds.
Finally, my greatest thanks goes to my Family (yes, with capital letter as dad knows): not only they support my decisions and the unique shaping of my life, but also teach me everyday to have values and to not sacrifice them.

Contents

1 Attoscience for ultrafast dynamics in solids **1**

1.1 Why attoscience? 1

1.2 High-order harmonic generation process 2

1.3 Attosecond transient spectroscopy in solids 5

1.4 Motivation and structure of this work 7

2 Table-top experimental setup **9**

2.1 Laser source 9

2.2 Beamline for attosecond transient reflection spectroscopy 11

2.2.1 High-order harmonic generation and recombination chambers . 12

2.2.2 Interaction regions: ToF and XUV reflectometer 14

3 Further setup development: polarimeter for IR radiation **17**

3.1 Methods 19

3.1.1 Classic 19

3.1.2 Rotating waveplate 20

3.2 Experimental measurements 21

3.2.1 Setup and data acquisition 21

3.2.2 Data analysis 23

3.2.3 Narrow-band measurements 24

3.2.4 Broad-band measurements 29

4 Pulse interaction at an interface: static reflectivity **31**

4.1 The Fresnel coefficients 31

4.2 Pulse propagation and reflection at a plane interface 32

4.3 IR pulse at vacuum-diamond interface 35

4.4 XUV pulse at vacuum-diamond interface 38

4.5 Surface roughness 41

5 Key parameters for transient reflectivity measurements **43**

5.1 Determination of the angle of incidence 43

5.1.1 Diamond critical angle 46
5.2 Determination of the complex refractive index 48
5.2.1 Reflectivity measurements at Elettra Synchrotron 48

6 Attosecond electron dynamics in diamond **51**
6.1 Attosecond streaking trace 52
6.2 Transient reflectance trace 56
6.3 Extraction of the energy-dependent phase delay 58
6.4 Interpretation of the energy-dependent phase delay 63

Conclusions **67**

Appendix A. Beckmann-Spizzichino model **71**

Bibliography **73**

List of Figures

1.1 Time scales of electronic motion in atomic/molecular systems (upper part) with respect to ΔE and of an electronic ensemble (lower part). [1] 2

1.2 Three-step model scheme. The red line indicates the electric field of the driving laser electric field.[7] 3

1.3 Schematic HHG spectrum. [7] 4

1.4 Example of attosecond transient absorption spectroscopy from [11]: schematic of the setup (left) and absorbance trace as function of the reciprocal delay of IR and XUV pulses and the photon energy (right). 6

1.5 In the first panel the transient absorption signal from GaN oscillating with a periodicity of 860 as, corresponding to three times the driving frequency of the IR field inducing the signal shown in the second panel. Adaptation from [15]. 6

2.1 Simple block scheme of the amplifying system: the oscillator-generated laser pulse (red) enters the stretcher, it is amplified through the three stages (regenerative, preamplifier and booster) pumped by the Etna pump laser (green) and finally reaches the compressor. 10

2.2 Scheme of the generation and recombination stage.[19] 12

2.3 Scheme of the DOG. QP1 and QP2 are the first and second quartz plate, and BBO is the barium borate crystal. Adaptation from [26]. . 13

2.4 Scheme of the two interaction regions, ToF and reflectometer.[19] . . 14

3.1 Generic polarization ellipse. 18

3.2 Classical measurement scheme [38]. 19

3.3 Rotating waveplate measurement scheme [38]. 20

3.4 Picture of the polarimeter setup built and used for the characterization of the IR laser beam of the beamline. The two rotor stages can be seen in line on the left side of the picture, whilst their controllers are on the right side, behind them there is the spectrometer. 22

3.5 Reference system orientation. 23

3.6 IR intensity spectrum measured before temporal compression by hollow-core fiber. The polarimeter optical elements are at 0°. 24
3.7 Stokes parameters retrieved with the classic method at each wavelength for the case of linear horizontal polarization. Dots • correspond to mean values and error bars are associated to $\pm\sigma_{tot}$ intervals. Red dashed lines correspond to the expected theoretical values. 25
3.8 Stokes parameters retrieved with the rotating waveplate method at each wavelength for the case of linear horizontal polarization. Dots • correspond to mean values and error bars are associated to $\pm\sigma_{tot}$ intervals. Red dashed lines correspond to the expected theoretical values. 26
3.9 Theoretical, experimental and fitted curves comparison for the three polarization cases considered in narrow-band pre-fiber measurements. —— fitted, - - - theoretical, • experimental data. Blue horizontal, red circular and green 30° linear polarization. Darker color shade for $\phi = 0$, lighter for $\phi = \pi/2$. 28
3.10 Broad spectrum exiting from the hollow core fiber filled with 0.5 bar of Ne. Polarimeter optical elements set at 0°. 29

4.1 Rotation of the reference system, from $\{x', y', z'\}$ to $\{x, y, z\}$, where z-axis is normal to the interface between medium 1 and medium 2. . . 34
4.2 Generic wave component reaching the interface with an angle θ_i. . . . 34
4.3 Real and imaginary part of the complex refractive index of diamond in the IR spectral range considered. 36
4.4 Temporal profiles of the IR reflected and transmitted pulses at the vacuum-diamond interface. 36
4.5 Spatial profile of the Gaussian IR pulse interacting with the vacuum-diamond interface (located at x=0) given by the superposition of incident, reflected and transmitted pulses. Arrows point the direction of incidence, reflection and transmission. 37
4.6 Real and imaginary parts of the diamond refractive index calculated by S. Sato (2016) and from public databases. 38
4.7 Real and imaginary parts of the diamond refractive index in the XUV spectral range considered. 39
4.8 Peak intensity exponential decay of the XUV pulse in diamond. . . . 39
4.9 Temporal profiles of the XUV reflected and transmitted pulses at the vacuum-diamond interface. 40

5.1 On the left, $|S_{\varepsilon''}|$ as function of the XUV energy and the incident angle and on the right $|S_{\varepsilon'}|$. The black line represents the critical angle at each energy. 45

5.2 Absolute sensitivity functions at 44.6° as function of the energy. . . . 46

5.3 Modulus of the transient reflectivity at 45 eV from diamond as function of the angle of incidence. Red curve and black curve are respectively to a variation in the reflectance with respect to the real and imaginary part of the dielectric function. The dashed light blue line corresponds to the critical angle for 45 eV calculated to be 45.3°. 47

5.4 Static reflectivity (R) of $LaVO_3$ at various angles of incidence with respect to the normal. 49

6.1 (a) Diamond crystal structure, highlighting the tetrahedral bonds. (b) Atomic positions in the cubic cell projected on a cube face: numbers refer to the height of the atom with respect to the cubic edge and colors to the two different interpenetrating fcc lattices. [53] 51

6.2 Schematic representation of the measurement of an attosecond streaking. The XUV probe pulse ionized the atoms generating electrons, which are then subjected to a variation in their momentum caused by the IR field. The change in momentum is the actual observable to be measured. [54] 54

6.3 Photoelectron trace [arb.u.], obtained in Argon with a ToF pressure of $7.7{\cdot}10^{-6}$ mbar, in absence (left) and in presence (right) of the IR pump. 54

6.4 Detail of the streaking trace in Figure 6.3 (right) obtained in Argon (ToF pressure of $7.7{\cdot}10^{-6}$ mbar) with the extracted center of mass (black curve), a good approximation of the IR vector potential. 55

6.5 Raw transient reflectance trace from diamond. It is obtained mediating over 100 acquisition of the XUV camera with an exposure time of 0.2 s. The delay axis spans 10 fs with steps of 250 as. The energy of the IR pulse is set to 30 μJ. 56

6.6 Transient reflectivity trace of Figure 6.5 after the edge-pixel referencing procedure. 57

6.7 Center of mass extracted from the reference streaking trace and filtered around f_0 (left) and its squared modulus (right). The center of mass is a good approximation of the IR vector potential A_{IR}. 59

6.8 Transient reflectance trace of Figure 6.6 filtered around $2f_0$. 59

6.9 Mean value of the phase delay extracted from four measurements (black curve) with the corresponding standard deviation (black shaded area), superimposed to the transient reflectance trace used as reference and reported in Figure 6.8. The two fuchsia lines highlight the V-shape, usually associated to the dynamical Franz-Keldysh effect. . 60

6.10 Illustrated explanation of the dynamical Franz-Keldysh effect in diamond from [57]. *(a)* Two electronic states in the VB and CB whose wavefunctions are periodic Bloch states; absorption occurs only for photon energies higher than the energy gap. *(b)* Effect of an external perturbing field which causes the bending of the energy bands; the electron wavefunctions are now Airy functions. Transitions to the conduction band are possible also for photon energies lower than the energy gap. *(c)* Schematic of the absorption profile in the static case shown in frame *(a)* (black dashed curve), and in case of DFKE (red curve), with non-zero absorption below the energy gap proportional to the ponderomotive energy of the field and oscillations at higher photon energies. *(d)* Diamond band diagram highlighting the transition from band 1 to band 11, the main involved in [11]. When $\gamma_a \approx 1$, the IR field can either accelerate the electron in the same sub-band (intra-band motion) or inject it to another sub-band (inter-band motion). . 61

6.11 Schematic map of the electro-optic phase space as function of the amplitude and frequency of the IR perturbing field. The three different regimes are highlighted ($\gamma = \gamma_a$). Adaptation from [59]. 62

6.12 Block states of diamond (left) and the corresponding density of states (right). Colored curves correspond to the states possibly involved to describe the features observed in the transient reflectance trace. In the valence band (VB), these are states 2, 3, and 4 and in the conduction band (CB), states 9, 10, and 11. Adaptation from [11]. 64

6.13 Decomposition of the imaginary part of the dielectric function into the contribution from each valence band (a) and further decomposition of each valence band (1 to 4) into individual transitions to the conduction states 8 to 15 (b)-(e). Adaptation from [11]. 65

6.14 A plane wave incident on a rough surface with propagation direction $\mathbf{k}_1$ and scattered in direction $\mathbf{k}_2$. [47] 71

List of Tables

3.1 Fundamental measurements for classical polarimetry method. 19
3.2 Stokes parameters of the integrated spectra retrieved with the classic method for the case of linearly horizontally polarized light. 26
3.3 Stokes parameters of the integrated spectra for the case of left circular polarization. 27
3.4 Stokes parameters from fit of the integrated spectra in case of linearly polarized light at -30°. 27
3.5 Fiber in vacuum. Results for integrated spectra. 30
3.6 Fiber filled with Ne gas. Results for integrated spectra. 30

1 | Attoscience for ultrafast dynamics in solids

The topic of this thesis is attosecond spectroscopy of solids, focusing on the study of ultrafast dynamics in a prototype insulator like diamond. In this introductory chapter, I will discuss the relevance of attoscience for the study of condensed matter, the difference between transient absorption and reflectance providing a description of a typical experiment. The structure of this thesis will be illustrated in the last section of this chapter.

1.1 Why attoscience?

Electron motion and dynamics in the microcosm are ruled by the laws of quantum mechanics. A particle in a superposition of two of its states results, from Schrödinger equation, in an oscillatory motion whose period is $T_{osc} = h/\Delta E$, where h is the Planck constant and ΔE is the energy difference between the two levels. Thus, the millielectronvolt-scale energy spacing of vibrational energy levels implies that molecular vibrations occur on a time scale of tens/hundreds femtoseconds, whereas the motion of individual electrons in the atomic orbitals occurs at shorter time intervals ranging from tens of femtosecond to less than an attosecond [1]. The oscillation period previously defined governs also the response time of the particle to an external perturbation. Figure 1.1 from [1] shows the characteristic time scales for electronic motion in an atomic/molecular system (upper part) with respect to ΔE, and for the collective motion of an electronic ensemble (lower part). For the purpose of this thesis, it is worth to highlight once again that the electronic motion in the valence and inner shells corresponds to the kiloelectronvolt-energy and to a time scale ranging from few attoseconds to few femtoseconds.

At this point the question is: how to access electronic motion? And in particular, how to access transitions at tens of eV and with attosecond time scales? The

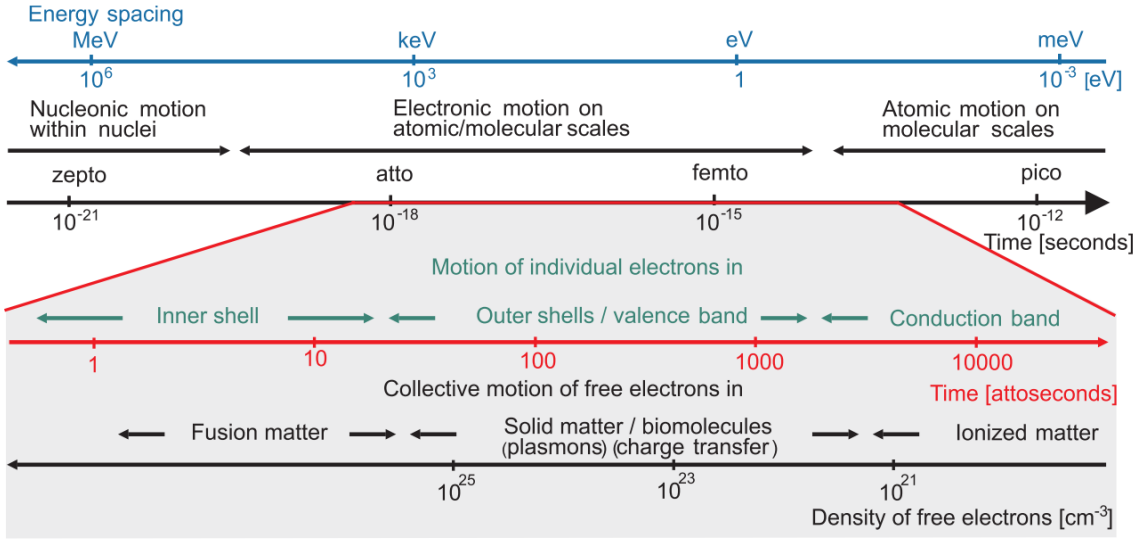

Figure 1.1: *Time scales of electronic motion in atomic/molecular systems (upper part) with respect to ΔE and of an electronic ensemble (lower part). [1]*

discovery of X-rays (W.C. Röntgen, 1895) partially solved the problem: with their short wavelengths (0.01 to 10 nm) and enough energy per photon X-rays are able to access transitions from the core levels of atoms. Synchrotrons are widely used to generate efficiently X-rays, nonetheless, synchrotron radiation has not the temporal properties to access the time scale required to study electronic dynamics; typically, X-rays emitted from sychrotron are trains of 10-100 ps long pulses separated by few nanoseconds [2, 3]. It was only with the advent of free-electron lasers and the discovery of *high-order harmonic generation (HHG)* that this problem has been overcome [3]. Nowadays, HHG is routinely used in laboratories all over the world to generate attosecond pulses in the extreme-ultraviolet energy range. In the next section, I will briefly explain this physical process.

1.2 High-order harmonic generation process

A short (few fs) and intense (10^{13} to 10^{15} W/cm^2) laser pulse can be used to drive the *high-order harmonic generation process (HHG)*: focusing it into a gas medium, thanks to the highly non-linear electronic response of the gas, high-order harmonics of the driving laser frequency can be generated. In our setup, the few-cycle IR laser pulse[1] (intensity $\approx 10^{14}$ W/cm^2 and duration < 10 fs) drives HHG.
This process can be explained through a semiclassical model, called ***three-step***

[1] see Chapter 2

model or *simple man model* [4, 5, 6]. In the first step, there is tunnel ionization of the gas atoms: under the action of the external electric field - the IR driving laser beam-, the Coulomb potential felt by the outer electrons is strongly modified, enhancing the probability of electron emission; the electron can then tunnel out of the potential barrier. The second step consists in the electron acceleration and deceleration caused by the laser electric field until it reaches again the initial position. The third and last step is recollision: the electron have a non-null probability of recolliding with the parent ion and the kinetic energy acquired during the second step is released in form of a burst of high-energy photons with IR sub-cycle duration, i.e. an XUV attosecond pulse [7]. Figure 1.2 summarizes the three steps.

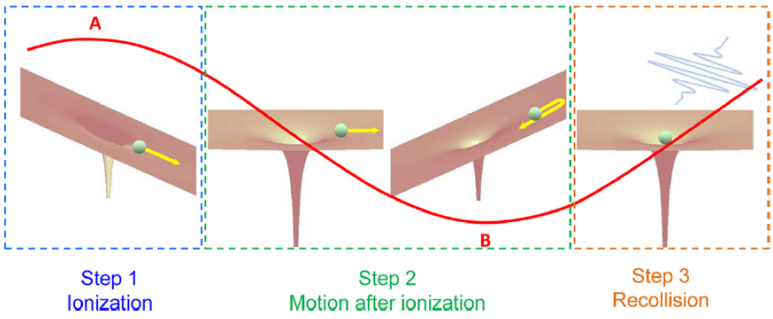

Figure 1.2: *Three-step model scheme. The red line indicates the electric field of the driving laser electric field.[7]*

The three steps are repeated every half optical cycle, since an electron can be freed around any of the field crests, thus leading to the generation of a train of attosecond pulses separated by half optical cycle of the IR driving radiation. Moreover, in a centrosymmetric medium as the gas target, a reversal of the driving field results also in a reversal of the nonlinear polarization, which is the source of the harmonic emission. For these reasons, only odd harmonics can be generated. In fact, considering an IR driving laser electric field of period T and so carrier frequency $\omega_0 = \frac{2\pi}{T}$, the XUV electric field at each period is given by

$$E_{XUV}(t) = E_1(t) - E_1\left(t - \frac{T}{2}\right) \tag{1.1}$$

where E_1 is the electric field of a single pulse emitted. It corresponds to a spectrum

$$A_{XUV}(\omega) = A_1(\omega) - A_1(\omega)e^{-i\omega\frac{T}{2}} \tag{1.2}$$

that in intensity becomes

$$|A_{XUV}(\omega)|^2 = 4\,|A_1(\omega)|^2\,\sin^2\left(\frac{\omega T}{4}\right)\,. \tag{1.3}$$

This intensity spectrum is maximum for

$$\frac{\omega T}{4} = \frac{\pi}{2}(1+2n) \tag{1.4}$$

that can be rewritten as

$$\omega = \frac{2\pi}{T}(1+2n) = \omega_0(1+2n) \ , \tag{1.5}$$

highlighting the presence of only odd harmonics.
A schematic representation of the HHG spectrum can be found in Figure 1.3, showing the plateau region, where intensity is roughly constant, and the cutoff region, where the efficiency of the process drops. From the semiclassical model, one can also derive the maximum photon energy that can be emitted after recollision:

$$\hbar\omega_{X,max} = I_p + 3.17\, U_p \ , \tag{1.6}$$

where I_p is the ionization potential of the atom and U_p is the ponderomotive energy, i.e. the mean kinetic energy of an electron oscillating in a laser field. This can be expressed as

$$U_p = \frac{(eE_0)^2}{4m\omega_0^2} \ , \tag{1.7}$$

where E_0 and ω_0 are, respectively, the amplitude and the angular frequency of the driving field, and e and m the charge and mass of the electron. An alternative formulation is $U_p\ [eV] = 9.33\ 10^{-14}\ I_L\ \lambda_0^2$, with I_L [W/cm^2] intensity of the driving laser and λ_0 [μm] the laser wavelength. This last formulation highlights that the cutoff photon energy can be extended by increasing the wavelength and the intensity. However, an higher intensity can induce saturation (too many atoms are ionized) and longer wavelengths reduce the efficiency of the HHG process [8].

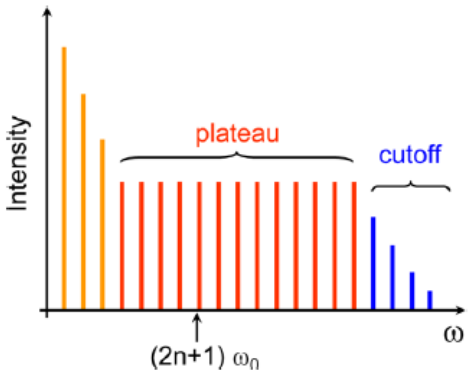

Figure 1.3: *Schematic HHG spectrum. [7]*

All this considered, the HHG process allows to generate pulses in the XUV/soft-X region, from 10 eV up to hundreds of eV, and with typical temporal duration of hundreds of attoseconds. At the present moment, the shortest single attosecond pulse obtained through HHG has a duration of 43 as [9]. Thus, these pulses have the needed temporal and energetic characteristics to access the electronic motion in the inner shells.

1.3 Attosecond transient spectroscopy in solids

The behaviour of an electron in the periodic lattice potential of a crystal is a crucial topic for solid-state physics. To investigate it, the idea is to measure the response of the system to an external stimulus, that can be of different nature (radiative, electrical, thermal). Thus, in a typical experiment, we have a pump source which induces the perturbation of the system and a probe to analyse it. The response of the material manifests in a change in the dielectric function, in case of photon stimulation, or in the heat capacity, in case of heat stimulation. For the reasons mentioned above, broadband and short XUV pulses generated through HHG are good candidates to probe the system, whereas, another pulse, even with different temporal and energetic characteristics, could be used as pump. For instance, strong and intense IR femtosecond pulses can drive nonlinear processes inside the material, as for example, the dynamical Franz-Keldysh effect [10, 11], as well as excitons dynamics [12]. The electronic motion resulting from these nonlinear effects responds at the scale of the optical cycle of the pump electric field, thus an attosecond probe is necessary to observe them.

Probe and pump pulses are focused on the sample controlling their reciprocal time delay. Typically, changes in the dielectric function are studied by measuring the *absorbance* of the XUV beam; for each delay, two transmission spectra are caught, one in presence of the pump, and often called *pump-on* measurement, and one without the pump and as a consequence called *pump-off*. In this way, it is possible to track the evolution of the signal. The transient absorbance, then, is defined as the logarithm of the ratio of the transmitted pump-off intensity and the transmitted pump-on intensity. The works in [11], [13] and [14] are brilliant examples of ***attosecond transient absorption spectroscopy (ATAS)***. For instance, I report in Figure 1.4 (left) the schematic of the experimental setup in [11], with its peculiarity of double-target detection to measure absorbance from diamond and photoelectrons from ionization of the Ne gas. In this experiment, the pump is an IR pulse of 5 fs duration, whilst the

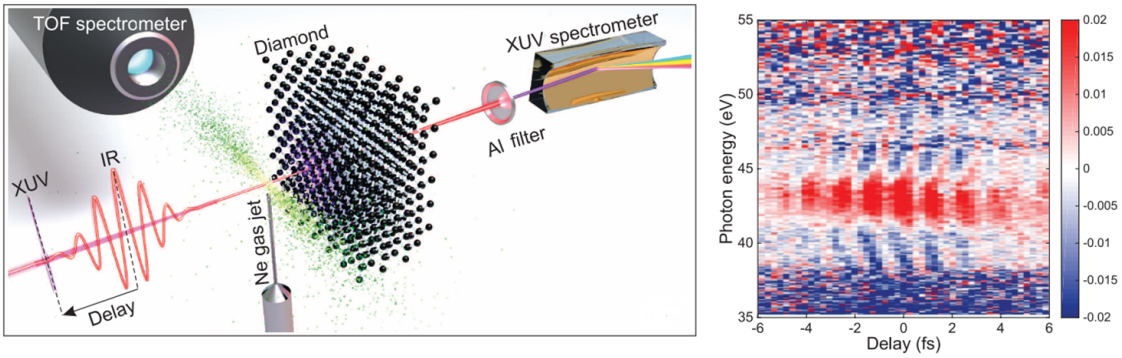

Figure 1.4: *Example of attosecond transient absorption spectroscopy from [11]: schematic of the setup (left) and absorbance trace as function of the reciprocal delay of IR and XUV pulses and the photon energy (right).*

probe is an XUV pulse obtained through HHG in Argon. In the right panel of the same figure, a typical map obtainable from an ATAS measurement, the IR-induced absorbance measured as function of the delay and the photon energy, with clearly visible features between 40 and 45 eV.

It is worth to mention also the work in [15] about gallium nitride (GaN, E_g=3.35 eV), given its peculiarity of probing transitions from the valence/conduction band to the continuum. The absorption oscillates at three times the driving frequency providing clear evidence of three-photon absorption, this frequency corresponds to 1.16 PHz, being the first direct observation of optical driving above 1 petahertz [3]. In Figure 1.5 the transient absorption signal observed with a periodicity of 860 as and, below, the IR field inducing the dynamic.

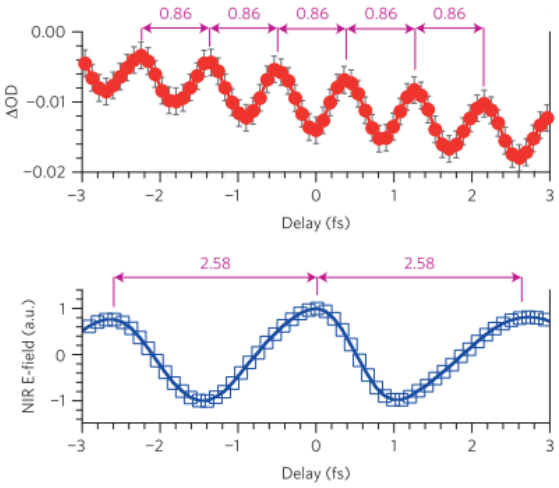

Figure 1.5: *In the first panel the transient absorption signal from GaN oscillating with a periodicity of 860 as, corresponding to three times the driving frequency of the IR field inducing the signal shown in the second panel. Adaptation from [15].*

Even though this technique has made it possible to access and observe several electronic processes in condensed matter, it has a major limitation. In order to measure absorbance, considering that the HHG process generates XUV pulses with low photon flux and that, typically, materials are strong absorbers in this energetic range, the sample must be synthesized as a thin film and this is not always possible. Moreover, the study of absorbance variations give insights only on the imaginary part of the dielectric function, being it directly responsible of absorption. In addition, ATAS is blind to the surface properties of matter, preventing the study of the chemistry of the interfaces [3]. To overcome these limitation, ***attosecond transient reflectivity spectroscopy (ATRS)*** is adopted for the experiments reported in this thesis. First of all, as it will be explained in Chapters 4 and 5, transient reflectivity can access both the real and imaginary part of the dielectric function, leading to a more complete investigation of the sample optical properties. However, it is technically more challenging, requiring, for example, a proper choice of the angle of incidence. Remarkable examples of ATRS are [12] and [16]. ATRS is the technique adopted for the experimental measurements presented in the last chapter of this thesis work and it will be deeply discussed along the chapters.

1.4 Motivation and structure of this work

This thesis work aims to provide an insight into the preparation of an attosecond transient reflectance experiment from the setting to the final measurement. The analyzed sample is diamond, with the underlying idea of continuing the work in [11], providing further insights on the electron dynamics of such crystal in a different energy range, only accessible by studying the sample reflectance.
Chapter 2 is devoted to the description of the setup, highlighting its double-foci geometry, a peculiarity which allows to both characterize pump and probe pulses and measure a transient reflectivity signal from the sample.
Further setup developments are programmed for the beamline in order to study polarization dependent phenomena in advanced materials. For this reason, a complete characterization of the polarization state of the beams it will be necessary. *Chapter 3* describes the development of a polarimeter for IR radiation, from setup to test measurements.
Chapter 4 will be devoted to the analysis of the static reflectivity of a pulse considering its spatial and temporal properties, using the Fresnel equations without any approximation. After a general description and the related calculations, the model is applied to diamond to study the behaviour of both the IR (pump) and the XUV

(probe) pulses at the interface. The study of the static reflectance is indeed a crucial aspect to set and then analyze properly a transient reflectance experiment.
Chapter 5 presents a discussion above two important parameters of a transient reflectance measurement: the angle of incidence and the complex refractive index of the material. Here, the choice of the angle for the experiments on diamond will be discussed in detail. The determination of the angle of incidence depends on the correct determination of the refractive index, which can be experimentally retrieved from static reflectivity measurements as the ones performed by our team at the Elettra Synchrotron in Trieste. One of these measurements will be discussed at the end of the chapter.
Finally, *Chapter 6* contains the experimental results on diamond. Giving that at the moment the theoretical calculations are not yet performed, I will provide a preliminary analysis following the reasoning in [11], giving a few hints for the interpretation of the data and on the possible steps to follow.

2 | Table-top experimental setup

The systems used for attosecond spectroscopy are quite complex as they consist of several parts and involve various technologies, ranging from femtosecond high-power/high-intensity lasers to ultra high vacuum techniques. Their structure can be generally divided into two main sections: an IR laser source and the attosecond pump-probe beamline itself, characteristic of each experiment. The setup at the basis of this thesis is an attosecond transient reflectivity beamline, unique of its kind thanks to its sequential double-foci geometry, which allows direct and live calibration of the pulses, while measuring, at the same time, a reflectivity signal from a sample [17, 18, 19]. In this chapter I will discuss in detail each section which composes the beamline.

2.1 Laser source

The laser source is a 10-kHz, 2-mJ, CEP-stable 800-nm commercial apparatus. It is composed by a Ti:Sapphire mode-locked oscillator (Rainbow, Femtolasers) with average power of 120 mW, whose pulses are amplified through a three-stage chirped-pulse amplification (CPA) system (AURORA, Amplitude Technologies). The amplification system, in turn, is pumped by a high power Nd:YAG Q-switched laser (ETNA HP, Thales), emitting at 532-nm central wavelength with an average power of 130 W.
The CPA process consists of three steps: first, the pulse is stretched to increase its temporal duration, then it is actually amplified in different stages (for the present setup: regenerative, preamplifier, and booster) and, finally, it is compressed in time to ideally restore the transform-limited initial condition [20]. Stretcher and compressor are made of pairs of diffraction gratings combined with a 1:1 inverting telescope: the reciprocal position of these elements allows to introduce either a positive (stretcher) or negative (compressor) dispersion; the geometrical configurations are matched to balance the total dispersion and achieve pulse compression close to the Fourier transform limit. Before the amplification stages, an acousto-optic programmable dispersive filter (AOPDF, Dazzler) is used in feedback loop to fine tune dispersion, through active control of pulse phase and amplitude. A simple block scheme of the amplifying

system is reported in Figure 2.1.

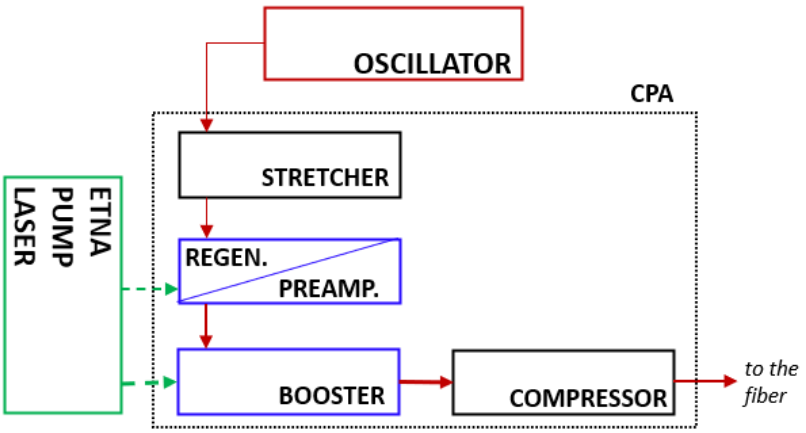

Figure 2.1: *Simple block scheme of the amplifying system: the oscillator-generated laser pulse (red) enters the stretcher, it is amplified through the three stages (regenerative, preamplifier and booster) pumped by the Etna pump laser (green) and finally reaches the compressor.*

The ***regenerative amplifier*** scheme consists of an optical cavity with a gain medium in population inversion, a thin-film polarizer, and a Pockels cell. These two last elements control how many times an external pulse propagates into the gain medium to be amplified. The Pockels cell is a device able to rotate the polarization through electro-optic effect; when the desired amplification level is reached, the device changes the pulse polarization state and the pulse is ejected from the cavity. In this setup, the optimal number of passages in the cavity, before depletion starts, is four; two different Pockels cells are used to control the pulse propagation and the ejection. The gain medium is a Ti:Sapphire, pumped by a fraction of about 13 W of the ETNA pump laser beam and constantly water-cooled. In the cavity is also present an acousto-optic programmable gain control filter (AOPGCF, Mazzler) to prevent the gain-narrowing phenomenon. The regenerative amplification stage leads to an average power up to 1.2 W.

The ***preamplifier*** is a multi-pass amplifier: the pulse propagates four times in a gain medium in population inversion (Ti:Sapphire, water-cooled pumped by a fraction of almost 16 W of the ETNA laser beam) guided by a proper sequence of mirrors. The average power after this stage is almost doubled.

Last, the ***booster stage*** is another multi-pass amplifier, in which the Ti:Sapphire crystal is pumped with the largest fraction ($\approx$ 100 W) of the ETNA pump laser and, for this reason, it is cooled at -180°C with liquid helium. The average power after the booster stage can reach up to 30 W.

Finally, the ***compression stage***, leads typically to 19 W average power pulses of 21 fs duration.
Further temporal compression of the pulses is then obtained through a well-established technique based on two steps: a spectral broadening of the pulse through a fused silica ***hollow-core fiber*** filled with a noble gas and, then, dispersion compensation through ***chirped mirrors*** [21, 22]. The beam coming from the compressor is precisely coupled into the fiber thanks to a beam-pointing stabilization system based on a feedback loop formed by four motor-movable mirrors (Aligna system by TEM Messtechnik). Then, spectral broadening is achieved by exploiting the self-phase modulation (SPM) phenomenon in a noble gas. Self-phase modulation is a third-order non-linear effect: a pulse of intensity I propagating through a material (here, the gas) whose refractive index is $n(t) = n_0 + n_2 I(t)$ (Kerr effect), modulates by itself its own phase $\phi = \omega_c t - \frac{\omega_c}{c} nz$ generating new frequencies, as the instantaneous frequency becomes $\omega(t) = \frac{d\phi}{dt} = \omega_c - \frac{\omega_c n_2 z}{c} \frac{dI}{dt}$. Usually, the fiber is filled with Neon gas at variable pressure; typical values range from 1.5 to 2 bar. The vast majority of the positive group delay dispersion (GDD) is balanced by reflections on the chiriped mirrors (PC70, Ultrafast Inmnovations). Additional glass wedges are used to finely compensate dispersion after chirped mirrors. After this stage, the pulse duration is less than 10 fs and the average power is around 8 W.
The system is equipped also with ***carrier-envelope phase (CEP) stabilization***; however, for the experiments described in the following chapters, this has not been used and for this reason, it will not be discussed here. For details about this point please refer to [18], [19].

2.2 Beamline for attosecond transient reflection spectroscopy

The beamline I used for the attosecond transient reflection experiments shown in this work consists of four components. The first chamber is dedicated to the high-order harmonic generation and it is followed by a separate chamber in which IR and XUV are recombined. The two following chambers correspond to the interactions region, one with a noble gas (time-of-flight spectrometer) and the second with the solid sample under investigation (reflectometer). All the components will be fully described in the following sections.

2.2.1 High-order harmonic generation and recombination chambers

After compression, the short and intense (peak intensity $\approx 10^{14}$ W/cm^2) IR laser pulses can be used to drive the ***high-order harmonic generation (HHG) process***, which is explained in detail in section 1.2.
A scheme of the generation and recombination chambers is reported in Figure 2.2. The IR beam enters the ***generation chamber***. Here it is split through a 30-70

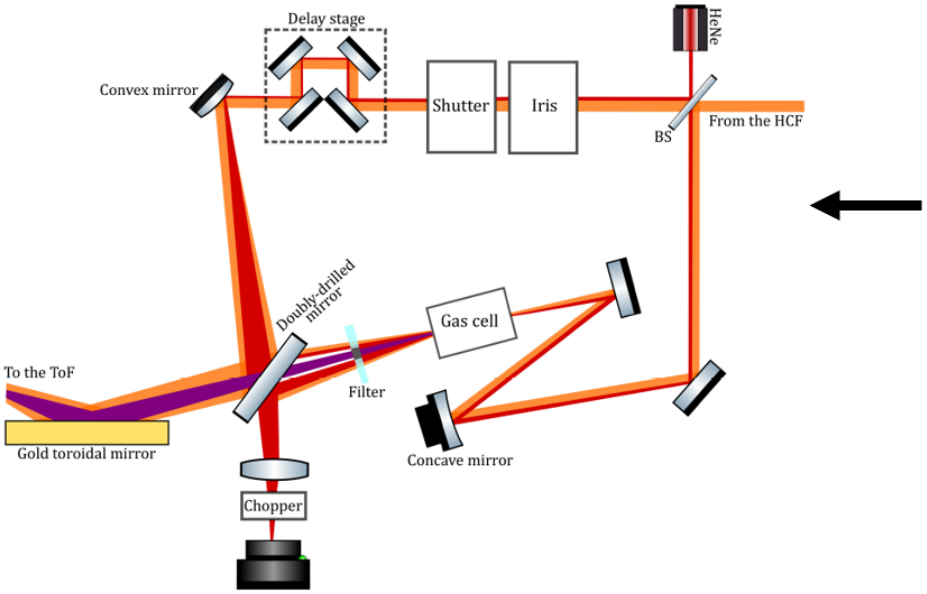

Figure 2.2: *Scheme of the generation and recombination stage.[19]*

beamsplitter: the reflected beam drives HHG and the transmitted one is used for the pump-probe experiment. Motorized irises are used to control the pulse energy on both arms. To realize the HHG process, the most intense part of the laser beam is focused into a gas cell usually filled with Argon. The weakest portion, instead, goes through a mechanical shutter (driven at 1 Hz, to achieve efficient noise subtraction), and reaches the delay line, constituted by a retro-reflector mounted onto a translational stage with nanometric resolution.
Additionally to what is illustrated in [17], for the experiments explained in the next chapter, before the gas cell a ***double optical gating (DOG)*** scheme is introduced [23]. This technique was originally developed to generate isolated attosecond pulses with CEP-stable lasers. It has been shown [24] that by adding a weak second harmonic radiation to the driving laser, the field inversion symmetry can be broken and even harmonics can be generated. Under these conditions, an attosecond pulse is gen-

erated only at positive field crests and thus the periodicity of the attosecond pulse train is the same as the generating IR electric field. Moreover, using the so-called polarization gating technique [25], it is possible to confine the HHG to a single event. The technique exploits the fact that circular polarization does not allow electron-ion recollision, the fundamental third step of HHG. Thus, the polarization is manipulated in such a way that the leading and trailing edges are circularly polarized, whilst the central region is linearly polarized. In this way, the generation of the attosecond pulse is confined to a single event, corresponding to the linearly polarized region. DOG is a combination of these two aspects: while a first birefringent plate at 45° creates two orthogonally polarized delayed replicas of the pulse, a second quartz plate combined with a BBO (barium borate) crystal allows to generate two counter-rotating fields with a second harmonic field polarized parallel to the driving field [26]. A scheme is reported in Figure 2.3. The angles of the two waveplates are adjusted by moving motorized rotor stages, to optimize the HH spectra, aiming at the best compromise between flux and high cutoff energy.

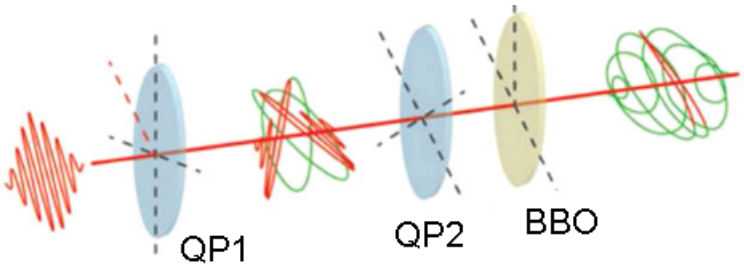

Figure 2.3: *Scheme of the DOG. QP1 and QP2 are the first and second quartz plate, and BBO is the barium borate crystal. Adaptation from [26].*

In a separate chamber, then, the ***recombination*** of the two beams takes place. An aluminum filter removes the residual IR radiation from the XUV beam generated through HHG, then the XUV beam passes through one of the holes of a double drilled mirror at 45° while the IR beam is reflected; collinear recombination is imposed for experiments.

To perform time-resolved experiments with attosecond temporal resolution, very precise relative timing between pump and probe pulses is required. For this reason, an ***active stabilization system*** is implemented. A Helium-Neon (633 nm) frequency-stabilized laser beam enters the recombination chamber through a beamsplitter so that it can follow both the path of the IR and of the XUV up to the double drilled mirror, where the part coming from the XUV direction is reflected from the back and the other one passes through the second hole. The spatial fringes generated by the

recombination are measured with a webcam, placed right after a mechanical chopper suitably synchronized to remove residual IR radiation. Through a PID controller acting on the delay stage, the pump-probe relative delay can be stabilized with a residual root-mean-squared standard deviation of 24 as over a period of 60 minutes.

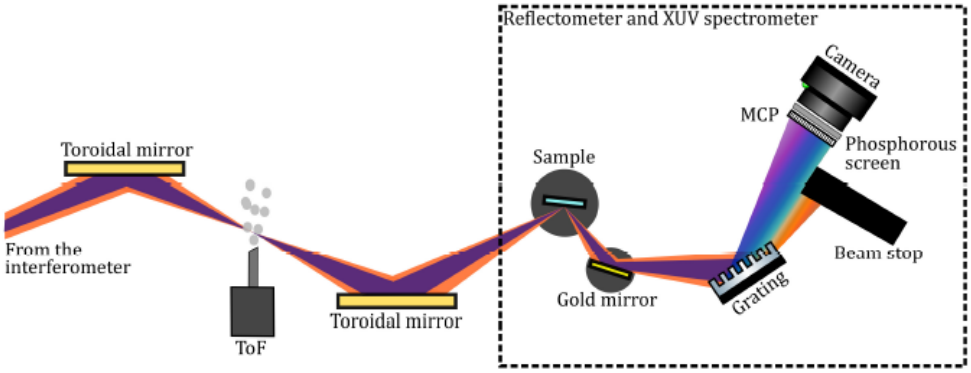

Figure 2.4: *Scheme of the two interaction regions, ToF and reflectometer.[19]*

2.2.2 Interaction regions: ToF and XUV reflectometer

The peculiarity of this attosecond beamline is given by its sequential double-foci geometry, i.e. two different interaction regions in which the XUV and IR beams are focused. The first region is equipped with a time-of-flight (TOF) spectrometer for photoelectron spectroscopy in gas targets. The second focus hosts an XUV reflectometer. The first region is use to precisely characterize both pulses, while the second, at the same time, is used to measure reflectivity signals from solid samples. Moreover, after a precise measurement of the phase delay induced by light propagation between the two foci[1], the beamline enables direct calibration of the absolute pump-probe delay. This means that it is actually possible to access the attosecond timing of the observed dynamics with respect to the IR pump field that induces them. A scheme of the two interaction regions is reported in Figure 2.4.

XUV and IR beams exiting from the recombination chamber are focused by a toroidal mirror at the center of a dedicated vacuum chamber equipped with an electron ***Time of Flight (ToF) spectrometer*** (eTOF v6, Stefan Kaesdorf). The ToF measures

[1]The propagation of the the IR and XUV pulses between the two foci introduces an additional delay between the two pulses that must be measured and considered to obtain an accurate calibration of the pump-probe delay axis. The measurement of this phase delay was performed with a double RABBITT (Reconstrucion of Attosecond Beating By interference of Two-photon Transitions [27]), reader is referred to [17] for a full description of this measurement.

the kinetic energy of electrons by measuring the time an electron takes to cover a known distance. A stainless-steel needle is used to inject Argon gas in the interaction region of the ToF. XUV photons ionize the gas generating photoelectrons, which in turn interact with the IR pulse. The photoelectrons are then accelerated and collected via electron optics: they travel through the drift tube at a constant potential, where electrons with different speeds separate. Last, a micro-channel plate (MCP) amplifies the signal and produces a current that is measured. Photoelectron spectra measured at different relative delays between XUV (single pulse) and IR pulses generate a spectrogram that is called *attosecond streaking trace* [28]. From this trace, with the use of appropriate iterative reconstruction algorithms, such as the *Frequency-Resolved Optical Gating for Complete Reconstruction of Attosecond Bursts (FROG-CRAB)* [29] or the *extended Ptychographic Iterative Engine (ePIE)* [30], it is possible to retrieve the complex electric field of both pulses involved [17, 18, 19].
A silver mirror (SM1) mounted on a push-pull manipulator can be inserted into the beam path soon after the first focusing chamber to extract the converging beams and control their spatial properties. Furthermore, removing the metallic filter from the XUV arm in the recombination chamber, it is possible to exploit spatial and spectral interferometry between the IR pump and the residual IR from the XUV probe to set their temporal overlap [17].
A second toroidal mirror makes a one-to-one image of the first focus onto the solid target placed in the ***reflectometer***. This chamber consists of two main elements. The first one is a motorized sample holder, which can translate along the three directions (0.1 μm resolution) and rotate around the vertical axis (0.01° resolution). The sample support hosts an additional gold mirror, that can be moved in place of the sample to collect background and reference measurements. The reflected beam from the sample is intercepted by a second gold mirror on a roto-translator stage, that can be moved to adapt to different incidence angles with no need for major rearrangement.
The reflectometer is followed by an ***XUV spectrometer***. It is constituted by a diffraction grating to spatially disperse the incoming radiation and a micro-channel plate (MCP) followed by a phosphor screen to collect the photon signal; finally, a CCD camera takes an image of the signal on the screen. The chamber is equipped with two different gratings, one allowing detection of photons between 14 and 62 eV (spectral dispersion 18 meV/pixel) and the second in a range from 27.5 to 124 eV (spectral dispersion 11 meV/pixel).

3 | Further setup development: polarimeter for IR radiation

To further expand the possible applications of the beamline, project AuDACE [31] aims to generate, characterize ad use polarized light to study polarization-dependent electron dynamics in 2D and advanced materials. In particular, circularly-polarized light beams are used to study chiral media, like ferromagnetic materials [32] and transition metal dichalcogenides (TMDs) [33]. Several techniques can be used, among them, the so-called magnetic circular dichroism spectroscopy (MCD) and the time-resolved magneto-optical Kerr effect (TR-MOKE) spectroscopy. MCD spectroscopy measures the differential absorption of right and left circularly polarized light induced by longitudinal magnetic field [34, 35], whilst TR-MOKE spectroscopy studies laser-induced magnetization changes in materials with ferroic magnetic order by exploiting the magneto-optical Kerr effect; indeed, a magnetized material induces both a polarization change and an intensity reduction to the light reflected from it, so again it is a transient reflectivity measurement [36, 37].
For this reason, part of my thesis project has been dedicated to polarimetry -the science of measuring polarization- to obtain a reliable method to characterize the IR beam feeding the attosecond beamline.
Polarimetry is based on the use of the Stokes parameters, namely four numbers ranging from -1 to 1 that can completely describe the polarization state. For monochromatic plane waves, they can be easily obtained from the definition of the polarization ellipse [38] and can be written as

$$S = S_0 \begin{pmatrix} 1 \\ \cos(2\chi)\cos(2\psi) \\ \cos(2\chi)\sin(2\psi) \\ \sin(2\chi) \end{pmatrix} \tag{3.1}$$

where ψ is the azimuthal angle with respect to the horizontal axis of the reference system chosen, χ the ellipticity angle, describing the "width" of the ellipse, and S_0

the amplitude parameter. Generic polarization ellipse is shown in Figure 3.1, where relationships with field amplitude components E_{0x} and E_{0y} are highlighted too.

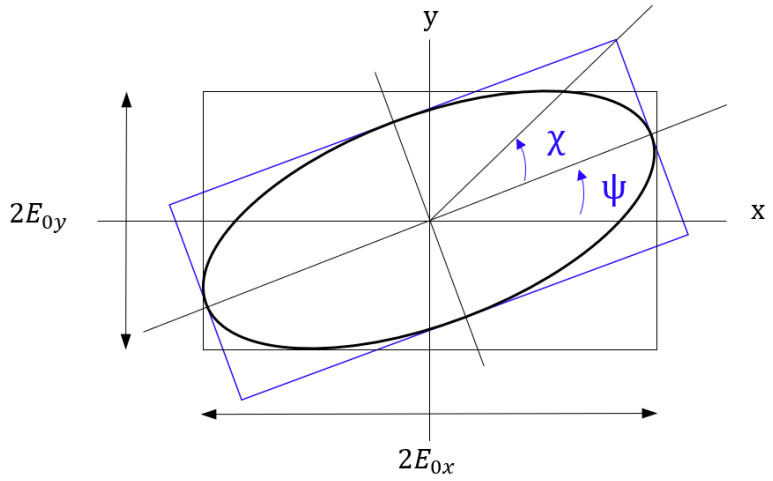

Figure 3.1: *Generic polarization ellipse.*

More generally, Stokes parameters are written as

$$S = S_0 \begin{pmatrix} 1 \\ S_1 \\ S_2 \\ S_3 \end{pmatrix} \tag{3.2}$$

where S_0 still expresses the intensity amplitude, S_1 and S_2 are related to linear polarization (given their dependence from the azimuthal angle), and S_3 describes the circular polarization component. By the definition of parameters from polarization ellipse, one can retrieve that

$$S_1^2 + S_2^2 + S_3^2 \leq 1 \tag{3.3}$$

where the left side of the expression is equal to unity only for fully-polarized light. In this work, two polarimetry methods have been compared, the so-called *classic* one and the *rotating waveplate* one. Both methods are based on the use of two optical elements, one quarter-wave plate and one polarizer, and they differ in the rotating element used for the measurement; they will be analyzed in detail below.

3.1 Methods

3.1.1 Classic

This method was the first one developed by Stokes himself, even though at that time no detector except form human eyes existed. The optical system is constituted by two optical elements, a polarizer at angle θ and a $\lambda/4$ waveplate introducing a phase delay of $\phi = \pi/2$ when inserted, while $\phi = 0$ otherwise. The scheme is reported in Figure 3.2.

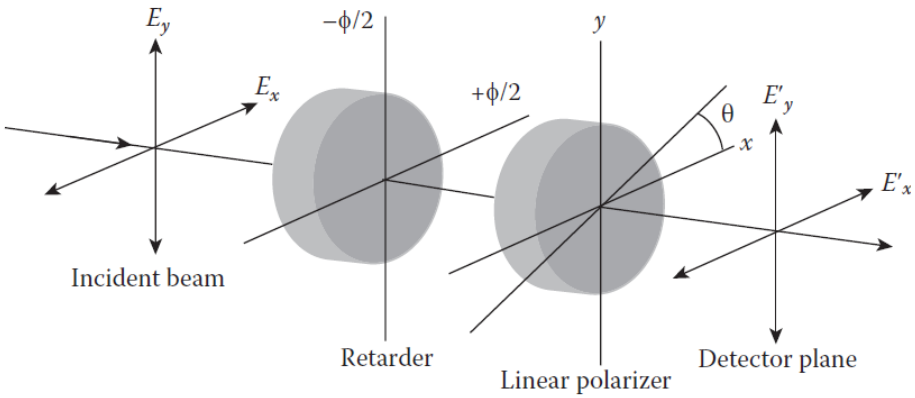

Figure 3.2: *Classical measurement scheme [38].*

The intensity measured at the detector is given by the so called *Stokes Formula*:

$$I(\theta, \phi) = \frac{1}{2} S_0 (1 + S_1 \cos(2\theta) + S_2 \cos(\phi) \sin(2\theta) + S_3 \sin(\phi) \sin(2\theta)) \tag{3.4}$$

As it can be seen from the formula, only four intensity/power measurements are strictly needed in order to retrieve all the free parameters; a possible implementation is summarized in Table 3.1.

$\boldsymbol{\theta}$	$\boldsymbol{\phi}$	$\boldsymbol{I(\theta, \phi)}$
0	0	$\frac{1}{2} S_0 (1 + S_1)$
$\frac{\pi}{2}$	0	$\frac{1}{2} S_0 (1 - S_1)$
$\frac{\pi}{4}$	0	$\frac{1}{2} S_0 (1 + S_2)$
$\frac{\pi}{4}$	$\frac{\pi}{2}$	$\frac{1}{2} S_0 (1 + S_3)$

Table 3.1: *Fundamental measurements for classical polarimetry method.*

In order to obtain a more reliable extraction of the Stokes parameters, in the present work another strategy was adopted. The polarizer performs two scans from 0 to $\pi/2$ with 1° step: in the first one, the waveplate is placed before the polarizer with the fast axis at 0°, while no waveplate is used in the second scan. Data were collected with a spectrometer, so that it was possible to characterize the polarization for each wavelength. Further details on data acquisition and analysis can be found in the next section.

3.1.2 Rotating waveplate

A more automatic method that does not require insertion and removal of any optical element is the so called rotating waveplate method. The optical elements used in this scheme are the same as the previous method, but the polarizer is fixed in the horizontal position (chosen as the 0 axis of the system) and the quarter-wave retarder rotates between 0 and π (1° step) in front of it. A schematic drawing is reported in Figure 3.3.

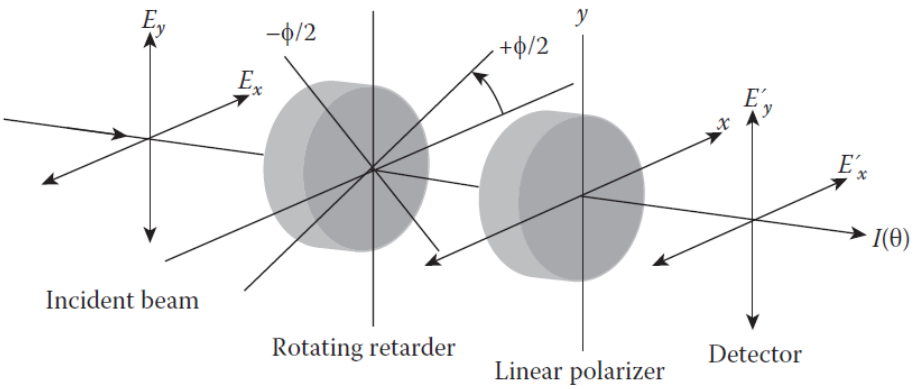

Figure 3.3: *Rotating waveplate measurement scheme [38].*

In this case, the intensity at the detector is given by:

$$I(\theta) = \frac{1}{2} S_0 (1 + S_1 \cos^2(2\theta) + S_2 \cos(2\theta)\sin(2\theta) + S_3 \sin(2\theta)) \tag{3.5}$$

where θ is the angle of the waveplate. This method is also called Fourier analysis method and, in fact, (3.5) can be rewritten as a Fourier truncated series:

$$I_n(\theta_i) = \frac{1}{2}(A - B\sin(2\theta_i) + C\cos(4\theta_i) + D\sin(4\theta_i)) \tag{3.6}$$

where θ_i is the step size (N measurements performed dividing the period π by θ_i) and

A, B, C, D are the coefficients of the series calculated as follows

$$A = \frac{2}{N}\sum_{n=1}^{N} I(n\theta_i) \tag{3.7}$$

$$B = \frac{4}{N}\sum_{n=1}^{N} I(n\theta_i)\sin(2n\theta_i) \tag{3.8}$$

$$C = \frac{4}{N}\sum_{n=1}^{N} I(n\theta_i)\cos(4n\theta_i) \tag{3.9}$$

$$D = \frac{4}{N}\sum_{n=1}^{N} I(n\theta_i)\sin(4n\theta_i) \tag{3.10}$$

From these coefficients, the Stokes parameters can be retrieved through the following equations

$$S_0 = A - C \tag{3.11}$$

$$S_1 = 2C \tag{3.12}$$

$$S_2 = 2D \tag{3.13}$$

$$S_3 = B \tag{3.14}$$

Note that in (3.6) the Stokes parameters are not normalized, so that, with respect to equation (3.5), $S_{1,2,3}$ calculated in (3.12)-(3.14) must all be divided by S_0 from (3.11).
Similarly to the previous method, also in this case a scan between 0 and π with step 1° is performed. Data acquisition and analysis are unvaried with respect to classic method and are explained in detail in next section.

3.2 Experimental measurements

3.2.1 Setup and data acquisition

The two methods explained above were applied to a number of different polarization states and positions along the laser source. The first main distinction is between polarization measurements of the IR laser pulse taken before and after the hollow core fiber used for spectral broadening and compression (see Chapter 2 for details). In the first case, measurements were taken right after the amplification stage from a mirror loss commonly used for inspection, whilst, in the second case, the beam was taken right after the fiber, before entering the chirped mirrors. Such positions

were chosen in order to avoid any other non-essential optical element that could introduce distortions. A picture of the polarimeter setup is reported in Figure 3.4. The polarimeter is made up by a Glan-Thompson calcite prism polarizer by B.Halle

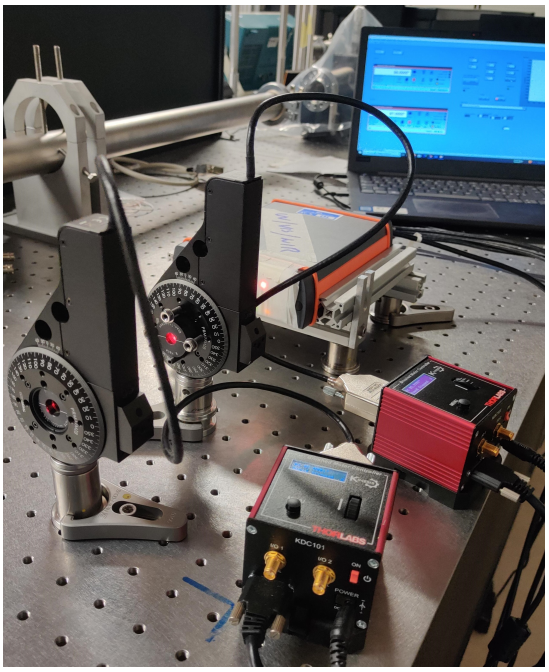

Figure 3.4: *Picture of the polarimeter setup built and used for the characterization of the IR laser beam of the beamline. The two rotor stages can be seen in line on the left side of the picture, whilst their controllers are on the right side, behind them there is the spectrometer.*

(bandwidth 350-2700 nm) and an achromatic quater-wave plate by B.Halle (quartz crystal and MgF_2, bandwidth 550-1000 nm), both mounted on motorized precision rotation stage (model PRM1/MZ8, ThorLabs) with DC Servo Motor Driver (model KDC101, ThorLabs). All the elements are controlled through a specific written LabView program, finally communicating with the spectrometer (AVANTES StarLine, AvaSpec-ULS4096CL-EVO) used for data acquisition.
This type of measurements normally require high amplitude precision as they actually measure variations of intensity. For this reason, being able to have a stable laser source is crucial. Laser fluctuations must be taken into account as a possible source of noise and their effect can be limited using sufficiently ***long integration times***.
Another crucial aspect to consider is the ***calibration*** of polarizer and waveplate, i.e. defining the common reference system, as all the parameters depend on this choice. The calibration was performed in the position chosen before the hollow-core fiber choosing as reference the beam transmitted through an horizontal fixed polarizer (Glan-Thompson calcite prism, bandwidth 350-2700 nm by B.Halle), finding out an angular offset of 4° with respect to the horizontal. Note that by specification the

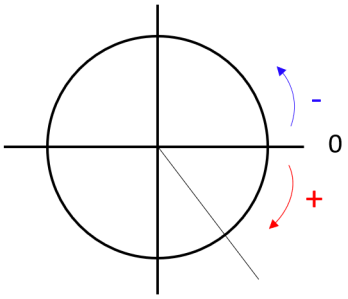

Figure 3.5: *Reference system orientation.*

polarization of the laser source should be horizontal, thus the polarizer ensures the removal of any possible residual component. The calibration of the quarter-wave plate retarder is a bit more complex. For horizontal polarization - stokes vector [1,1,0,0] - the intensity curve in (3.4) does not change for $\phi = 0$ and $\phi = \pi/2$. For this reason, the angular offset of the quarter-wave plate was chosen as the one which minimizes the difference between these two measured curves and it results as 3° with with respect to the horizontal. It is worth to highlight that these angular offsets have no physical meaning, they just depend on the positioning of the optical elements with respect to the mounting.
A final remark on the ***axes system***: the 0 axis is the horizontal one, the rotation stages are moving clockwise so this direction is the positive one. Be aware that this is actually the opposite of the commonly used convention, where counterclockwise direction is the positive direction. From now on, this system will be used as reference. A summarizing scheme is shown in Figure 3.5.

3.2.2 Data analysis

The acquired data, i.e. laser spectra for different angles of polarizer and waveplate, are then analyzed with a MATLAB code. Formulas in (3.4) and (3.5), normalized by S_0, allow to avoid normalization issues and unnecessary data manipulations. Background subtraction is done during the acquisition through LabView.
The spectral relevant region to be considered is obtained by calculating the center of mass $CM_\lambda = \dfrac{\int \lambda \, dI}{\int dI}$, and then choosing an appropriate bandwidth around it according to spectral broadening. Integrated spectra, which correspond to a good estimation of the laser power associated to a single acquisition, are obtained summing the amplitudes associated to the selected wavelengths. The experimental curves are fitted using `lsqnonlin` MATLAB fit function, which performs the minimization

of the residuals between experimental data and theoretical equations (3.4) or (3.5), according to the case. Integrated spectra are used each time to check the goodness of the fit comparing extracted curves and theoretical ones. Each polarization case has been tested with six measurements in the same conditions so that to retrieve a mean value μ and the associated standard deviation σ_{tot}, calculated as $\sigma_{tot} = \sqrt{\sigma_{\mu}^2 + \sigma_{fit}^2}$ with σ_{μ} corresponding to the sample mean standard deviation of the six measurements and σ_{fit} the standard error coming from the fitting procedure. This last term, for each wavelength, has been found to be around 5% of the mean values for parameters values around 1 and much higher (up to equal the average) for small parameters, highlighting inaccuracy in their determination. Regarding, instead, the integrated spectra, it is around the 0.1% for each parameters extracted and can be actually neglected ($\sigma_{tot} \approx \sigma_{\mu}$).

3.2.3 Narrow-band measurements

This section refers to the set of measurements taken right *before* the hollow-core fiber (see details above). The integration time is set to 100 ms, allowing a good control of beam fluctuation. A spectrum of the IR laser beam, measured with the polarimeter optical elements at 0°, can be seen in Figure 3.6. The evaluated spectral region is 40-nm wide centered around the center of mass, calculated to be at 796 nm.

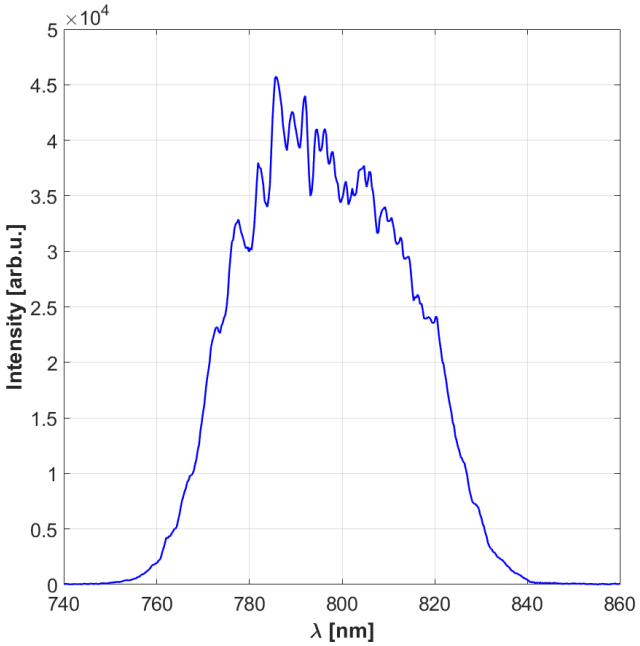

Figure 3.6: *IR intensity spectrum measured before temporal compression by hollow-core fiber. The polarimeter optical elements are at 0°.*

Horizontal polarization

In this case, no further optical element is added to the setup; the Stokes vector is expected to be [1, 1, 0, 0]. In Figure 3.7 the results obtained with the classic method; dots corresponds to the mean values of the six scans, whilst the associated error bars corresponds to the $\pm\sigma_{tot}$ interval, defined as above mentioned. It is worth mentioning that in this case the constraint in (3.3) is respected for each wavelength as well as for the integrated spectra. One can note that error bars are around 5% for S_0 and S_1, whilst considerably higher for S_2 and S_3. This can be explained in terms of fitting errors as it is more difficult to find precisely values around 0. However, results are satisfying considering that a small misalignment of the polarization direction with respect to the reference system will cause S_2 to be different from zero. The mean μ and the total standard deviation σ_{tot} of the Stokes parameters from the fit of the integrated spectra are summarized in Table 3.2. S_0 will not be discussed anymore as it gives no significant information on polarization state, being just an indication of the intensity.

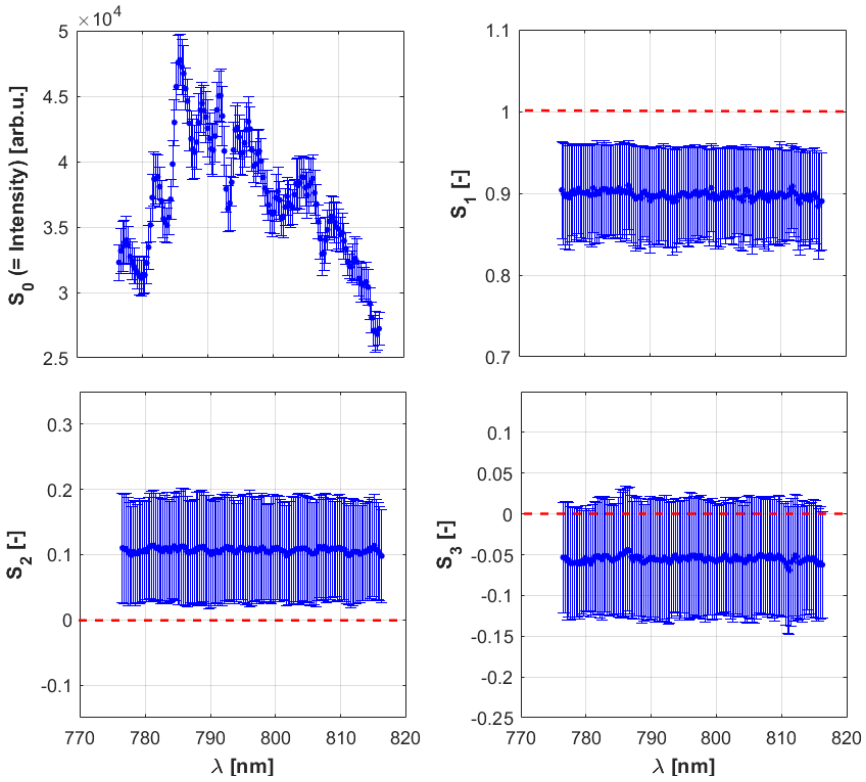

Figure 3.7: *Stokes parameters retrieved with the classic method at each wavelength for the case of linear horizontal polarization. Dots • correspond to mean values and error bars are associated to $\pm\sigma_{tot}$ intervals. Red dashed lines correspond to the expected theoretical values.*

Figure 3.8, instead, presents the results obtained with the rotating waveplate method.

	μ	σ_{tot}	expected
$\boldsymbol{S_1}$	0.898	0.029	1
$\boldsymbol{S_2}$	0.107	0.062	0
$\boldsymbol{S_3}$	-0.055	0.051	0

Table 3.2: *Stokes parameters of the integrated spectra retrieved with the classic method for the case of linearly horizontally polarized light.*

In this case, results are less satisfying: the constraint (3.3) is not respected -note S_1 values really close to or higher than 1 for most wavelengths- and expected values are less stable at different wavelength, highlighting some fit unreliability. Even though this method is largely and successfully used for its practicality (no need of manually changing the optical elements), in these tests it did not provide the expected results. The reason behind this issue must be further investigated, however some critical point to be check could be the calibration (much difficult for the waveplate, that here is the key element) and the fit reliability, in this case, in fact, it is required the fitting of a rapidly oscillating curve. For this reason, all the other tests were performed only with the classic method.

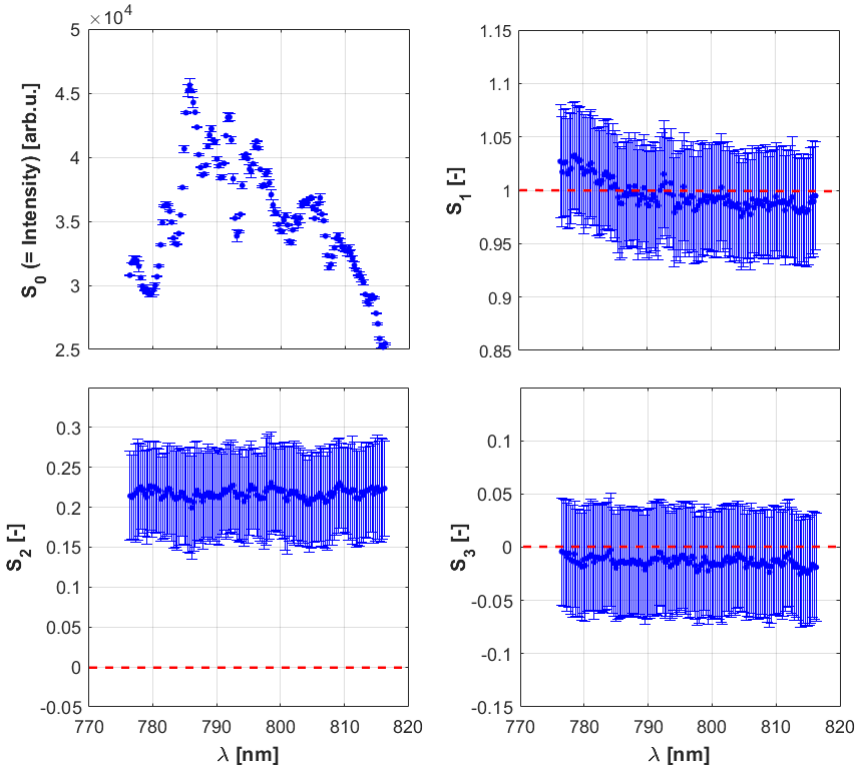

Figure 3.8: *Stokes parameters retrieved with the rotating waveplate method at each wavelength for the case of linear horizontal polarization. Dots • correspond to mean values and error bars are associated to $\pm\sigma_{tot}$ intervals. Red dashed lines correspond to the expected theoretical values.*

To conclude this section, it can be argued that the polarization state is reasonably horizontal, with S_1 really close to 1 and the other two parameters sufficiently close to 0. S_2 seems the one most sensible to misalignment and calibration error and in fact it differs from 0 in case of linear polarization at angles greater that 0, being consistent with S_1 smaller than 1.

Circular polarization

In this case, circular polarization was obtained using an achromatic quarter-wave plate of bandwidth 500-900 nm (B.Halle) at -45° with respect to the reference system in Figure 3.5, generating left circular polarization corresponding to a stokes vector [1, 0, 0, -1]. Also in this case, the constraint (3.3) is respected at each wavelength and error bars are similar to the previous case. Stokes mean values μ and standard deviations σ for the integrated spectra are reported in 3.3.

	$\boldsymbol{\mu}$	$\boldsymbol{\sigma_{tot}}$	**expected**
$\boldsymbol{S_1}$	0.029	0.024	0
$\boldsymbol{S_2}$	0.067	0.043	0
$\boldsymbol{S_3}$	-0.908	0.018	-1

Table 3.3: *Stokes parameters of the integrated spectra for the case of left circular polarization.*

Arbitrary linear polarization

In this case, linear polarization at -30° with respect to the reference system in fig.3.5 was obtained using an achromatic half-wave plate of bandwidth 500-900 nm (B.Halle) at -15°. Stokes vector corresponding to this polarization is $[1, 0.5, -\sqrt{3}/2, 0]$. Results and fit performance are consistent with what found before; the retrieved parameters for integrated spectra are reported in Table 3.4 . One can notice that S_1 is quite smaller than expected but anyway this is in accordance with possible errors in the angular positions of the half-wave plate; in this case a correction of around -5° of ψ, having so polarized light at -35°, is consistent with fitted values.

	$\boldsymbol{\mu}$	$\boldsymbol{\sigma_{tot}}$	**expected**
$\boldsymbol{S_1}$	0.290	0.037	0.5
$\boldsymbol{S_2}$	-0.870	0.017	$-\sqrt{3}/2$
$\boldsymbol{S_3}$	0.010	0.043	0

Table 3.4: *Stokes parameters from fit of the integrated spectra in case of linearly polarized light at -30°.*

Figure 3.9 well summarizes all the three cases. It reports experimental data for integrated spectra as mean values (dots) and corresponding total standard deviation (shaded region). Dashed lines correspond to theoretical curves of the three cases above, i.e. (3.4) calculated with theoretical parameters, whilst continuous lines are obtained from (3.4) using the Stokes values retrieved by the fit. darker curves tonalities refer to $\phi = 0$ and brighter ones to $\phi = \pi/2$. For horizontal polarization (blue and light blue), one can appreciate that the theoretical curves are perfectly superimposed, whilst the experimental ones are not (even though they are close): this is due to the linear components being not exactly horizontal. Green curves are related to -30° linear polarization: the variance from theoretical ones results from an actual slightly different angular position, as explained before. To conclude, the red curves of circular polarization are very close to the theoretical expectations, even though the darkest curve is not properly horizontal, needless to say, also in this case, errors are due to small angle misalignment difficult to avoid.

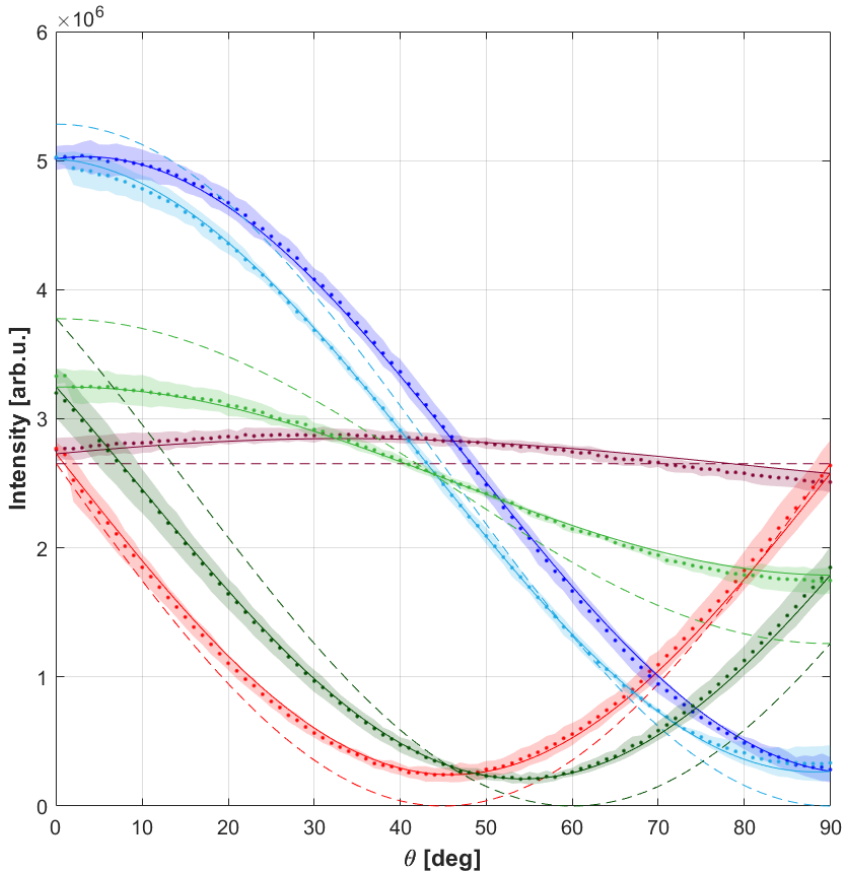

Figure 3.9: *Theoretical, experimental and fitted curves comparison for the three polarization cases considered in narrow-band pre-fiber measurements. —— fitted, - - - theoretical, • experimental data. Blue horizontal, red circular and green 30° linear polarization. Darker color shade for $\phi = 0$, lighter for $\phi = \pi/2$.*

3.2.4 Broad-band measurements

This section refers to the set of measurements taken right *after* the hollow-core fiber (see details above). Two different situations were compared. First one with fiber in vacuum and latter one with fiber filled with 0.5 bar of Ne gas (total pressure inside 1.5 bar), in order to ensure a broader spectrum that can be observed in Figure 3.10. Even in these two measurements the same fixed polarizer used for narrow-band measurements was set in front of the system to allow proper calibration; the zero axis is remained unvaried as well as the zero angle of the waveplate. Integration time is set to 100 ms, the analyzed spectral bandwidth is 100-nm wide around the center of mass, found to be at 797 nm.

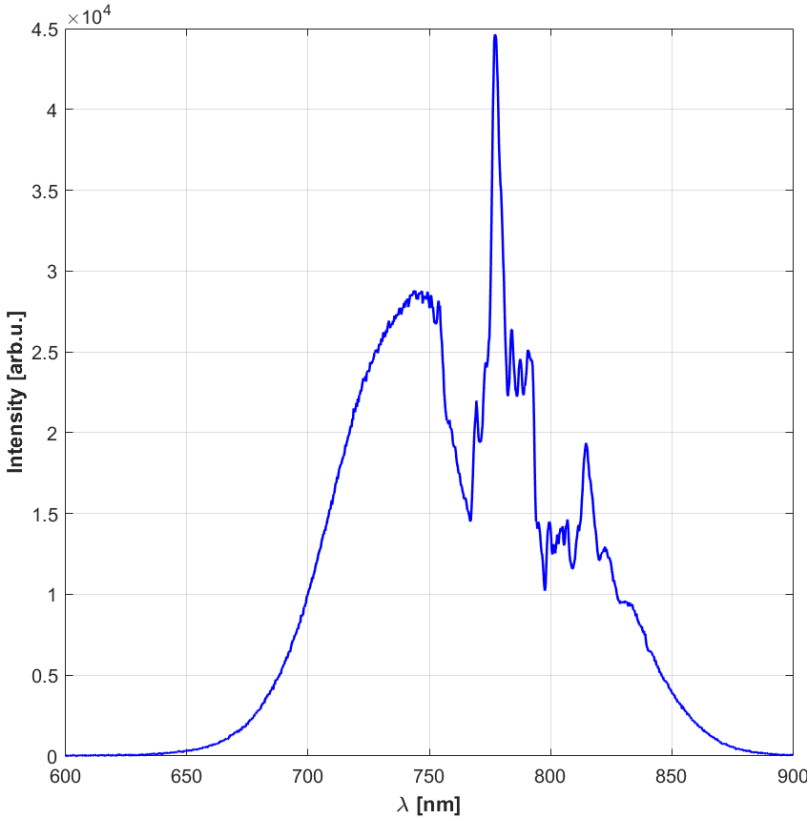

Figure 3.10: *Broad spectrum exiting from the hollow core fiber filled with 0.5 bar of Ne. Polarimeter optical elements set at 0°.*

Results of the integrated spectra for the two cases are summarized in Tables 3.5 and 3.6. One can notice that S_3 in sensibly higher than in the narrow-band case, with almost no difference in empty/full fiber conditions, suggesting the presence of a residual elliptical component.

	μ	σ_{tot}	expected
S_1	0.967	0.019	1
S_2	-0.006	0.050	0
S_3	-0.220	0.031	0

Table 3.5: *Fiber in vacuum. Results for integrated spectra.*

	μ	σ_{tot}	expected
S_1	0.974	0.030	1
S_2	0.007	0.055	0
S_3	-0.198	0.033	0

Table 3.6: *Fiber filled with Ne gas. Results for integrated spectra.*

4 | Pulse interaction at an interface: static reflectivity

A deep knowledge of the static reflectivity of a sample is a fundamental requirement to properly interpret a transient reflectivity experiment. This chapter is devoted to the description of the interaction between a laser pulse and a plane solid interface. After a brief introduction about the Fresnel coefficients for plane waves, the discussion proceeds presenting the adaptation of the model to the case of a pulse with Gaussian temporal and spatial profiles. The model is then applied to the IR and XUV pulses generated by the beamline illustrated in Chapter 2 and interacting with a diamond sample, whose ultrafast dynamics have been investigated with transient reflectance measurements shown in the final chapter of this thesis. Finally, possible improvements to the model are briefly discussed in the last section of this chapter.

4.1 The Fresnel coefficients

Fresnel equations and coefficients describe the fraction of reflected r and transmitted t amplitude of an electromagnetic field of a plane wave at the interface of two materials with polarization-dependent formulas. Thus, the reflected field will be $E_r = rE_{in}$ and the transmitted $E_t = tE_{in}$. Considering instead the field intensities, one can define the reflectance $R = |r|^2$ and transmittance $T = |t|^2$, so that the reflected intensity is $I_r = RI_{in}$ and the transmitted $I_t = TI_{in}$.[1]

In the experimental measurements of this work, the laser beams present s-polarization, i.e. the electric field is perpendicular to the plane of incidence. For this reason, the following discussion will focus only on this case, omitting the p-polarization one, i.e.

[1]Note that considering the field *power*, the transmittance becomes $T = n\left(\frac{\cos\theta_2}{\cos\theta_1}\right)t^2$, with an additional factor to include the cross-sectional areas of the incident and transmitted beams; n is the relative refractive index of the interface, θ_1 and θ_2 are respectively the angle of incidence and the transmission angle.

the electric field parallel to the plane of incidence. A comprehensive discussion about the definition of the Fresnel coefficients can be found in [39].
In the most general case, the reflectivity coefficient can be expressed as

$$r_s = \frac{\mu_2 n_1 \sqrt{1 - \sin^2(\theta_1)} - \mu_1 n_2 \sqrt{1 - n^2 \sin^2(\theta_1)}}{\mu_2 n_1 \sqrt{1 - \sin^2(\theta_1)} + \mu_1 n_2 \sqrt{1 - n^2 \sin^2(\theta_1)}} \,, \tag{4.1}$$

whilst the transmittivity coefficient as

$$t_s = \frac{2\mu_2 n_1 \sqrt{1 - \sin^2(\theta_1)}}{\mu_2 n_1 \sqrt{1 - \sin^2(\theta_1)} + \mu_1 n_2 \sqrt{1 - n^2 \sin^2(\theta_1)}} \,, \tag{4.2}$$

where $\mu_{1,2}$ and $n_{1,2}$ are respectively the magnetic permeability and the refractive indices of the two materials constituting the interface, θ_1 is the angle of incidence with respect to the normal to the interface, and $n = \frac{n_1}{n_2}$ is the relative refractive index of the interface. Note that these formulas apply also to the case of complex refractive indices.
These coefficients can be further simplified in case of pure dielectric materials, which present $\mu_2 = \mu_1 = 1$. One can also note that, according to the Snell's law $n_1 \sin(\theta_1) = n_2 \sin(\theta_2)$, the square-root term involving n is actually $\cos(\theta_2)$, the cosine of the transmission angle.
These coefficients can also be extended to multilayered structures considering the wave propagation inside the layer and multiple reflections and transmissions at each interface. Several methods based on transfer matrices are used in order to find the Fresnel coefficients of the structure, please refer to [39] and [40] for further details.

4.2 Pulse propagation and reflection at a plane interface

The aim of this section is to fully describe the interaction of a laser pulse with a plane interface. A pulse can be defined as

$$P(x', y', t) = A(x', y')B(t)e^{i(\vec{k_0} \cdot \vec{r} - \omega_0 t)} \,, \tag{4.3}$$

where ω_0 is the carrier angular frequency and $\vec{k_0} = k_0 \hat{u}_0 = n_1(\omega_0)\frac{\omega_0}{c}\hat{u}_0$ the wave vector (n_1 is the refractive index of the material in which the pulse propagates). The most common and simple case of laser pulse is the TEM_{00}, which presents both a

spatial and a temporal Gaussian profile, so that

$$A(x', y') = e^{-\frac{x'^2+y'^2}{w_0^2}} \tag{4.4}$$

and

$$B(t) = e^{-\frac{t^2}{\tau^2}} \tag{4.5}$$

with w_0 being the beam waist and $\tau = 2\sqrt{\log(2)}\ \Delta t_{FWHM}$, where Δt_{FWHM} is the pulse duration corresponding to the full width at half maximum.
To correctly retrieve the reflected and transmitted pulses, the incoming pulse must be Fourier-transformed. In fact, r and t are functions of the refractive indices, which then depend on ω, and on the angle of incidence, thus on the wave vectors k in space. The transformed pulse is

$$\tilde{P}(k'_x, k'_y, \omega) = \iiint dx'\ dy'\ dt\ A(x', y')B(t)e^{i\left(\vec{k_0}\ \cdot\ \vec{r}\ -\ \omega_0 t\right)}e^{-i\left(\vec{k}'\ \cdot\ \vec{r}\ -\ \omega t\right)}\ , \tag{4.6}$$

which can be rewritten, separating variables, as

$$\begin{aligned}\tilde{P}(k'_x, k'_y, \omega) &= \iint dx'\ dy'\ A(x', y')e^{-i\left[(\vec{k}'-\vec{k_0})\ \cdot\ \vec{r}\ \right]} \int dt\ B(t)e^{-i(\omega\ -\ \omega_0)t} \\ &= \tilde{A}(k'_x - k_{0x}, k'_y - k_{0y})\tilde{B}(\omega - \omega_0)\ ,\end{aligned} \tag{4.7}$$

The reference system $\{x',\ y',\ z'\}$ has been chosen so that $\overrightarrow{k_0}$ lies on the z'-axis and it is shown in Figure 4.1. Now, remembering that in the Fresnel equations the angles are defined with respect to the normal axis of the interface, we should calculate the correct incident angle for each space-transformed component. The reference system must be changed accordingly, so that the z-axis corresponds to the normal to the interface. Figure 4.1 will help in doing this procedure. In fact, the transformation from system $\{x',\ y',\ z'\}$ to $\{x,\ y,\ z\}$ is a rotation of angle θ_1, which is the angle of incidence of the carrier component $\overrightarrow{k_0}$ propagating along z'. The new k-space vector components are:

$$\begin{pmatrix} k_x \\ k_y \\ k_z \end{pmatrix} = \begin{pmatrix} k'_x \\ k'_z \sin(\theta_1) + k'_y \cos(\theta_1) \\ k'_z \cos(\theta_1) - k'_y \sin(\theta_1) \end{pmatrix}\ . \tag{4.8}$$

Note that by definition $k'_z = \sqrt{k^2 - k'^2_x - k'^2_y}$, where $k = n_1(\omega_i)\dfrac{\omega_i}{c}$ is the wave vector for each i-th component. The *i-th* spatially-dispersed pulse component reaches the

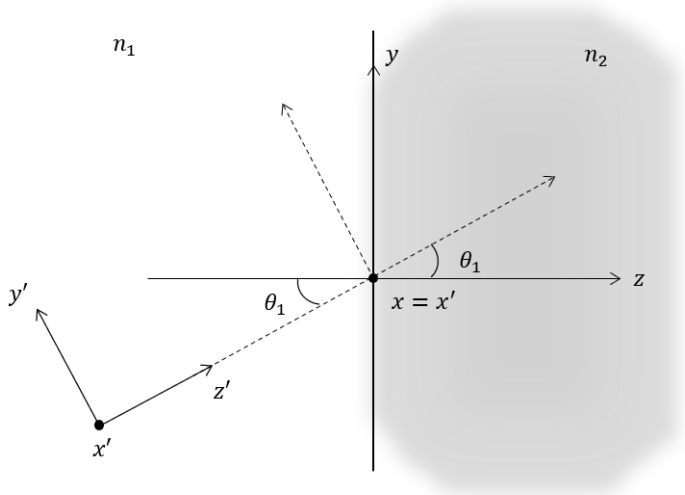

Figure 4.1: *Rotation of the reference system, from {x′, y′, z′} to {x, y, z}, where z-axis is normal to the interface between medium 1 and medium 2.*

interface with an angle

$$\theta_i = \arctan \frac{\sqrt{k_x^2 + k_y^2}}{k_z^2} \ , \tag{4.9}$$

obtained by geometrical consideration using Figure 4.2, a 3D representation of the same reference system as Figure 4.1. At this point, the r and t Fresnel coefficients in

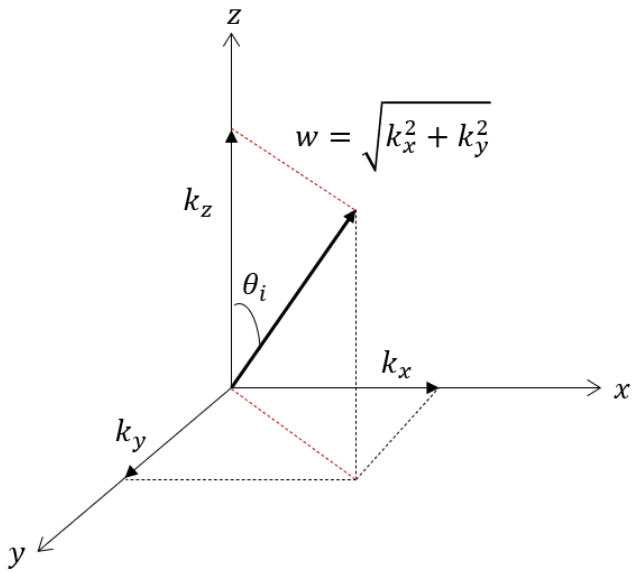

Figure 4.2: *Generic wave component reaching the interface with an angle θ_i.*

(4.1) and (4.2), can be calculated for each *i-th* component at its own angle θ_i. The

reflected and transmitted pulses can be then calculated by anti-transforming

$$P_r(x,y,t) = \mathscr{F}^{-1}\left\{\tilde{P}(k_x,k_y,\omega)\cdot r_s(\theta_i,\omega)\right\} \tag{4.10}$$

$$P_t(x,y,t) = \mathscr{F}^{-1}\left\{\tilde{P}(k_x,k_y,\omega)\cdot t_s(\theta_i,\omega)\right\} \tag{4.11}$$

Finally, having θ_i for each component, it is also possible to calculate the transmission angle by Snell's law: $\theta_{t,i} = \arcsin\dfrac{n_1}{n_2(\omega_i)} sin\theta_i$, useful to define the penetration depth in medium 2. In fact, the transmitted pulse propagates in the second medium as

$$\begin{aligned} P_t(x,y,z,t) &= P_t(x,y,t)\exp\left(i\ \overrightarrow{k_t}\cdot z\hat{u}_z\right) \\ &= P_t(x,y,t)\exp\left(i\frac{\omega}{c}n_2\cos(\theta_{t,i})z\right) \end{aligned} \tag{4.12}$$

In the next section, I will present some significant cases, related to the experimental measurements illustrated in Chapter 6, where the sample is diamond.

4.3 IR pulse at vacuum-diamond interface

In this first example, we will consider the IR pulse in vacuum ($n_1 = 1$) interacting with the diamond sample. As explained briefly in the introductory chapter, the few-cycle IR pulse excites the sample, whose reflectance, then, is studied as a function of the XUV pulse energy and the reciprocal pump-probe delay.

As a first approximation, the pulse has both temporal and spatial Gaussian profile; its beam waist is set at 100 μm, it is centered at 800 nm and has a FWHM duration of around 8 fs. These values are consistent with the pump pulse parameters currently used in the attosecond beamline (for more details, please refer to Chapter 2). In order to actually perform the calculations shown in the previous section, the complex refractive index of diamond is needed; data are taken from [41] and they are published in the `refractiveindex.info` database [42].

Diamond is transparent to IR radiation ($\Re e\{n\}$ almost constant and no absorption, $\Im m\{n\} = 0$). In Figure 4.3, the field spectrum of the IR pulse and the real (black) and complex (red) parts of the diamond refractive index are reported.

The angle of incidence of the carrier frequency is set to $\theta_0 = 44.6°$. This angle is the one used for the measurements presented in Chapter 6 and its choice will be discussed exhaustively in section 5.1. The temporal profiles of the reflected and transmitted pulses at the interface are shown in Figure 4.4, compared to the incident one in light blue. The black curve refers to the correction adopted for the incident angle of

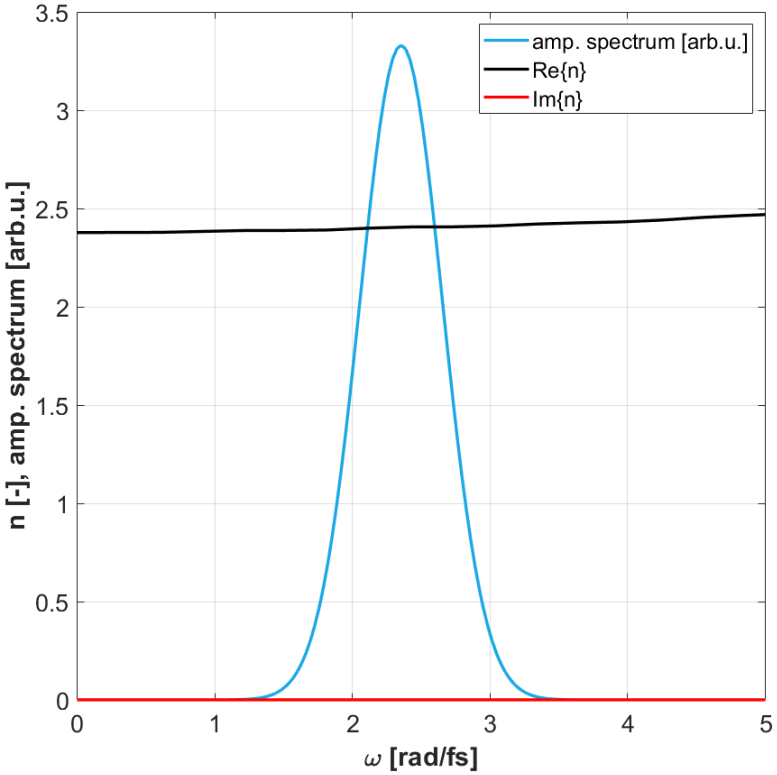

Figure 4.3: *Real and imaginary part of the complex refractive index of diamond in the IR spectral range considered.*

each component, explained above, whilst the dashed line in red is obtained without correction: all the components have an angle of incidence equal to θ_0.

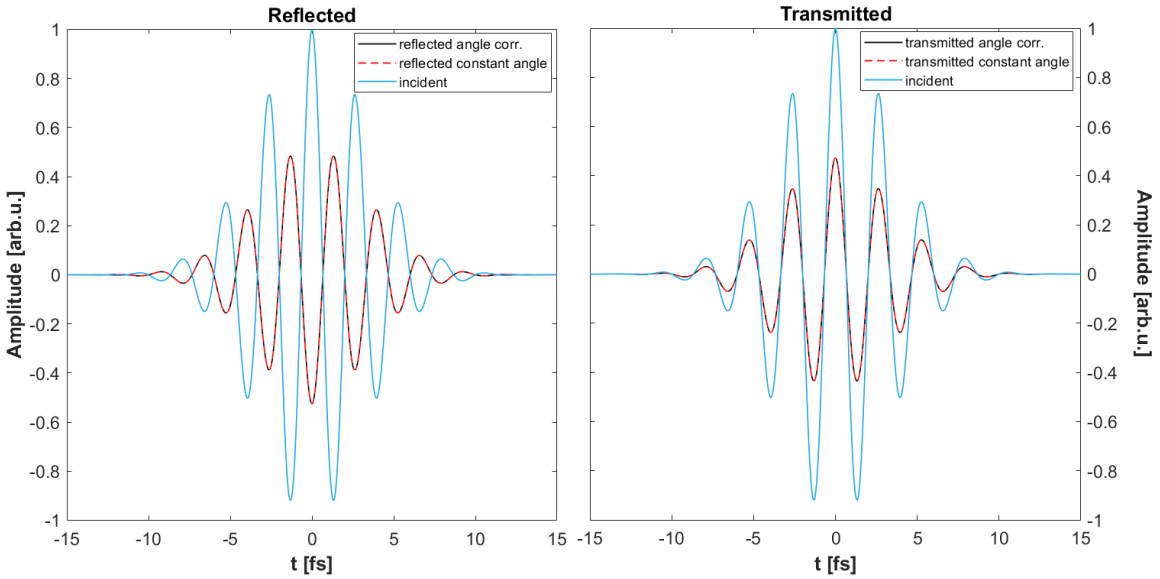

Figure 4.4: *Temporal profiles of the IR reflected and transmitted pulses at the vacuum-diamond interface.*

From this figure, one can notice that there is no difference with and without angle correction, i.e. by neglecting the spatial dispersion the results are still accurate, the difference between the peak of the temporal profile is in the order of 10^{-8}. Giving that $n_2 > n_1$, this is a case of external reflection and, as expected, the reflected pulse experiences a phase shift of π. The pulse temporal extension does not change due to the absence of dispersion. The spatial profile does not present any significant variation from the one obtained with the angular approximation and its shape is unvaried.

To conclude this section, Figure 4.5 shows the spatial profile of the Gaussian IR field at the vacuum-diamond interface, corresponding to x=0 in space. The interference pattern between incident and reflected field is clearly visible and continuity at the interface is respected, with the transmittance showing lower amplitude as expected.

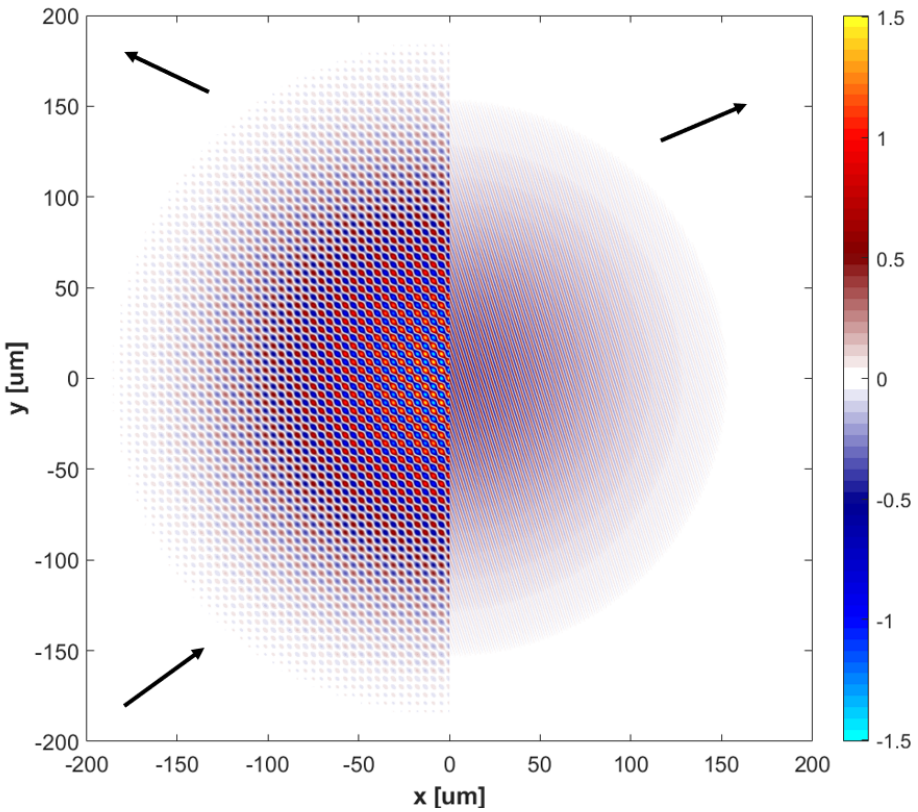

Figure 4.5: *Spatial profile of the Gaussian IR pulse interacting with the vacuum-diamond interface (located at x=0) given by the superposition of incident, reflected and transmitted pulses. Arrows point the direction of incidence, reflection and transmission.*

4.4 XUV pulse at vacuum-diamond interface

This section is devoted to the description of the XUV probe pulse in vacuum interacting with the diamond sample. Also in this case, as a first approximation, the pulse has both temporal and spatial Gaussian profile; the FWHM duration is set to 250 as, it is centered at 35 eV and the beam waist is 10 μm. As for the IR pulse, the angle of incidence of the central component is 44.6°. The complex refractive index used for this simulation was calculated by S. Sato and coworkers in [11] using the independent particle approximation, i.e. null electron-electron interaction. The calculated

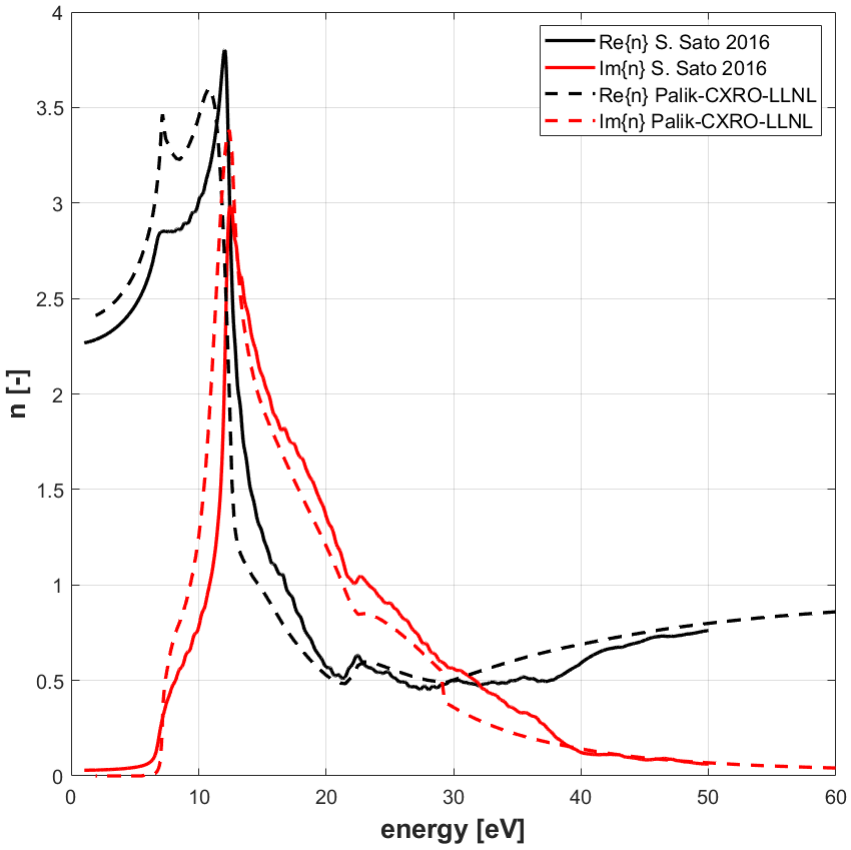

Figure 4.6: *Real and imaginary parts of the diamond refractive index calculated by S. Sato (2016) and from public databases.*

real and imaginary parts are compared with data from literature, extracted from [43] (low energies) and two other public databases, CXRO [44] and LLNL [45] for high energies[2]; Figure 4.6 reports the result of this comparison. As one can notice, there is a good agreement for both curves.
In Figure 4.7, instead, there is the XUV pulse spectrum and the corresponding values of the real and imaginary parts of the diamond refractive index.

[2]here, optical constants are calculated starting from the atomic scattering factors.

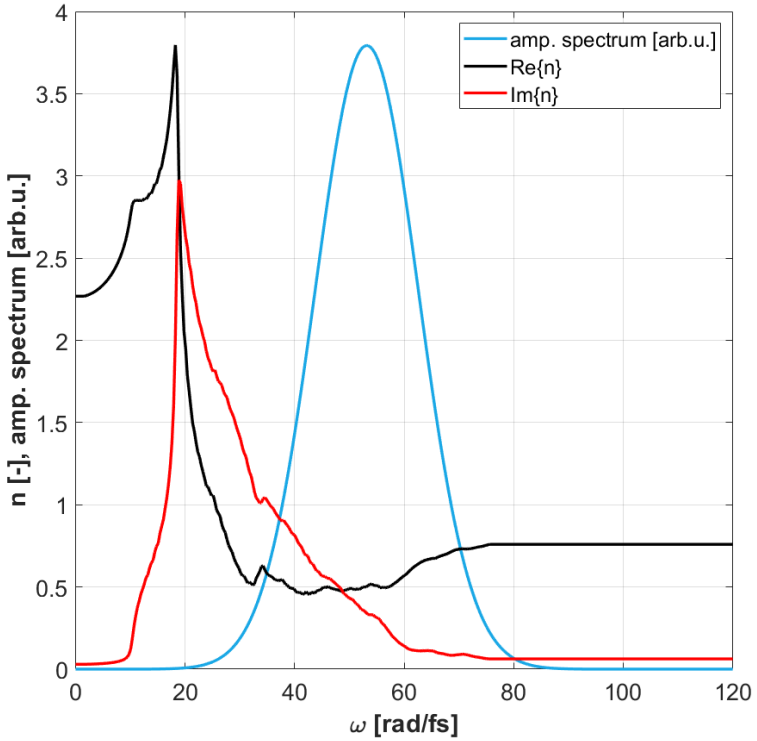

Figure 4.7: *Real and imaginary parts of the diamond refractive index in the XUV spectral range considered.*

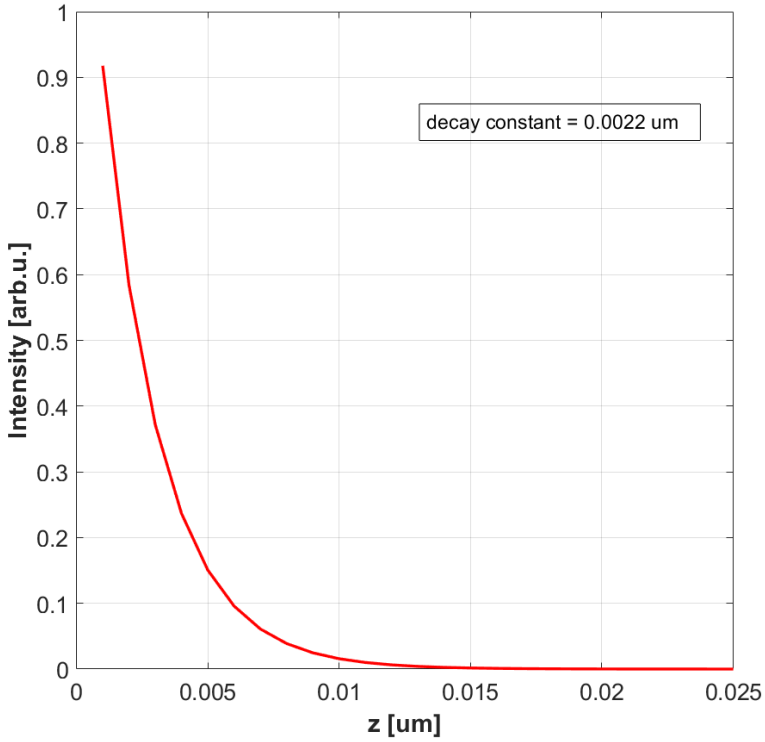

Figure 4.8: *Peak intensity exponential decay of the XUV pulse in diamond.*

For this spectral region, the imaginary part is different from zero (values ranges from 0.5 to 1). As a consequence, absorption does not allow the pulse to propagate for more than few nanometers in the sample. The propagation of the pulse is calculated with equation (4.12); taking, then, the peak intensity as a function of the material thickness (z direction), the expected exponential decay (Lambert Beer's law) can be observed in Figure 4.8. The decay constant is found to be 0.0022 μm, so, after five times the decay constant, which means at 11 nm, the pulse can be considered completely absorbed. Note that the incident angle chosen for the central component is close to the critical angle corresponding to 43.7 eV, so that total external reflection can be achieved; for a more complete discussion on this point see Section 5.1.
As a last result, in Figure 4.9 the temporal profiles of the XUV reflected and transmitted pulses are reported. Also in this case, the spatial properties of the pulse and so the consequent correction on the angle of incidence do not have a significant impact neither on the spatial nor on the temporal profile (maximum difference in the order of 10^{-8}) . The transmitted pulse experiences a field enhancement of approximately 1.3 times, consistent with total external reflection.

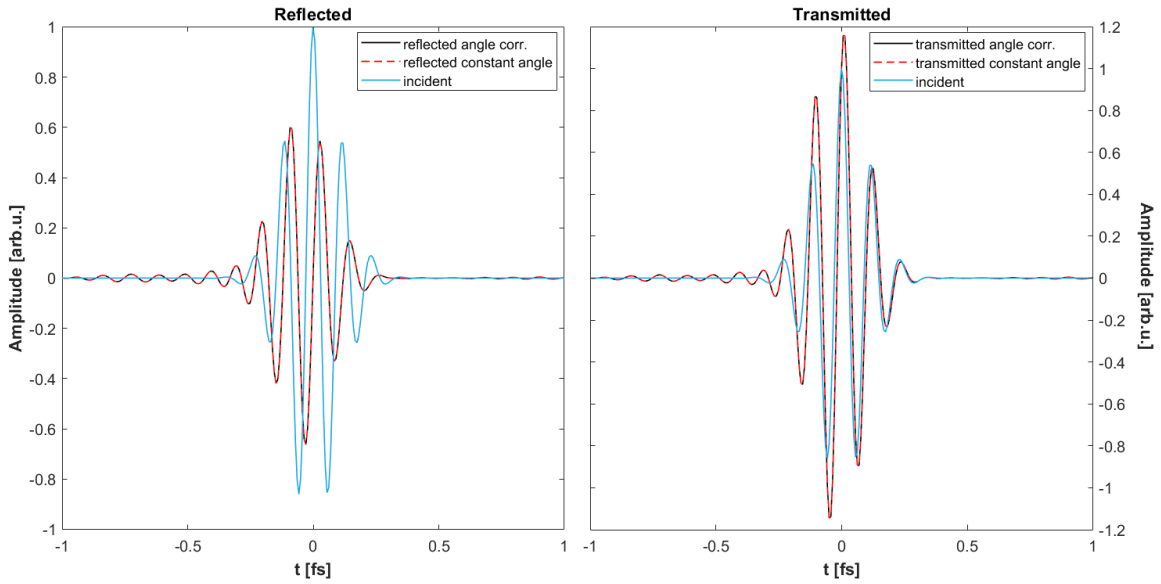

Figure 4.9: *Temporal profiles of the XUV reflected and transmitted pulses at the vacuum-diamond interface.*

4.5 Surface roughness

The surface quality can play an important role when working in total reflection regime - remember that the XUV pulse propagates just for few nanometers in the material. For this reason, a complete model should consider the surface roughness and its contribution to scattering. As a first step, it is possible to model the scattering from the surface thanks to the *Debye-Waller factor*. This factor represents the attenuation in intensity of the reflected pulse due to scattering at an interface of roughness σ for incident light with scattering vector $q = 4\pi \sin(\theta_i)/\lambda$ and it is given by

$$exp\left(-\sigma^2 q^2\right) , \tag{4.13}$$

thus the reflectance become

$$R = |r|^2 e^{\left(-\sigma^2 q^2\right)} . \tag{4.14}$$

This correction has been successfully applied in [46] to study Germanium.
More complex models used to describe the scattering from a surface are discussed in [47], as for example the so called *Beckmann-Spizzichino* model [48], which is briefly described in Appendix A.
Up to now, for the experiments and studies here developed the surface roughness has not been considered, given that most of the time the samples are prepared to be clean and smooth. However, we are planning to consider the effect of the scattering from a rough surface to provide a more accurate model of the situation under investigation.

5 | Key parameters for transient reflectivity measurements

The static reflectivity properties of a material strongly depend on the light angle of incidence. The same is true for the dynamical signals reported in Chapter 6. Here I will show which is the procedure to follow in order to optimise the signal in a transient reflectivity measurement, i.e. the appropriate choice of the angle of incidence. Moreover, this procedure is strongly dependent on the complex refractive index of the material under investigation in the XUV spectral region. As a consequence, an accurate determination of it must be done. Especially for highly innovative advanced materials, this is not straightforward, most of the time there are not calculated values nor experimental ones. The solution is provided by static reflectivity measurements at synchrotron facilities. An example of them will be discussed in the last section of this chapter.

5.1 Determination of the angle of incidence

The angle of incidence is a crucial parameter in a transient reflectivity experiment. Given that most of the materials in the XUV spectral range have an index of refraction lower than one, finding the critical angle, it is possible to work at total external reflection. The advantage of this choice lies in the exploitation of the field enhancement of the XUV probe pulse at the interface and penetration depth of the probe of few nanometers, as shown in Figure 4.9 and 4.8, and in a higher transient reflectivity signal, as it will be shown below with a small calculation. To reach this condition, there are two possible procedures to follow, that, in a first approximation, are equivalent: the first one consists in the direct calculation of the critical angle for each XUV photon energy, whilst the second proceeds defining the *sensitivity functions*, which describe the sensitivity of the reflectivity to the real and imaginary part of the refractive index. This approach has been fully described in [12], [16], and [46].
As shown in the previous chapter, thanks to the Fresnel coefficients, the reflectance

$R_s = |r_s|^2$ can be expressed as function of the complex refractive index of the material (see equation (4.1)). Remembering that the refractive index is the square root of the dielectric function $\varepsilon = \varepsilon' + i\varepsilon''$, one can calculate the derivative of the reflectivity with respect to the real and imaginary parts of ε obtaining[1]

$$\frac{\partial R_s}{\partial \varepsilon'} = 2\Re e \left\{ r_s^* \cdot \frac{\partial r_s}{\partial \varepsilon'} \right\} \tag{5.1}$$

and

$$\frac{\partial R_s}{\partial \varepsilon''} = 2\Re e \left\{ r_s^* \cdot \frac{\partial r_s}{\partial \varepsilon''} \right\} = -2\Im m \left\{ r_s^* \cdot \frac{\partial r_s}{\partial \varepsilon'} \right\} \ , \tag{5.2}$$

with

$$\frac{\partial r_s}{\partial \varepsilon'} = -\frac{cos(\theta_1)}{\sqrt{n_2^2 - \sin^2(\theta_1)} \cdot \left[cos(\theta_1) \sqrt{n_2^2 - \sin^2(\theta_1)} \right]^2} = -i \frac{\partial r_s}{\partial \varepsilon''} \tag{5.3}$$

The derivatives in (5.1) and (5.2) are the so-called *absolute* sensitivity functions. Especially when real and imaginary parts of the dielectric function are very different in magnitude, it can be useful to define the *relative* sensitivity functions [46] as

$$S_{\varepsilon'} = \frac{\varepsilon'}{R_s} \cdot \frac{\partial R_s}{\partial \varepsilon'} \tag{5.4}$$

$$S_{\varepsilon''} = \frac{\varepsilon''}{R_s} \cdot \frac{\partial R_s}{\partial \varepsilon''} \tag{5.5}$$

In [16] it has been shown that the critical angle tracks those points in which $\frac{\partial R_s}{\partial \varepsilon''} = 0$, so, in a first approximation, the two approaches can be considered equivalent. However, the approach has not yet been tested for a variety of different material and must be evaluated case by case.

As stated at the beginning of this section, choosing the critical angle as the angle of incidence for the experiment has the expected advantage of maximizing the transient signal. The transient reflectivity can be defined as the normalized difference between the intensity XUV spectrum reflected from the sample in presence and in absence of the IR pulse excitation; it can be expressed as

$$\frac{\Delta R}{R}(\mathcal{E}, \Delta t) = \frac{R_{IR}(\mathcal{E}, \Delta t) - R_0(\mathcal{E})}{R_0(\mathcal{E})} \ , \tag{5.6}$$

[1] the notation is the same used in Chapter 4: subscript 1 is used for the incidence angle in medium 1, that is vacuum, and subscript 2 for physical quantities referred to medium 2 (the sample), whilst n is the relative refractive index.

where $\mathcal{E}$ is the XUV photon energy, Δt is the reciprocal delay between IR and XUV pulses and subscripts IR/0 refer to the presence/absence of the IR pump; in absence of it, R_0 is the static unperturbed reflectance discussed in Chapter 4. The presence of the IR pulse induces a variation on the dielectric function that can be tracked through the variations in the reflectance. Approximating R_{IR} with the first two terms of its Taylor series with respect to ε it becomes

$$\frac{\Delta R}{R} \approx \frac{R_0 + \left.\frac{\partial R_{IR}}{\partial \varepsilon}\right|_{\varepsilon_0} d\varepsilon - R_0}{R_0} = \frac{1}{R_0} \left.\frac{\partial R_{IR}}{\partial \varepsilon}\right|_{\varepsilon_0} d\varepsilon \ . \tag{5.7}$$

Considering a purely real dielectric function, i.e. no absorption, the transient reflectivity, regardless of the value of dε that can be treated as a coefficient, diverges as approaching the critical angle, in fact, looking at equations (4.1), (5.1), and(5.3) one can notice that the denominator goes to zero when $\sin(\theta) = n_2$, that is the definition of the critical angle. This is not completely true in case of complex dielectric function, but still the critical angle remains a good indicator in order to maximize the signal. In the next section, I will apply this considerations to the case of diamond, which is anything but standard with respect to what discussed above.

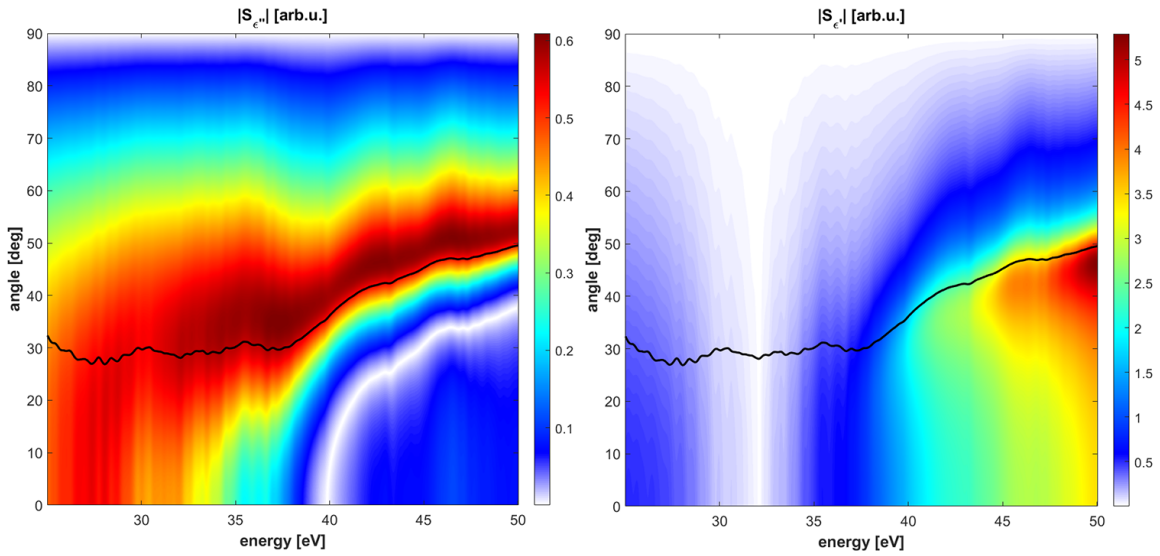

Figure 5.1: *On the left, $|S_{\varepsilon''}|$ as function of the XUV energy and the incident angle and on the right $|S_{\varepsilon'}|$. The black line represents the critical angle at each energy.*

5.1.1 Diamond critical angle

In the left side of Figure 5.1, the modulus of the relative sensitivity to the imaginary part of the dielectric function $S_{\varepsilon''}$, calculated with (5.5) by using the diamond refractive index values from [11], is reported. The picture shows in black also the critical angle calculated as $\theta_c = \arcsin(\Re e\{n_2\})$ from the Snell's law. Differently to what observed for germanium in [16, 46], in diamond the critical angle does not track the zeros of the sensitivity to the imaginary part of the dielectric function, instead, for the entire energy range is close to the region of maximum sensitivity. On the right panel of the same figure, instead, the modulus of the relative sensitivity to the real part of the dielectric function, calculated with the data mentioned above, is shown. Here, increasing the energy, the critical angle of incidence gets close to the maximum sensitivity.

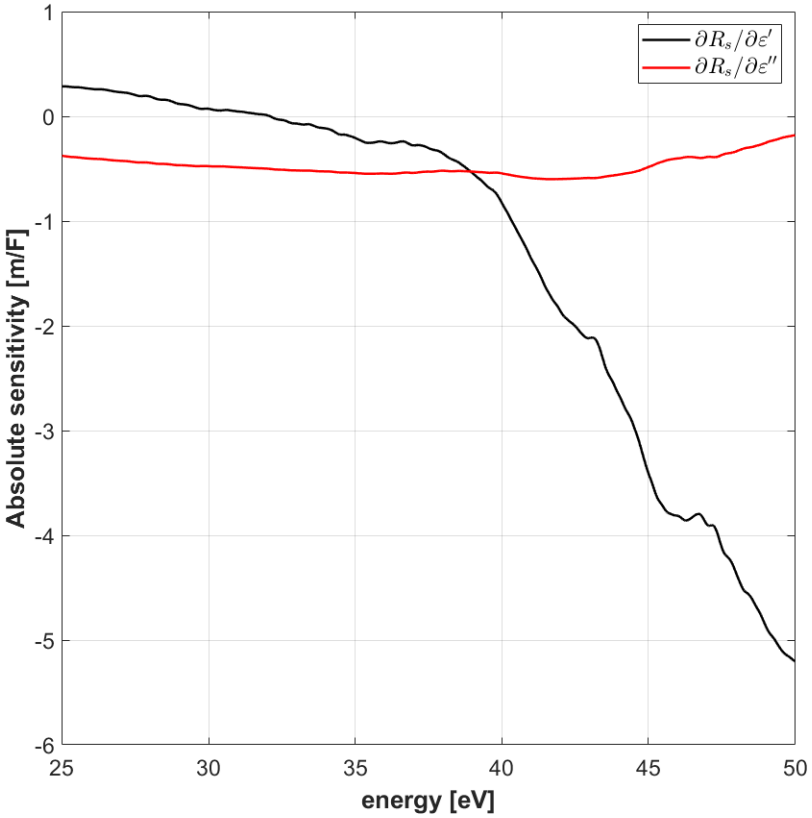

Figure 5.2: *Absolute sensitivity functions at 44.6° as function of the energy.*

The angle chosen for the experiment in Chapter 6 is 44.6°, close to the critical angle for 45 eV. This choice was driven by the idea of reproducing the results obtained in [11], where a significant increasing in absorbance was observed around 43 eV. The angle has been determined experimentally, starting from the calculated critical angle for 45 eV, then slightly modified to optimize the quality of the transient reflectivity

signal. Looking at the maps in Figure 5.1, this choice seems clearly lead to high sensitivity to variations of both the real and imaginary parts of the dielectric function in the energy region of interest. In Figure 5.2 the variation of the static reflectivity with respect to the real and imaginary part of the dielectric function at 44.6° is shown. At lower energies, both the real and imaginary parts of the dielectric function contribute at the same level to variations in the reflectivity, except for a region between 30 and 35 eV in which the sensitivity to ε' goes to 0, highlighting insensitivity of the reflectance to variation of the real part. At higher energies, the sensitivity to the imaginary part starts lowering and approaches zero, whilst the sensitivity to the real part increases significantly in absolute value. Following the reasoning in [16], this suggests that transient reflectivity variation at higher energies can be mainly explained by the real dielectric function, whilst at lower energies both contribute to changes.

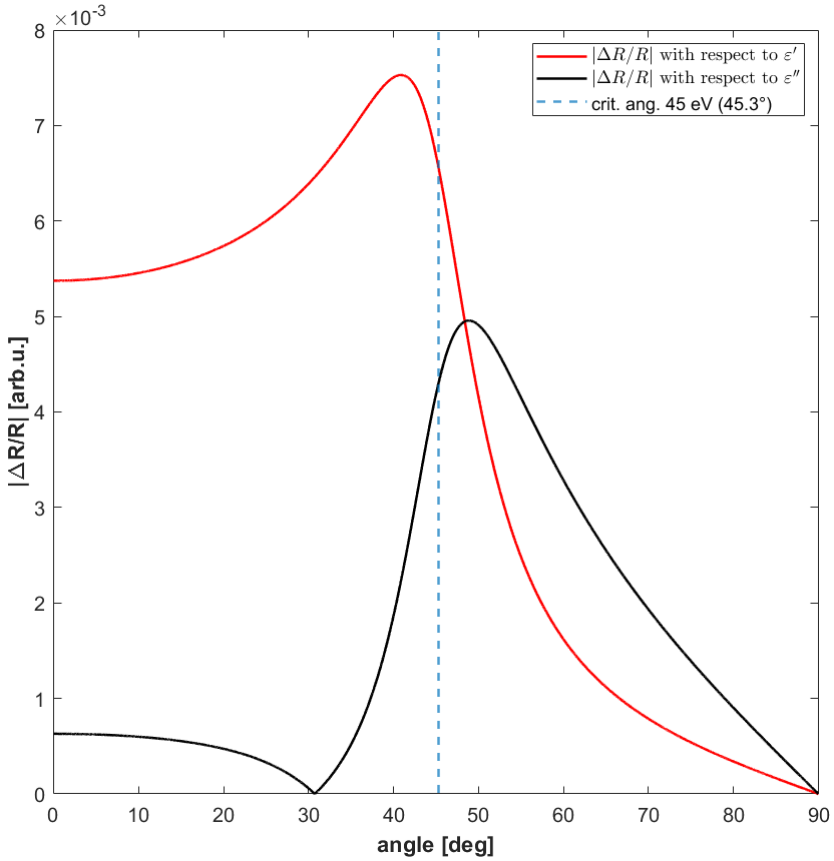

Figure 5.3: *Modulus of the transient reflectivity at 45 eV from diamond as function of the angle of incidence. Red curve and black curve are respectively to a variation in the reflectance with respect to the real and imaginary part of the dielectric function. The dashed light blue line corresponds to the critical angle for 45 eV calculated to be 45.3°.*

To conclude this section, Figure 5.3 shows the modulus of the transient reflectivity at 45 eV calculated with (5.7) with respect to a variation in a the real (red curve) and imaginary (black curve) part of the dielectric function, choosing $d\varepsilon = 0.0001$. As stated before, in case of complex refractive index, the reflectivity does not diverge in correspondence of the critical angle, that for 45 eV is equal to 45.3°. However, the transient reflectivity with respect to a variation in the imaginary and real part of the dielectric function both present a maximum, shifted of approximately 5° with respect to the critical angle. This confirms that working at total external reflection, by choosing the proper angle of incidence, i.e. the critical one, can enhance the transient reflectance signal.

5.2 Determination of the complex refractive index

As stated at the beginning of this chapter, the determination of the angle of incidence to be used in a transient reflectivity experiment is a key factor for a successful measurement. In fact, the angle that maximizes the sensitivity of the reflectivity to changes in the dielectric function must be chosen. With both methods illustrated above, it is necessary to know the multiangle static reflectivity or the complex refractive index of the sample considered. It is important to note that for the XUV range, and especially for recent advanced materials, data on refractive indices are not yet available in literature. In most of the cases, the determination of the complex refractive index is done by models, as the ones used for diamond in the previous sections. It is also possible to experimentally determine the complex refractive index to be more accurate. By measuring static reflectivity from a known sample at different angles of incidence and by reverting the Fresnel equation in (4.1), one can extract both the real and the imaginary parts of the refractive index. These types of measurements are typically performed at Synchrotron facilities all over the world, which, with respect to HHG pulses, allow to have higher photon flux, and as a consequence lower noise, and a wide energy range (from few eVs to hundreds of eVs). During my thesis, in order to collect data for further experiments in our laboratories, our team has performed such type of measurement at Elettra Synchrotron in Trieste (BEAR beamline [49]). Some preliminary results are reported in the next section.

5.2.1 Reflectivity measurements at Elettra Synchrotron

The reflectivity measurements here reported were performed at the BEAR beamline, which provides several spectroscopic tools, among which specular (reflectivity) and diffuse light scattering, soft X-ray excited fluorescence, ultraviolet and X-ray pho-

toemission spectroscopy (UPS-XPS) and X-ray Excited Luminescence (XEOL) [49]. This beamline allows to precisely control the beam position on the sample [50] and the light polarization state, and it is designed to be theoretically aberration free. Photon energy ranges between 2.7 eV and 1600 eV and typically the spot size is 30 x 100 μm wide, with a divergence lower that 20 mrad in both the dimensions.
Figure 5.4 reports the reflectivity of $LaVO_3$ at various angles of incidence with respect to the normal, ranging from 65° to 82.5°, considering grazing incidence. $LaVO_3$ is a perovskite material whose properties seem really promising for photovoltaic applications [51]; in fact, it shows high absorption in the solar spectrum range due to its optimal band gap of 1.1-1.2 eV, an efficient electron-hole separation, and a strong electron-electron interaction that can lead to the excitation of more than one free carrier per photon absorbed. However, the reflectivity in the XUV range has not been deeply studied yet. Two main deeps can be observed just above 40 eV and around 110 eV; the first one corresponds to the absorption edges M_2 and M_3 of Vanadium, and so to levels $3p_{1/2}$ and $3p_{3/2}$, whilst the latter to the absorption edges N_4 and N_5 (levels $4d_{3/2}$ and $4d_{5/2}$) of Lanthanum. There is also another peaked structure at 105 eV which probably is due to the formation of an exciton, but it must be further investigated. At this point, the reflectivity curves can be fitted using the minimiza-

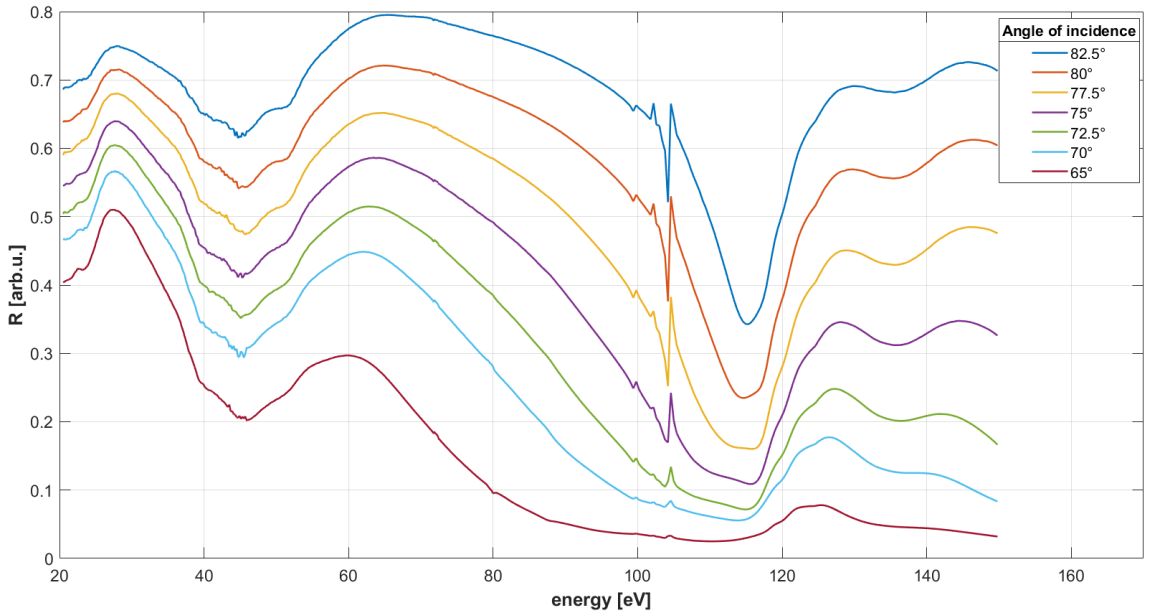

Figure 5.4: *Static reflectivity (R) of $LaVO_3$ at various angles of incidence with respect to the normal.*

tion of the residuals between experimental data and theoretical curves, that can be performed through the `lsqnonlin` MATLAB function. For this purpose, considering that the sample is in vacuum ($n_1 = 1$) and the magnetic permeability equal to 1 for

both the materials, the Fresnel coefficient in (4.1) can be further simplified in

$$r_s = \frac{\sqrt{1-\sin^2(\theta_1)} - \sqrt{n_2 - sin^2(\theta_1)}}{\sqrt{1-\sin^2(\theta_1)} + \sqrt{n_2 - sin^2(\theta_1)}}\,, \tag{5.8}$$

where θ_1, the angle of incidence, and r_s are known and the only remaining unknown is n_2, the refractive index of the sample. Multiple angles measurements allows the fit to be consistent. This procedure has been successfully applied to Germanium in [46]. Regarding diamond, this procedure was not necessary because of the availability of reliable calculations and data. However, this is not true for all the materials, especially for innovative compounds, that make necessary such measurement campaigns in order to properly design subsequent transient reflectivity experiments in the laboratories.

6 | Attosecond electron dynamics in diamond

In this chapter I will show the results of the attosecond transient reflectivity experiments performed on diamond.
The sample was provided by Delaware Diamond Knives [52] and it is cut along direction 100 according to Miller indices. Diamond is made of carbon atoms in the sp_3 ibridization tetrahedrally bonded. The *diamond cubic* structure, which actually takes its name from the diamond crystal structure, consists of two interpenetrating face-centered cubic (fcc) lattices displaced from each other along the body diagonal by one quarter of the diagonal length. The structure is reported in Figure 6.1 (left side),

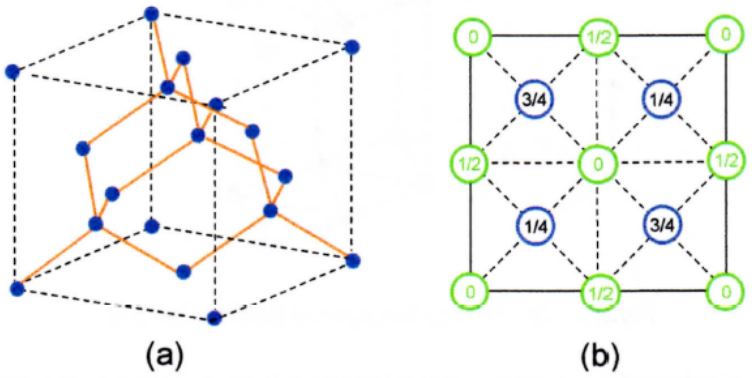

Figure 6.1: *(a) Diamond crystal structure, highlighting the tetrahedral bonds. (b) Atomic positions in the cubic cell projected on a cube face: numbers refer to the height of the atom with respect to the cubic edge and colors to the two different interpenetrating fcc lattices. [53]*

whilst the right side shows the atomic positions projected on a cube face: numbers correspond to the height above the cube face in unit of cube edge a and colors refer to the two different fcc lattices interpenetrating [53]. Due to the symmetry of the diamond cubic lattice, the projections on the faces are the same in all the directions. Diamond was chosen for this experiment with the idea of continuing the work in [11], where polycrystalline diamond was studied through attosecond transient absorption

spectroscopy. Here the maximum signal was found around 43 eV as an absorption increment oscillating at twice the fundamental frequency of the IR field. Differently from transient absorbance, transient reflectance allows to study electron dynamics not only in polycrystalline diamond, but also in monocrystals, impossible to be prepared thin enough for absorption. Moreover, studying reflectance, it is possible to access those spectral regions for which the transmission signal is too low to be detected.
The angle of incidence is 44.6° and its choice is explained in section 5.1. From the demonstrations in Chapter 4, it is possible to say that the spatial properties of the pulse have no influence on the actual angle of incidence of each spectral component. As highlighted before, the peculiarity of the setup of this experiment is to have two interaction regions, one with Argon in ToF spectrometer, used to temporally characterized both the XUV and the IR pulse, and one with the actual sample under investigation, that is diamond. This characteristics allows to precisely define the timing of the electron dynamics with respect to the IR pump that induces it. In the next sections, I will discuss both the signal coming from the ToF and from the diamond sample, relating one to each other to extract relevant information on the ongoing processes.

6.1 Attosecond streaking trace

Using the ToF spectrometer, it is possible to characterize both the IR and the XUV pulses. Photoelectron spectra measured at different delays between the two pulses generate the so-called *attosecond streaking trace* [28]. Following the reasoning exposed in [54], I will show that this trace is a direct measurement of the IR electric field.
Considering that the electric field is defined as the force exerted on a unitary-valued point charge, the direct measurement of the field must rely on the actual measurement of this force. To access this force $F = eE_{IR}$, the probe charge e must be instantaneously placed in the field, it means in a time interval $\tau_{probe} << T_0$, where T_0 is the period of the IR electric field. The probe charge (an electron) is obtained through the photoionization of the gas target by the XUV pulse, that, with its sub-femtosecond duration, satisfies also the temporal constraint required. For a linearly polarized wave, the variation in the momentum of the charge caused by the field can be expressed as

$$\Delta p(\overrightarrow{r}, t) = e \int_t^\infty E_{IR}(\overrightarrow{r}, t')\, dt' \tag{6.1}$$

$$= eA_{IR}(\overrightarrow{r}, t)\ , \tag{6.2}$$

where A_{IR} is the vector potential of the electric field

$$E_{IR}(\overrightarrow{r},t) = E_0\mathcal{E}_{IR}(\overrightarrow{r},t)\cos(kz-\omega_0 t+\phi)\ , \tag{6.3}$$

with E_0 being the maximum amplitude and $\mathcal{E}_{IR}$ the envelope of the pulse travelling along the z-direction with group velocity v_g and t=0 corresponding to the peak of the pulse. Knowing that

$$E_{IR} = -\frac{\partial A_{IR}}{\partial t}\ , \tag{6.4}$$

by measuring the momentum boost $\Delta p(\overrightarrow{r},t)$ imparted to the electrons by the electric field in the same position $\overrightarrow{r}$ at two different instants of time, $t_1 = t-\frac{\delta t}{2}$ and $t_2 = t+\frac{\delta t}{2}$ with $\delta t << t$, one can directly extract the electric field itself. In fact, approximating the derivative with the incremental ratio,

$$E_{IR} = \frac{\Delta p(\overrightarrow{r},t-\frac{\delta t}{2}) - \Delta p(\overrightarrow{r},t+\frac{\delta t}{2})}{e\delta t}\ . \tag{6.5}$$

Provided that the IR pulse can be reproducibly generated each time, repeating the measurement at different ionization instants t, we sample each time a different portion of the IR field, which then can be completely reconstructed. To proper sample the IR field, the electron probe must be also confined in space to a tiny fraction of the IR central wavelength; this requirement can be relaxed if the electron release is triggered by an XUV pulse propagating collineraly with the IR pulse. A schematic representation of the measurement is shown in Figure 6.2.

The photoelectron kinetic energy, using Taylor series approximation stopped at the first order, can be expressed as

$$\begin{aligned} U_k = \frac{p^2(\overrightarrow{r},t)}{2m} = \frac{[p_i+\Delta p(\overrightarrow{r},t)]^2}{2m} &= \frac{p_i^2}{2m}\left[1+\frac{\Delta p(\overrightarrow{r},t)}{p_i}\right]^2 \\ &\backsimeq \frac{p_i^2}{2m}\left[1+2\frac{\Delta p(\overrightarrow{r},t)}{p_i}\right] \\ &\propto \frac{p_i}{m}\Delta p(\overrightarrow{r},t) \propto \frac{ep_i}{m}A_{IR}(\overrightarrow{r},t) \end{aligned} \tag{6.6}$$

being directly proportional to the IR vector potential. For this reason, the center of mass CM of the photoelectron trace $S(\mathcal{E},\tau)$ for each delay τ, defined as

$$\mathcal{E}_{CM}(\tau) = \frac{\int \mathcal{E}\ S(\mathcal{E},\tau)d\mathcal{E}}{\int S(\mathcal{E},\tau)d\mathcal{E}}\ , \tag{6.7}$$

as a first approximation oscillates as the IR vector potential A_{IR}.

With the help of Figure 6.3, we can compare the photoelectron trace in presence

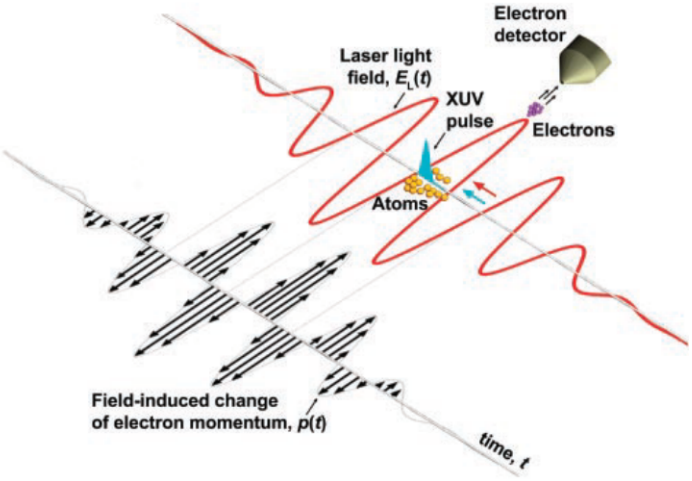

Figure 6.2: *Schematic representation of the measurement of an attosecond streaking. The XUV probe pulse ionized the atoms generating electrons, which are then subjected to a variation in their momentum caused by the IR field. The change in momentum is the actual observable to be measured. [54]*

of the IR field (right) and without the IR pump (left), as function of the absolute IR delay (delay step = 0.25 fs) and of the photoelectron energy. The photoelectron trace on the left maps the XUV photon spectrum, with an energy shift due to the ionization potential of the gas used (Argon, $I_p = 15.76$ eV) and its photoionization cross-section. Moreover, to have a clean streaking trace, electrons must come from only one orbital, in order not to have different signals superimposing. On the right, one can appreciate the delay-dependent energetic shift caused by the IR pump field.

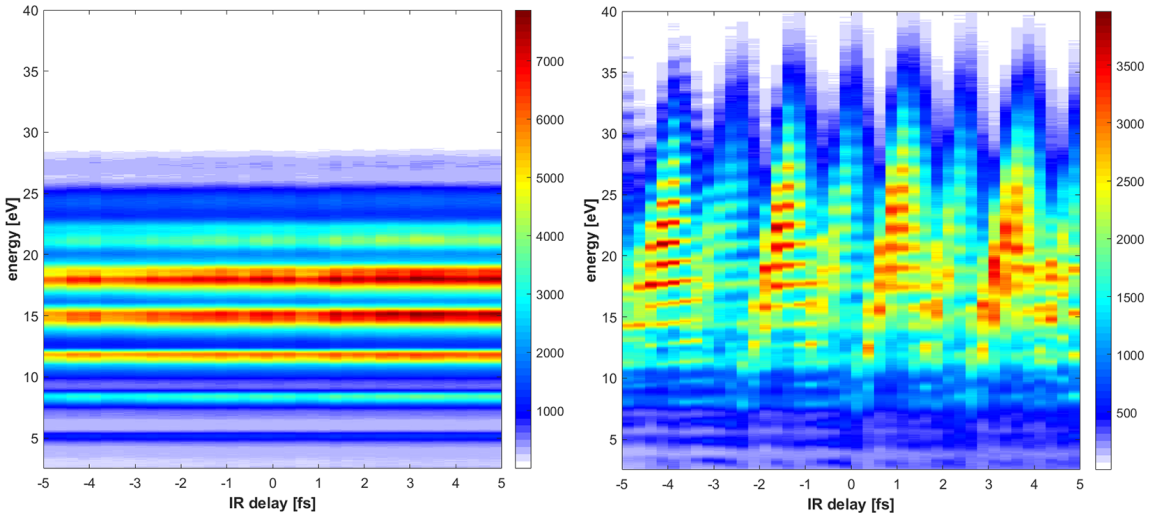

Figure 6.3: *Photoelectron trace [arb.u.], obtained in Argon with a ToF pressure of $7.7{\cdot}10^{-6}$ mbar, in absence (left) and in presence (right) of the IR pump.*

Figure 6.4 shows enlarged the streaking trace in Figure 6.3 (right) with superimposed the the extracted center of mass (black curve). It can be observed that there are some secondary weak peaks due to the operational conditions of the DOG. Here we are using this technique with trains of pulses and without CEP stabilization: this leads to the generation and superposition of a main XUV train, whose pulses are generated every period and a second train, usually weaker in intensity, whose pulses are separated by half a cycle. Unbalancing in the delay introduced by the waveplates and in the amount of second harmonic generated by the BBO results in unbalancing in the superposition of the two trains, which reflects also in the streaking trace causing a shift on the actual A_{IR} and making the approximation with the center of mass less accurate. The use of the center of mass is just a first step towards the analysis of the

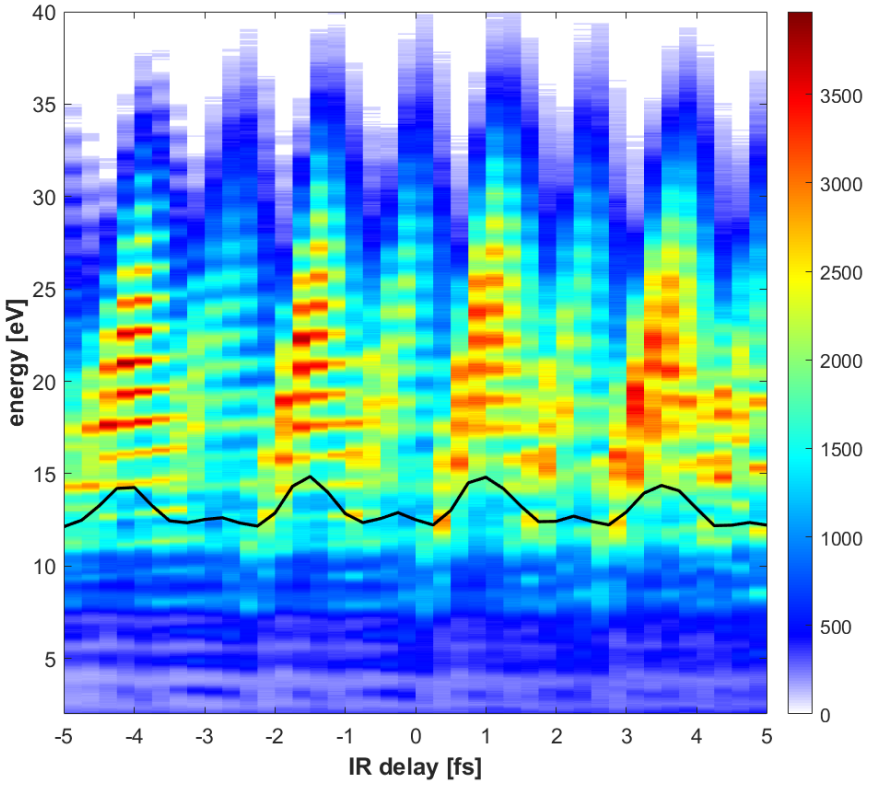

Figure 6.4: *Detail of the streaking trace in Figure 6.3 (right) obtained in Argon (ToF pressure of 7.7·10^{-6} mbar) with the extracted center of mass (black curve), a good approximation of the IR vector potential.*

trace; there are more complex models able to extract the actual vector potential with a higher degree of precision, providing also a full characterization of the attosecond XUV probe pulse (see Frequency-Resolved Optical Gating for Complete Reconstruction of Attosecond Bursts (FROG-CRAB) [29] and extended Ptychographic Iterative Engine (ePIE) [30]). Another interesting method serving this purpose is called *analytical chirp evaluation (ACE)* and it is fully described in [55].

6.2 Transient reflectance trace

In this section, I will discuss one of the transient reflectivity trace obtained from diamond; this trace has been chosen as reference also for the analysis of the attosecond timing of the IR-induced effects, which is explained in the following section. The transient reflectivity trace is given by (5.6). From the experimental point of view, the two XUV spectra are acquired for each delay, one with the IR pulse passing through the beamline and reaching the sample and the other blocking it with the 1-Hz-frequency shutter (see 2.2.1). The transient reflectivity trace obtained in this way can be also called *pump-probe spectrogram*.

Figure 6.5 shows the transient reflectance trace used as reference for the analysis illustrated below. The trace was obtained mediating over 100 acquisitions of the XUV camera with an exposure time of 0.2 s. The delay axis spans 10 fs with steps of 250 as. The energy of the IR pulse is set to 30 μJ by controlling the dedicated motorized iris. As one can notice, the trace is strongly affected by noise, which limits the actual sensitivity of the experiment. A major noise component is due to the source itself, in fact the high non-linearity and instability of HHG process result in a spectral noise strongly correlated to the XUV spectral fluctuations. To solve this

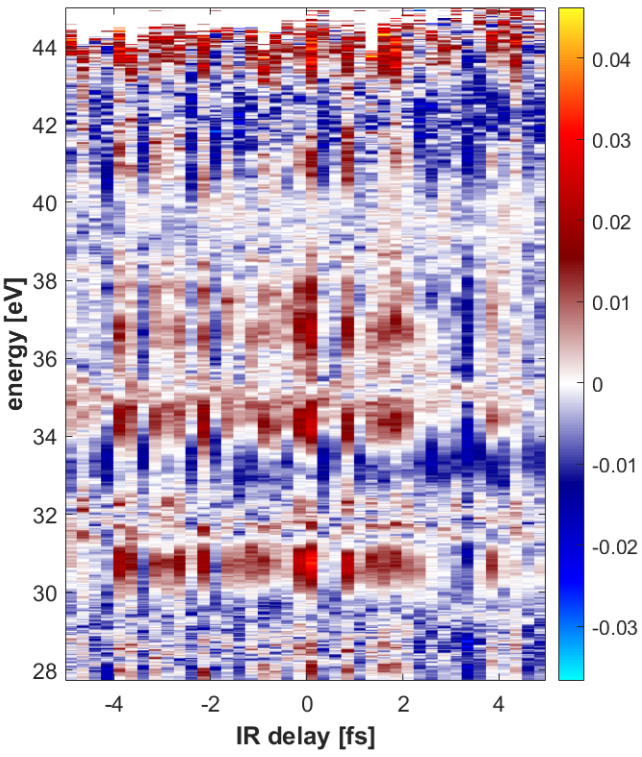

Figure 6.5: *Raw transient reflectance trace from diamond. It is obtained mediating over 100 acquisition of the XUV camera with an exposure time of 0.2 s. The delay axis spans 10 fs with steps of 250 as. The energy of the IR pulse is set to 30 μJ.*

issue, a very efficient procedure, called *edge-pixel referencing*, is presented in [56]. Thanks to the large bandwidth of the XUV beam, the transient reflectivity signal spans over a bandwidth much larger than the one in which a pump-induced signal is present. Since the spectral noise is correlated, the signal-free regions contain information on the noise distribution of the whole spectrum, including the regions containing the pump-induced signal. The first ones, called *edge-pixels* regions, will be used to remove fluctuations in the *signal-pixels* regions. The method relies on the selection of the edge pixels from the transient reflectivity trace and on the construction of the *correlation matrix*, that is characteristic of each measurement and based on a calibration dataset obtained from pump-off probe spectra. In the case of correlated noise, this procedure provides the best noise correction. Nonetheless, the correct selection of the edge pixels is crucial: in fact, if a pump-induced signal is present in those regions, this approach can create artefacts. For this reason, comparing the edge-reference result with the result from a different noise-suppression method can be useful. To this purpose, singular-value decomposition is usually adopted.

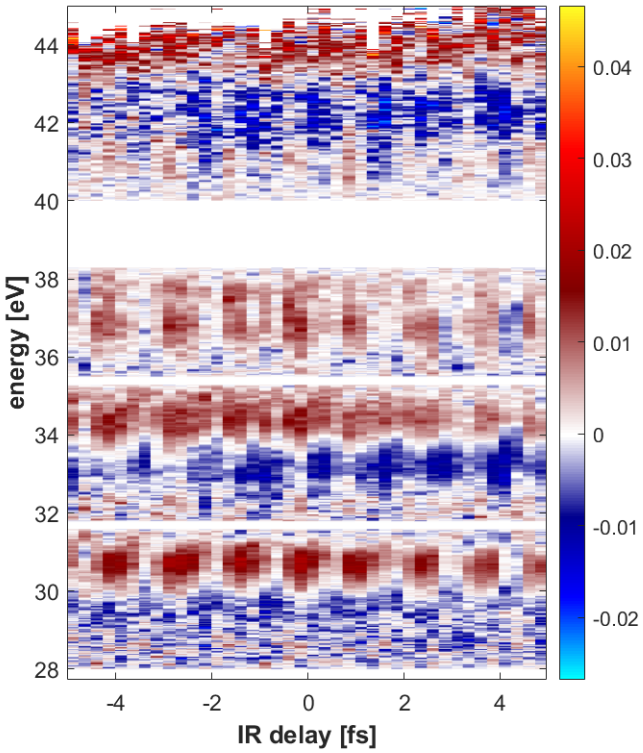

Figure 6.6: *Transient reflectivity trace of Figure 6.5 after the edge-pixel referencing procedure.*

For the trace reported in Figure 6.5, four edge-pixel regions has been chosen: from 27.7 (minimum energy detected) to 28 eV, from 31.6 to 31.8 eV, from 35.3 to 35.5 eV

and from 38.3 to 40 eV. The result is shown in Figure 6.6. Thanks to this procedure, pump-induced oscillations at double the frequency of the IR field (≈ 0.75 PHz, period ≈ 1.3 fs) are clearly visible between 30 and 32 eV and above 34 eV. These features correspond to a reflectance increment, whilst the in-between region shows a decrement.
Streaking trace and transient reflectivity spectrogram are now ready to be used for a combined analysis, which aims to extract, with a sub-femtosecond resolution, the energy-dependent time delay of the pump-induced signal with respect to the vector potential that generates it. This step will be detailed in the next section.

6.3 Extraction of the energy-dependent phase delay

The aim of this section is to show how it is possible to combine the information provided by the streaking trace and the transient reflectivity trace. Not to forget, the main purpose of this type of experiment is to study pump-induced electron dynamics in diamond through the change in reflectance of the XUV pulse impinging on the sample. Provided that the IR field induces a change in the dielectric function that translates into a change in the reflectance, a relevant analysis consists in the extraction of the phase difference -thus, of the time delay- between the squared modulus of the vector potential and the oscillations at the same frequency in the transient reflectance trace. This procedure has been successfully applied for transient absorbance experiments in [13] and [57], and for transient reflectance traces in [12]. Here I will follow the same method.
The first step is the filtering of the traces around the frequency of interest. The streaking trace, being directly proportional to the IR vector potential centered at 800 nm, must be filtered around the IR central frequency f_0 that is 0.375 PHz. Practically, this translates into the Fourier transform of the "raw" center of mass extracted using (6.7) multiplied by an appropriate super-Gaussian filter and finally anti-transformed. Regarding the transient reflectance trace, we are interested in studying oscillations at twice the optical frequency of the IR pump, it means at 0.750 PHz. The procedure, then, is the same as above.
The energy dependent phase delay between the transient reflectivity spectrogram (5.6) and the simultaneously measured streaking trace can be directly extracted multiplying the filtered Fourier transform of $\Delta R/R$ with the complex conjugate of the Fourier transform of the squared modulus of the IR vector potential. The modulus of this product has a peak at the shared oscillation frequency of the two signals and

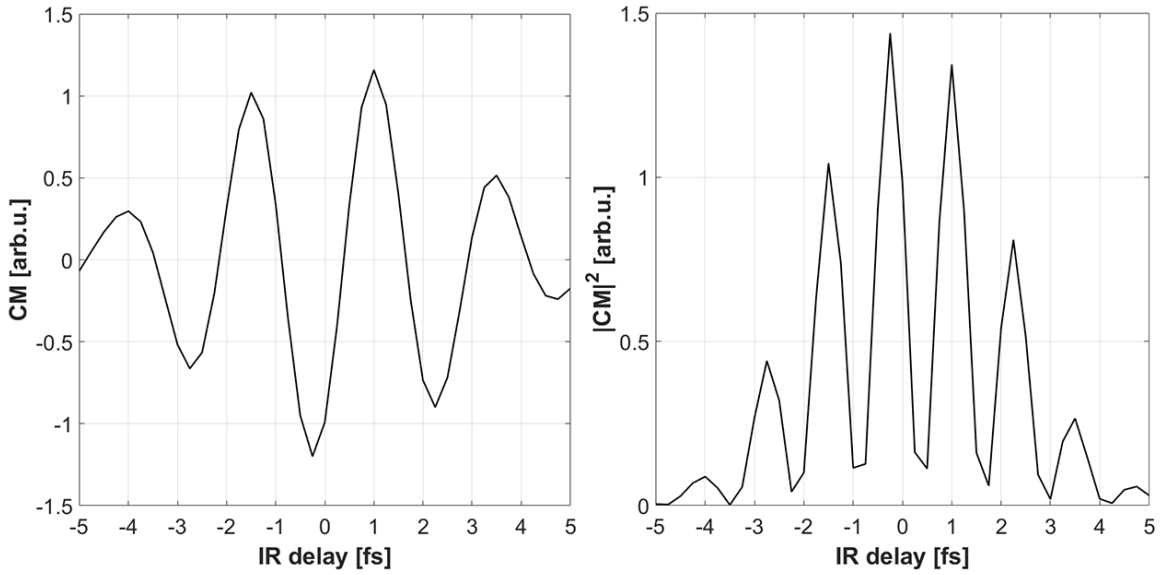

Figure 6.7: *Center of mass extracted from the reference streaking trace and filtered around f_0 (left) and its squared modulus (right). The center of mass is a good approximation of the IR vector potential A_{IR}.*

its phase corresponds to the phase difference we are looking for [58].

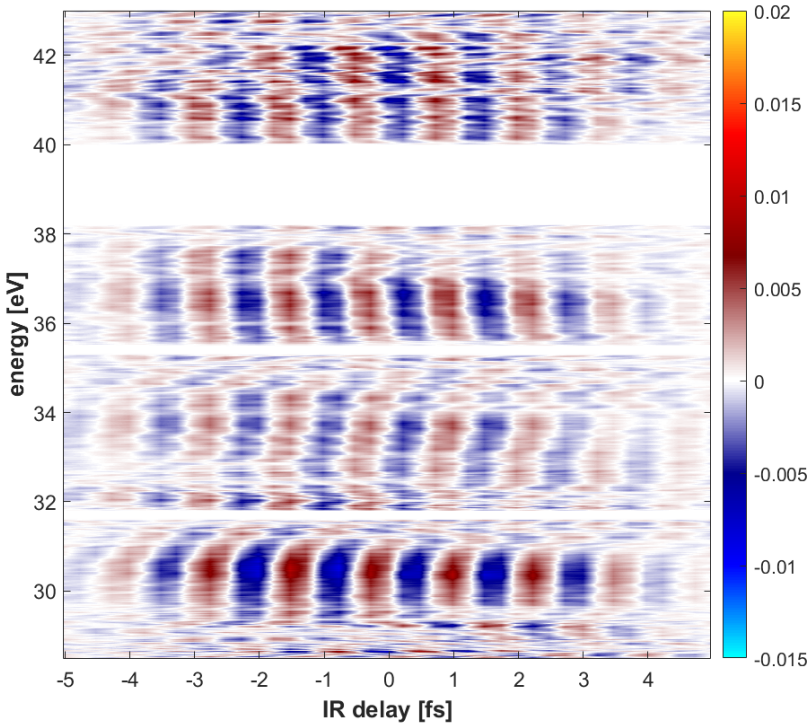

Figure 6.8: *Transient reflectance trace of Figure 6.6 filtered around $2f_0$.*

In Figure 6.7, the center of mass extracted in Figure 6.4 filtered around f_0 (left) and its squared modulus (right) as function of the absolute delay of the measurement. In

Figure 6.8, the transient reflectance trace of Figure 6.6 filtered around $2f_0$ is shown. A final comment about the procedure concerns the time-zero calibration. In order to directly compare the phase delay extracted with the $\Delta R/R$ trace, we must set the pump-probe delay zero, i.e. the instant of temporal superposition of the two. Provided that oscillations go as the squared modulus of the vector potential, a proper choice is one of its zeros. However, the center of mass is just an approximation of the vector potential and it becomes less accurate in presence of satellite pulses, as in our case. As one can notice, the zero of the delay axis does not correspond perfectly to the closest zero of the the function, it differs from it of about 0.25 fs, which corresponds to the additional propagation delay between the two foci of the beamline [17].
Figure 6.9 shows the mean value of the phase delay, extracted from four measurements at the same conditions as the reference shown above, with the corresponding standard deviation (black shaded area) and superimposed to the reference transient reflectance signal reported in Figure 6.8. In the central and lower part of the trace,

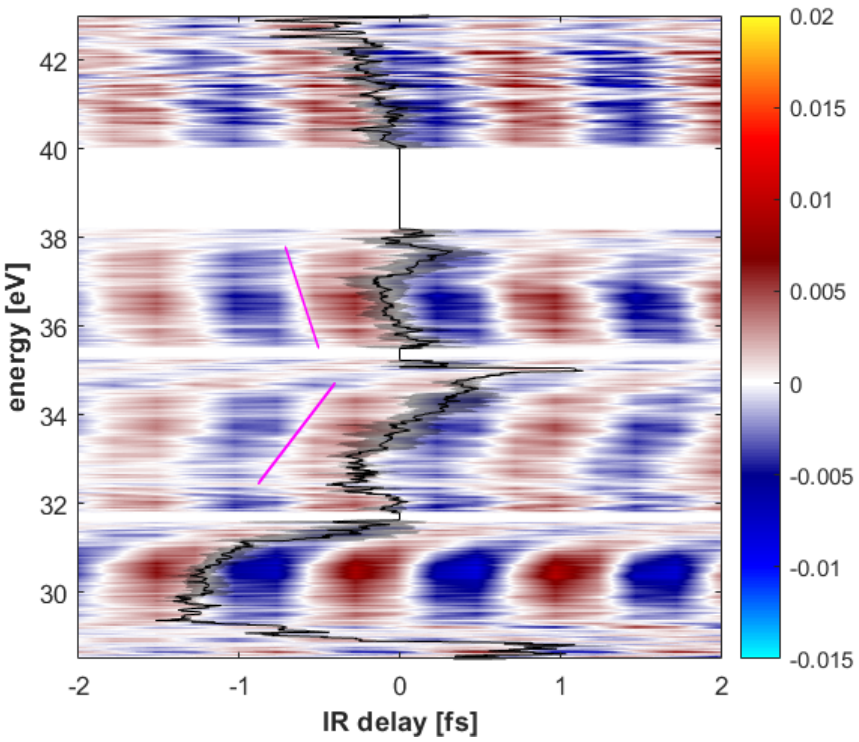

Figure 6.9: *Mean value of the phase delay extracted from four measurements (black curve) with the corresponding standard deviation (black shaded area), superimposed to the transient reflectance trace used as reference and reported in Figure 6.8. The two fuchsia lines highlight the V-shape, usually associated to the dynamical Franz-Keldysh effect.*

it can be noticed a V-shape (highlighted by the two fuchsia lines), similar to those in [11] and [12] even though less pronounced. This shape is usually associated to the

dynamical Franz-Keldysh effect (DFKE) [10]: the time-dependent IR field causes a sudden change in the absorption and reflection that, according to theory, is associated to a change in the electronic band structure and in the density of states. Figure 6.10 from [57] will help in explaining this effect.

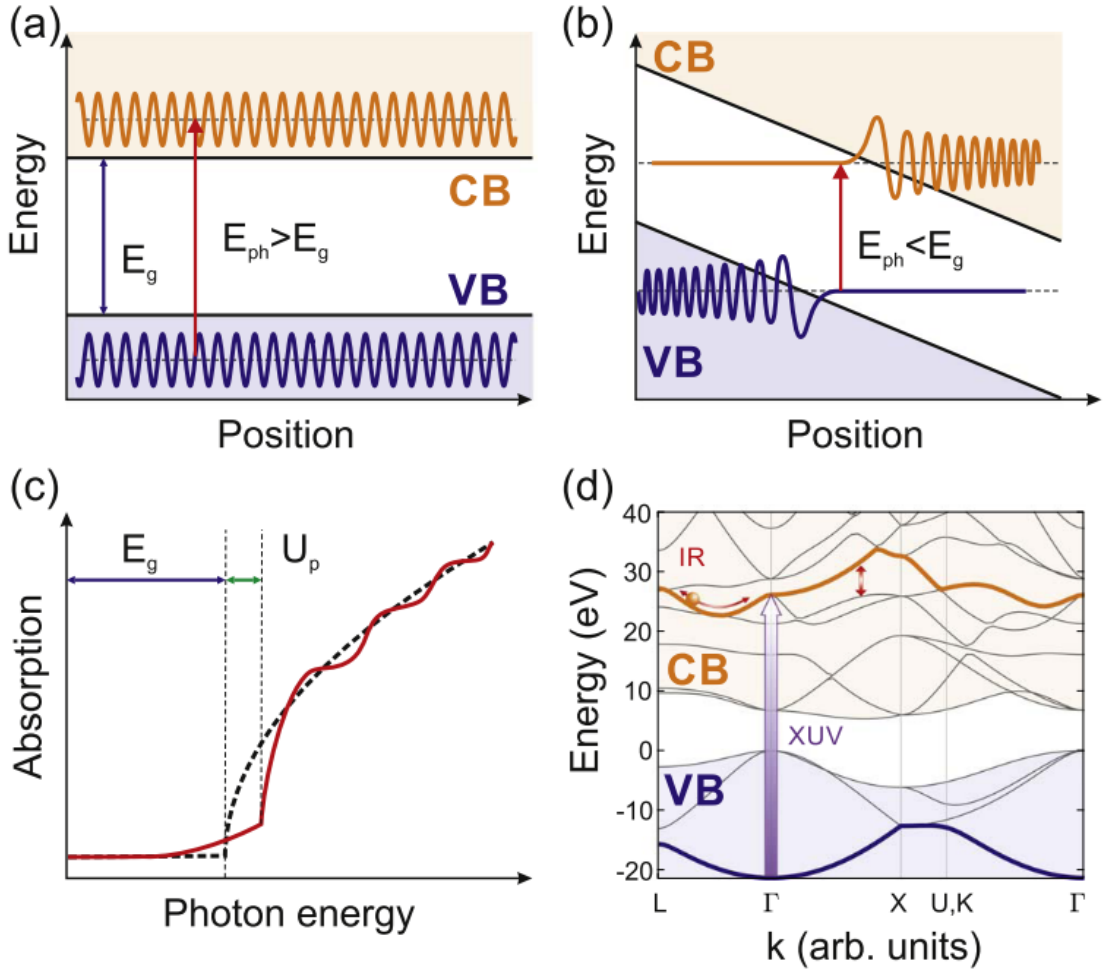

Figure 6.10: *Illustrated explanation of the dynamical Franz-Keldysh effect in diamond from [57].* (a) *Two electronic states in the VB and CB whose wavefunctions are periodic Bloch states; absorption occurs only for photon energies higher than the energy gap.* (b) *Effect of an external perturbing field which causes the bending of the energy bands; the electron wavefunctions are now Airy functions. Transitions to the conduction band are possible also for photon energies lower than the energy gap.* (c) *Schematic of the absorption profile in the static case shown in frame* (a) *(black dashed curve), and in case of DFKE (red curve), with non-zero absorption below the energy gap proportional to the ponderomotive energy of the field and oscillations at higher photon energies.* (d) *Diamond band diagram highlighting the transition from band 1 to band 11, the main involved in [11]. When* $\gamma_a \approx 1$*, the IR field can either accelerate the electron in the same sub-band (intra-band motion) or inject it to another sub-band (inter-band motion).*

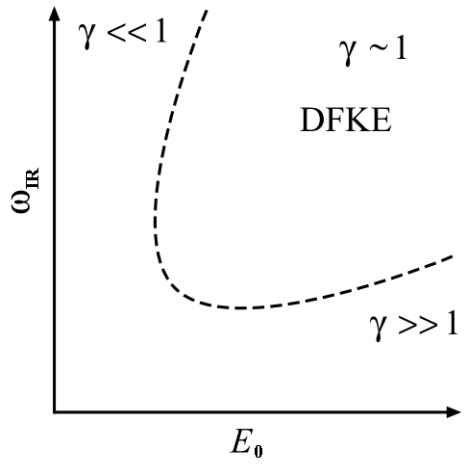

Figure 6.11: *Schematic map of the electro-optic phase space as function of the amplitude and frequency of the IR perturbing field. The three different regimes are highlighted ($\gamma = \gamma_a$). Adaptation from [59].*

The presence of an external oscillating field causes a bending of the energy bands, similar to what happens in the HHG process to the Coulomb potential of the atoms involved. The electron wavefunction (Bloch state), shown in the sub-plot *a*, becomes an Airy function, which differs from a plane wave because of a tail extending into the band gap (sub-plot *b*). This means that an electron can jump form the valence to the conduction band with and energy that is lower than the normal band gap, shifting the absorption edge (frame *c*). Moreover the absorption spectrum (and symmetrically the reflection) shows energy oscillations above the absorption edge dependent on the external field. DFKE is only one of the possible light effects in condensed matter, the dimensionless adiabaticity parameter γ_a [59] can help in classifying different mechanisms according to the theoretical description (classical/quantistic) needed to explain them. It is defined by

$$\gamma_a = \frac{U_p}{\hbar\omega_{IR}} \,, \tag{6.8}$$

where U_p is the ponderomotive energy (see equation (1.7)) and $\hbar\omega_{IR}$ the energy of the incoming IR photon, which triggers the effect. Three different situations and regimes can be identified and the schematic map in Figure 6.11 summarizes them as a function of the frequency and of the amplitude of the incoming IR field. The situation in which $\gamma_a \gg 1$ corresponds to perturbative theory and a classical description of the field interaction with matter, where the motion of the electrons is not dominated by the external field (intra-band motion), whilst $\gamma_a \ll 1$ corresponds to quantum phenomena such as multiphoton absorption (inter-band motion). The in-between situation with $\gamma_a \approx 1$ is associated, among others, with the DFKE, which requires

the combination of quantum and classical theories to be explained. This means that the physical mechanism taking place cannot be described completely neither by vertical inter-band transitions nor by intra-band motion alone: while the XUV pulse probes the transition between VB and CB, the IR can either accelerate the electron in the same sub-band (intra-band motion) or inject it vertically to another sub-band (inter-band motion) [57]. This mechanism is shown in the sub-plot *d* of Figure 6.10 with respect to the transition from band 1 to band 11 of diamond, which are the main involved in the experiment illustrated in [11].

6.4 Interpretation of the energy-dependent phase delay

Theoretical simulations are usually carried out to validate and support the interpretation of the experimental results. In our case, simulations are currently under development. Nonetheless, we can still try to make some considerations following the reasoning in [11]: these experiments on diamond should be considered complementary to the ones there presented.
Complete simulations on the electron dynamics taking into account also the effects induced by the dynamics of pump and probe pulses are based on the *time-dependent density functional theory (TDDFT)* coupled with Maxwell equations [60]. This method allows to directly simulate and reproduce the transient reflectance trace. However, some preliminary considerations can be done starting from the Bloch states of diamond and their contributions to the static dielectric function. This operation allows to have a first indication on the bands involved in the transitions and generating the transient features measured in the experiment.

In Figure 6.12, the diamond Bloch states depicted in the energy/momentum space (left) and the corresponding density of states DOS (right) [11] are reported. Here, few states are highlighted in different colors: the lower ones are states 2, 3, and 4 in the valence band (VB), whilst, the upper ones are states 9, 10, and 11 in the conduction band (CB). Considering that the main features of the transient reflectance trace are between 30 and 34 eV, the transitions from the valence states highlighted to the conduction ones, that imply an energy difference corresponding to this amount, are good candidates to explain them. Once identified the possible states involved, we have to investigate their effect on the static dielectric function through orbital decomposition. Differently from what is explained in [11], here we have to take into account also the effect on the real part of the dielectric function. Recalling Figure 5.2, in the energy region we are interested in, both imaginary and real parts of ε contribute to the

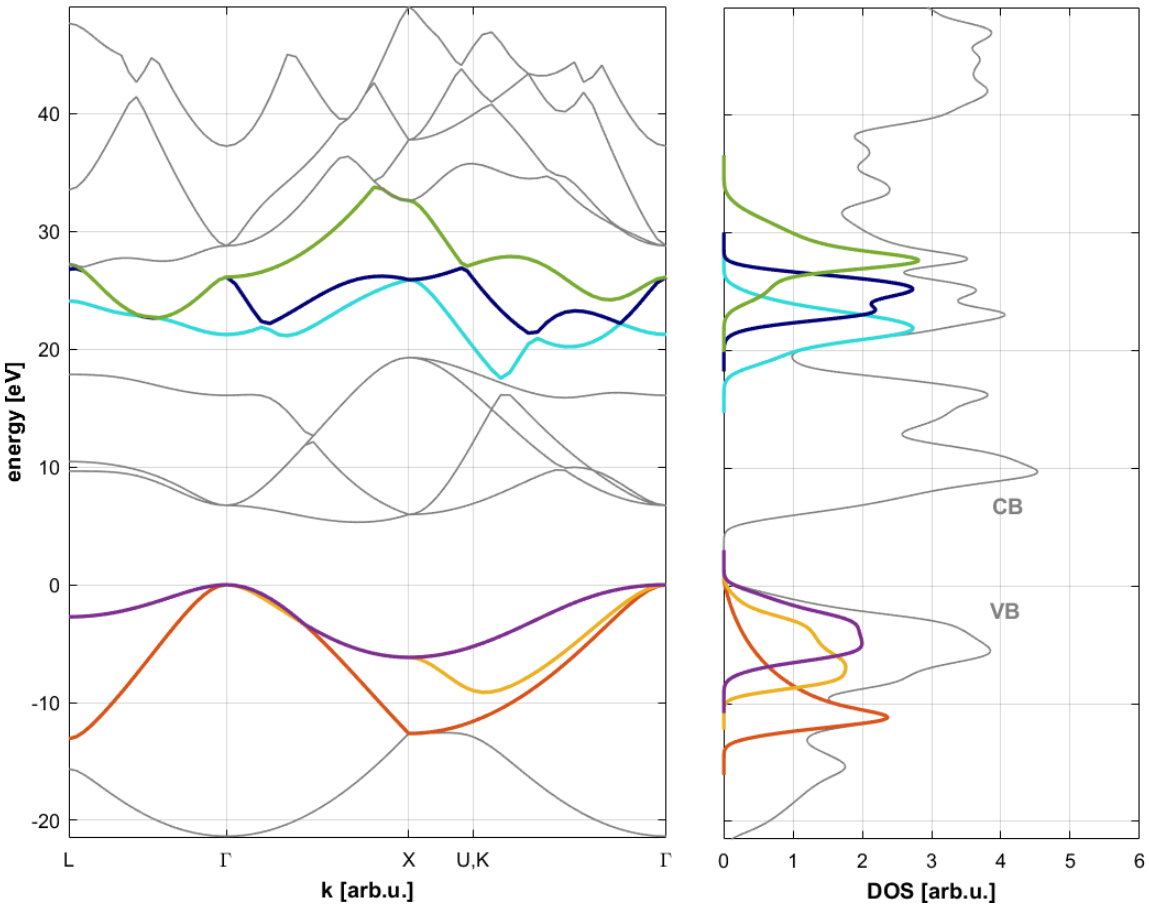

Figure 6.12: *Block states of diamond (left) and the corresponding density of states (right). Colored curves correspond to the states possibly involved to describe the features observed in the transient reflectance trace. In the valence band (VB), these are states 2, 3, and 4 and in the conduction band (CB), states 9, 10, and 11. Adaptation from [11].*

variation of the reflectance. For example, we can consider in Figure 6.13 the orbital decomposition of the imaginary part developed for the above-mentioned work we have used as reference. In sub-picture *a*, the total contribution of transitions from the four valence bands; in sub-pictures *b* to *e* decomposition of each valence state contribution into individual transitions to the conduction states from eight to fifteen, where bands 9, 10 and 11 are highlighted with the same colors as Figure 6.12. Focusing on the region between 30 and 35 eV, where the transient reflectance trace in Figure 6.6 shows the $2\omega_{IR}$-oscillations we are interested in, the signal from valence band two is sensibly higher suggesting major contribution from this band coming from transitions to band 9. A bit smaller contribution seems coming from band 3 (d) and band 4 (e), whose decomposition between 30 and 35 eV is dominated by transitions to bands 10 and 11. The analysis regarding the real part of the dielectric function must be carry out from the beginning it is not possible to provide any insights without calculations.

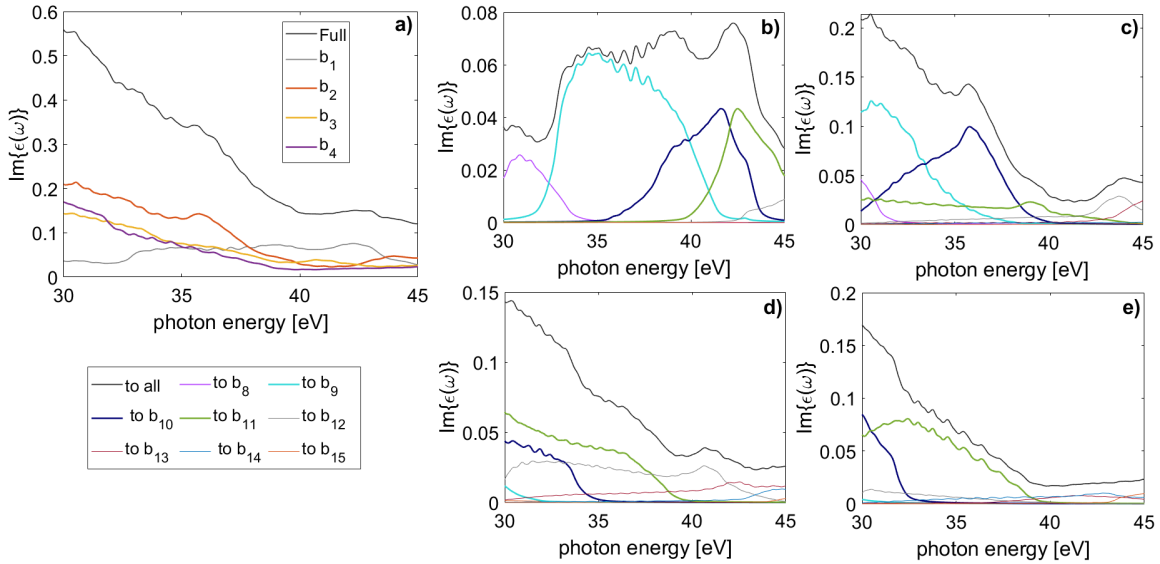

Figure 6.13: *Decomposition of the imaginary part of the dielectric function into the contribution from each valence band (a) and further decomposition of each valence band (1 to 4) into individual transitions to the conduction states 8 to 15 (b)-(e). Adaptation from [11].*

Another point to be investigated is the role of the temporal properties of the probe pulse in the electron dynamics, i.e. if its finite temporal duration can have an impact on the dynamics observed. Usually, the probe pulse has not an impact as shown in [11] and it can simply be treated as a small perturbation.

These experiments on diamond, according to these preliminary observations and discussions, seem to agree with the results obtained in absorbance for polycristalline diamond [11], in particular regarding the dynamical Franz-Keldysh effect. However, in order to properly analyze transient reflectance trace, other aspects must be considered. For example, working at total external reflection means that the XUV probe pulse behaves as an evanescent wave at the interface and its propagation time must be taken into account too. Moreover, considering that the probe penetrates in the sample only for few nanometers, as shown in Figure 4.8, also the sensitivity to the surface must be further investigated. Without claiming full comprehension in the data interpretation, the present discussion must be considered only as a starting point for a more accurate analysis. The group is working hard to reach this goal as soon as possible.

Conclusions

In this thesis, I have discussed the key ingredients for an attosecond transient reflectivity experiment, starting from the laser source up to preliminary data obtained with a diamond sample.
Regarding the setup, after a general description, given the planned beamline upgrade in order to study polarization-dependent processes, I presented the development and realization of a polarimeter for IR radiation. A detailed procedure is here reported, as it will become a routine measurement in the near future.
Regarding reflectivity measurements, as a first step, a comprehensive discussion about the static reflection of a pulse on a plane interface is provided. The analysis proposed starts from Fresnel equations and takes into account both spatial and temporal properties of a Gaussian pulse impinging on a plane surface, demonstrating that the spatial dispersion does not play a relevant role in the correct definition of the actual angle of incidence for each component. In fact, if we consider all the components impinging the plane interface with the same angle, in a sort of plane wave approximation, the final result on the reflected and transmitted pulses does not change. The model is used then to describe the interaction of the IR and XUV pulses with a diamond target, to give an insight on the physical processes taking place in the sample under investigation. However, a complete model, exempt from idealities, must take into consideration a rough surface and the scattering deriving from it. In this case, it is expected that the spatial properties of the pulse could play a major role. Further investigation is necessary to discern this point.
The choice of the angle of incidence on the sample is a crucial aspect of a transient reflectivity experiment. Following the state-of-the-art procedure, I analyzed the sensitivity function describing how a variation of the real and imaginary parts of the dielectric function ε influences the reflectance. At the chosen angle of 44.6°, in the energy range below 40 eV, variations of both imaginary and real parts of ε must be taken into account for the analysis.
Another relevant aspect is the determination of the refractive index of the material under investigation. Not to rely only on mathematical simulations, it is also impor-

tant to experimentally define the complex refractive index of the sample in the XUV range. This can be done at Synchrotron facilities. As a team, during my stay, we have performed static reflectivity measurements at Elettra in Trieste, to study new samples. I presented here the preliminary results for $LaVO_3$, an interesting compound for photovoltaic applications, that allow the identification of the absorption edges M_2 and M_3 of Vanadium and the edges N_4 and N_5 of Lanthanum. The fitting of these curves, taken at various angles, will allow to extract the complex refractive index of the material.

In light of what is discussed in the previous chapters, the final one presents the experimental results of transient reflectivity on diamond. Given the double-foci geometry of the setup, first of all, it is provided an analysis of the streaking trace through the determination of the IR vector potential. Regarding the transient reflectance trace, a noise suppression technique is explained, which enables a drastic increase in sensitivity highlighting oscillating features between 30 and 34 eV. The analysis continues with the extraction of the phase difference between the squared modulus of the IR vector potential and the $2\omega_{IR}$-oscillations in the reflectance trace. An attempt of physical explanation is provided following [11]. Probably the V-shape of the phase suggests the occurrence of the dynamical Franz-Keldysh effect. The inspection of the band structure of diamond, instead, suggests the involvement of valence bands 2, 3 and 4 and transitions to the conduction bands 9, 10, and 11. Any final consideration of the physical processes induced by the IR in this configuration is postponed until the development of adequate theoretical calculations.

For the future, in order to further develop the present work, several steps are planned, especially from the theoretical and analytical point of view, starting from the modeling of the interaction of a pulse with a rough surface, up to a more accurate analysis of the streaking trace and, as a consequence, of the transient reflectivity features supported by adequate theoretical calculations. However, the results obtained up to now can already confirm once again how powerful can be the transient reflectivity spectroscopy in investigating electron dynamics, otherwise not observable. Even though the state-of-the-art research does not allow yet to have an immediate application for these results, in the next future, once identified how a material reacts to light with defined spectral and temporal properties, a possible application is the implementation of the proper light source in order to induce a precise and desired effect, ideally leading to an ultrafast optical control of the electronic dynamics.

Appendix A.
Beckmann-Spizzichino model

The modelling of the scattering from a rough surface is a complex topic and several methods can be considered, depending on the degree of approximation that want to be adopted. I present here one of the possible model, that is called the *Beckmann-Spizzichino model* from the name of the two developers. This section is not meant to be exhaustive in the description and derivation of the model, but it is here proposed to give the flavour of the complexity of the topic.
The Beckmann-Spizzichino model [48] uses physical optics to describe the reflection of plane waves from smooth and rough surfaces. It relies on few approximations:

- the incident wave is a plane wave perpendicularly polarized with respect to the surface;

- the radius of curvature of surface irregularities is large compared to the wavelength of incident light (Kirchoff's assumption), thus the electric field and its derivative with respect to the normal can be approximated with the field that would be present on a tangent plane at that point;

- the surface is assumed to be a perfect conductor; the authors highlight that the surface roughness has a greater effect on the scattered field on than the electrical properties of the surface medium;

- masking and shadowing of surface points by adjacent surface points is neglected as well as multiple scattering (light is reflected only once);

- the surface is modelled as a random process, described by the statistical distribution of its height above a certain mean level. The height coordinate h of the surface is a random function of x and y and the shape of the surface is

determined by the probability distribution of h, that is the normal distribution

$$p_h(h) = \frac{1}{\sqrt{2\pi}\sigma_h} e^{-\left(\frac{h^2}{2\sigma_h^2}\right)} \tag{6.9}$$

where σ_h is the standard deviation and represents the roughness of the surface; the mean value is $< h >= 0$ and the correlation distance is T.

Figure 6.14 shows the geometry of the problem; the model, indeed, allows to calculate the instantaneous scattering at a point P in the direction $\overrightarrow{k_2}$ of an incident plane wave with propagation direction $\overrightarrow{k_1}$; θ_r and ϕ_r describe all the possible directions of reflection in the three-dimensional space. Following the calculations, one can retrieve the mean scattered power of a plane wave impinging on a rough rectangular surface of area $A = 2X \cdot 2Y$ with an angle of incidence θ_i in the arbitrary direction (θ_r, ϕ_r) as

$$< E_2 E_2^* >=< |E_2|^2 >= \frac{E_0^2 A^2 \cos^2(\theta_i)}{\lambda^2 R_0^2} e^{-g} \left(\rho_0^2 + \frac{\pi T^2 D^2}{A} \sum_{m=0}^{\infty} \frac{g^m}{m! m} e^{-\frac{k_{xy}^2 T^2}{4m}} \right) \tag{6.10}$$

where

$$g = \left(2\pi \frac{\sigma_h}{\lambda} (\cos\theta_i + \sin\theta_r) \right)^2 \tag{6.11}$$

$$\rho_0 = sinc(k_x X) sinc(k_y Y) \tag{6.12}$$

$$D = \frac{1 + cos\theta_i \cos\theta_r - \sin\theta_i \sin\theta_r \cos\phi_r}{\cos\theta_i (\cos\theta_i + \cos\theta_r)} \tag{6.13}$$

$$k_{xy} = \sqrt{k_x^2 + k_y^2} \tag{6.14}$$

and

$$k_x = k(\sin\theta_i - \sin\theta_r \cos\phi_r) \tag{6.15}$$

$$k_y = k(\sin\theta_r \sin\theta_i) \tag{6.16}$$

$$k = \frac{2\pi}{\lambda} \tag{6.17}$$

One can notice that the factor g resembles the argument of the Debye-Waller factor reported in 4.13 and indeed it represents the roughness of the surface, with three cases corresponding to smooth surface $g << 1$, moderately rough surface $g \approx 1$ and very rough surface $g >> 1$. The first term $e^{-g}\rho_0$ of the mean scattered power is the specular spike component of the specular reflection, when the surface dimensions are small, ρ_0 becomes a very sharp function of θ_i and θ_r and it is zero for all scattering

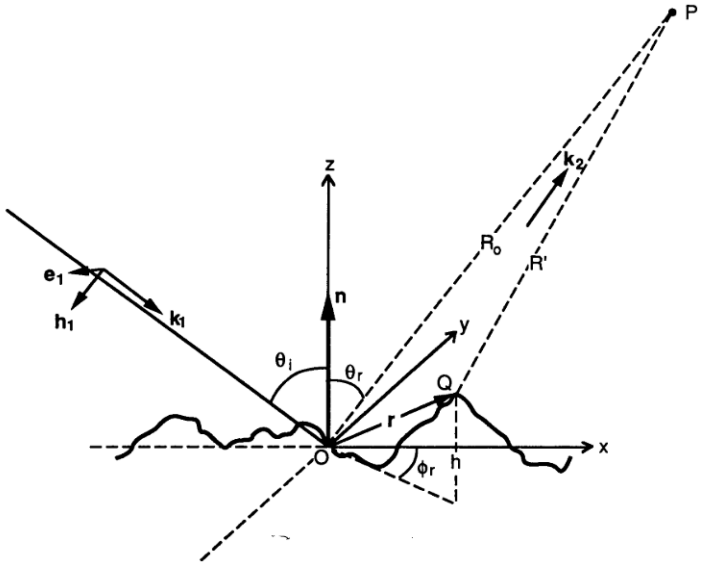

Figure 6.14: *A plane wave incident on a rough surface with propagation direction* $\boldsymbol{k}_1$ *and scattered in direction* $\boldsymbol{k}_2$*. [47]*

directions except a very narrow range around the specular direction ($\theta_r = \theta_i$).

Imagining to apply this model to our situation, further considerations are needed. Considering the dimension of the beam waists of the IR and XUV pulses, it is hard to imagine that spatial properties of the pulses have no impact on reflectance, especially when considering surface irregularities. Moreover, working with XUV and X-rays sources, Kirchoff's assumption is at its limit. All this to say that a comprehensive description of the surface interaction of a pulse with a solid interface requires careful considerations and an adequate choice of the approximations to be adopted.

Bibliography

[1] F. Krausz and M. Ivanov. "Attosecond physics". In: *Reviews of Modern Physics* 81.1 (2009), pp. 163–234. ISSN: 15390756. DOI: 10.1103/RevModPhys.81.163.

[2] I. H. Munro and N. Schwentner. "Time resolved spectroscopy using synchrotron radiation". In: *Nuclear Instruments and Methods in Physics Research* 208.1 (1983), pp. 819–834. ISSN: 0167-5087. DOI: https://doi.org/10.1016/0167-5087(83)91227-9.

[3] R. Geneaux et al. "Transient absorption spectroscopy using high harmonic generation: A review of ultrafast X-ray dynamics in molecules and solids". In: *Philosophical Transactions of the Royal Society A: Mathematical, Physical and Engineering Sciences* 377.2145 (2019). ISSN: 1364503X. DOI: 10.1098/rsta.2017.0463.

[4] P. B. Corkum. "Plasma perspective on strong field multiphoton ionization". In: *Phys. Rev. Lett.* 71 (13 Sept. 1993), pp. 1994–1997. DOI: 10.1103/PhysRevLett.71.1994.

[5] K. J. Schafer et al. "Above threshold ionization beyond the high harmonic cutoff". In: *Phys. Rev. Lett.* 70 (11 Mar. 1993), pp. 1599–1602. DOI: 10.1103/PhysRevLett.70.1599.

[6] K. C. Kulander, K. J. Schafer, and J. L. Krause. "Dynamics of Short-Pulse Excitation, Ionization and Harmonic Conversion". In: *Super-Intense Laser-Atom Physics*. Ed. by B. Piraux, A. L'Huillier, and K. Rzazewski. Vol. 316. NATO Science Series B. Springer US, 1993. ISBN: 978-1-4615-7965-6. DOI: 10.1007/978-1-4615-7963-2_10.

[7] M. Nisoli et al. "Attosecond Electron Dynamics in Molecules". In: *Chemical Reviews* 117.16 (2017). PMID: 28488433, pp. 10760–10825. DOI: 10.1021/acs.chemrev.6b00453.

[8] A. D. Shiner et al. "Wavelength Scaling of High Harmonic Generation Efficiency". In: *Phys. Rev. Lett.* 103 (7 Aug. 2009), p. 073902. DOI: 10.1103/PhysRevLett.103.073902.

[9] T. Gaumnitz et al. “Streaking of 43-attosecond soft-X-ray pulses generated by a passively CEP-stable mid-infrared driver”. In: *Opt. Express* 25.22 (Oct. 2017), pp. 27506–27518. DOI: 10.1364/OE.25.027506. URL: http://www.opticsexpress.org/abstract.cfm?URI=oe-25-22-27506.

[10] A. P. Jauho and K. Johnsen. “Dynamical Franz-Keldysh effect”. In: *Physical Review Letters* 76.24 (1996), pp. 4576–4579. ISSN: 10797114. DOI: 10.1103/PhysRevLett.76.4576. arXiv: 9512092 [cond-mat].

[11] M. Lucchini et al. “Attosecond dynamical Franz-Keldysh effect in polycrystalline diamond”. In: *Science* 353.6302 (2016), pp. 916–919. ISSN: 0036-8075. DOI: 10.1126/science.aag1268.

[12] M. Lucchini et al. “Unravelling the intertwined atomic and bulk nature of localised excitons by attosecond spectroscopy”. In: *Nature Communications* 12.1 (Feb. 2021), p. 1021. ISSN: 2041-1723. DOI: 10.1038/s41467-021-21345-7.

[13] F. Schlaepfer et al. “Attosecond optical-field-enhanced carrier injection into the GaAs conduction band”. In: *Nature Physics* 14.6 (2018), pp. 560–564. ISSN: 17452481. DOI: 10.1038/s41567-018-0069-0. URL: http://dx.doi.org/10.1038/s41567-018-0069-0.

[14] M. Schultze et al. “Controlling dielectrics with the electric field of light”. In: *Nature* 493.7430 (2013), pp. 75–78. ISSN: 00280836. DOI: 10.1038/nature11720.

[15] H. Mashiko et al. “Petahertz optical drive with wide-bandgap semiconductor”. In: *Nature Physics* 12.8 (2016), pp. 741–745. ISSN: 17452481. DOI: 10.1038/nphys3711.

[16] C. J. Kaplan et al. “Femtosecond tracking of carrier relaxation in germanium with extreme ultraviolet transient reflectivity”. In: *Phys. Rev. B* 97 (20 May 2018), p. 205202. DOI: 10.1103/PhysRevB.97.205202.

[17] G. D. Lucarelli et al. “Novel beamline for attosecond transient reflection spectroscopy in a sequential two-foci geometry”. In: *Review of Scientific Instruments* 91.5 (2020), p. 053002. DOI: 10.1063/5.0005932.

[18] B. Moio. “Design, realization and characterization of an experimental setup for Transient Reflectivity experiments”. 2018. URL: https://www.politesi.polimi.it/handle/10589/142734.

[19] G. Inzani. “Attosecond core-exciton dynamics in MgF_2”. 2019. URL: https://www.politesi.polimi.it/handle/10589/149546.

[20] M. Zavelani-Rossi and F. Vismarra. *High Intensity Lasers for nuclear and physical applications*. first. Società Editrice Esculapio s.r.l., 2020. ISBN: 978-88-9385-188-6.

[21] M. Nisoli, S. De Silvestri, and O. Svelto. "Generation of high energy 10 fs pulses by a new pulse compression technique". In: *Applied Physics Letters* 68.20 (1996), pp. 2793–2795. DOI: 10.1063/1.116609.

[22] M. Nisoli et al. "A novel-high energy pulse compression system: generation of multigigawatt sub-5-fs pulses". In: *Applied Physics B: Lasers and Optics* 65.2 (Aug. 1997), pp. 189–196. DOI: 10.1007/s003400050263.

[23] H. Mashiko et al. "Double Optical Gating of High-Order Harmonic Generation with Carrier-Envelope Phase Stabilized Lasers". In: *Phys. Rev. Lett.* 100 (10 Mar. 2008), p. 103906. DOI: 10.1103/PhysRevLett.100.103906.

[24] J. Mauritsson et al. "Attosecond Pulse Trains Generated Using Two Color Laser Fields". In: *Phys. Rev. Lett.* 97 (1 July 2006), p. 013001. DOI: 10.1103/PhysRevLett.97.013001.

[25] P. B. Corkum, N. H. Burnett, and M. Y. Ivanov. "Subfemtosecond pulses". In: *Opt. Lett.* 19.22 (Nov. 1994), pp. 1870–1872. DOI: 10.1364/OL.19.001870.

[26] F. Calegari et al. "Advances in attosecond science". In: *Journal of Physics B: Atomic, Molecular and Optical Physics* 49.6 (Feb. 2016), p. 062001. DOI: 10.1088/0953-4075/49/6/062001.

[27] H. G. Muller. "Reconstruction of attosecond harmonic beating by interference of two-photon transitions". In: *Applied Physics B: Lasers and Optics* 74.SUPPL. (2002), pp. 17–21. ISSN: 09462171. DOI: 10.1007/s00340-002-0894-8.

[28] J. Itatani et al. "Attosecond Streak Camera". In: *Physical Review Letters* 88.17 (2002), p. 4. ISSN: 10797114. DOI: 10.1103/PhysRevLett.88.173903.

[29] Y. Mairesse and F. Quéré. "Frequency-resolved optical gating for complete reconstruction of attosecond bursts". In: *Physical Review A - Atomic, Molecular, and Optical Physics* 71.1 (2005), pp. 1–4. ISSN: 10502947. DOI: 10.1103/PhysRevA.71.011401.

[30] M. Lucchini et al. "Ptychographic reconstruction of attosecond pulses". In: *Optics Express* 23.23 (2015), p. 29502. ISSN: 1094-4087. DOI: 10.1364/oe.23.029502.

[31] M. Lucchini. *Project AuDACE*. URL: http://www.audaceproject.it/. Last access: 17.07.2021.

[32] C. D. Stanciu et al. “All-Optical Magnetic Recording with Circularly Polarized Light”. In: *Phys. Rev. Lett.* 99 (4 July 2007), p. 047601. DOI: 10.1103/PhysRevLett.99.047601.

[33] C. Trovatello et al. “The ultrafast onset of exciton formation in 2D semiconductors”. In: *Nature Communications* 11.1 (Oct. 2020), p. 5277. ISSN: 2041-1723. DOI: 10.1038/s41467-020-18835-5.

[34] T. Fan et al. “Bright circularly polarized soft X-ray high harmonics for X-ray magnetic circular dichroism”. In: *Proceedings of the National Academy of Sciences* 112.46 (2015), pp. 14206–14211. ISSN: 0027-8424. DOI: 10.1073/pnas.1519666112.

[35] M. Hennes et al. “Time-Resolved XUV Absorption Spectroscopy and Magnetic Circular Dichroism at the Ni M2,3-Edges”. In: *Applied Sciences* 11.1 (2021). ISSN: 2076-3417. DOI: 10.3390/app11010325.

[36] G. P. Zhang et al. “Paradigm of the time-resolved magneto-optical Kerr effect for femtosecond magnetism”. In: *Nature Physics* 5.7 (July 2009), pp. 499–502. ISSN: 1745-2481. DOI: 10.1038/nphys1315.

[37] P. Tengdin et al. “Direct light–induced spin transfer between different elements in a spintronic Heusler material via femtosecond laser excitation”. In: *Science Advances* 6.3 (2020). DOI: 10.1126/sciadv.aaz1100.

[38] D. H. Goldstein. *Polarized light, Third Edition*. third. CRC press, 2011. ISBN: 978-1-4398-3041-3.

[39] F. L. Pedrotti, L. M. Pedrotti, and L. S. Pedrotti. *Introduction to Optics*. Pearson New International Edition. Pearson Education Limited, 2014. ISBN: 978-1-292-02256-7.

[40] J. P. Landry. “Optical oblique-incidence reflectivity difference microscopy: Application to label-free detection of reactions in biomolecular microarrays”. 2008, (Appendix B). URL: https://www.proquest.com/books/optical-oblique-incidence-reflectivity-difference/docview/20117398/se-2?accountid=28385.

[41] H. R. Phillip and E. A. Taft. “Kramers-Kronig Analysis of Reflectance Data for Diamond”. In: *Phys. Rev.* 136 (5A Nov. 1964), A1445–A1448. DOI: 10.1103/PhysRev.136.A1445.

[42] vv. aa. *Refractive Index Database*. URL: https://refractiveindex.info/. Last access: August 2021.

[43] E. D. Palik, ed. *Handbook of Optical Constants of Solids*. Boston: Academic Press, 1985. ISBN: 978-0-08-054721-3. DOI: https://doi.org/10.1016/C2009-0-20920-2.

[44] E. Gullikson. *CXRO database*. URL: https://henke.lbl.gov/optical_constants/. Last access: August 2021.

[45] D. E. Cullen et al. "Tables and graphs of photon-interaction cross sections from 10 eV to 100 GeV derived from the LLNL Evaluated Photon Data Library (EPDL)". In: (Oct. 1989). URL: https://www.osti.gov/biblio/6901928.

[46] C. J. Kaplan et al. "Retrieval of the complex-valued refractive index of germanium near the M4,5 absorption edge". In: *J. Opt. Soc. Am. B* 36.6 (June 2019), pp. 1716–1720. DOI: 10.1364/JOSAB.36.001716.

[47] S. K. Nayar, K. Ikeuchi, and T. Kanade. "Surface reflection: physical and geometrical perspectives". In: *IEEE Transactions on Pattern Analysis and Machine Intelligence* 13.7 (1991), pp. 611–634. DOI: 10.1109/34.85654.

[48] P. Beckmann and A. Spizzichino. *The scattering of electromagnetic waves from rough surfaces*. Pergamon Press, 1963.

[49] *BEAR beamline, Elettra*. URL: https://www.elettra.trieste.it/lightsources/elettra/elettra-beamlines/bear/beamline-description.html. Last access: August 2021.

[50] A. Giglia et al. "The beam position monitor of the BEAR beamline". In: *Review of Scientific Instruments* 76.6 (June 2005), p. 063111. DOI: 10.1063/1.1926907.

[51] H. Zhang et al. "High-Quality LaVO3 Films as Solar Energy Conversion Material". In: *ACS Applied Materials & Interfaces* 9.14 (2017). PMID: 28323409, pp. 12556–12562. DOI: 10.1021/acsami.6b16007.

[52] *Delaware Diamond Knives*. URL: https://ddk.com/. Last access: August 2021.

[53] M. Nisoli. *Semiconductor Photonics: Principles and Applications*. first. Società Editrice Esculapio, 2016. ISBN: 9788893850025.

[54] E. Goulielmakis et al. "Direct measurement of light waves". In: *Science* 305.5688 (2004), pp. 1267–1269. ISSN: 00368075. DOI: 10.1126/science.1100866.

[55] J. Gagnon and V. S. Yakovlev. "The direct evaluation of attosecond chirp from a streaking measurement". In: *Applied Physics B: Lasers and Optics* 103.2 (2011), pp. 303–309. ISSN: 09462171. DOI: 10.1007/s00340-010-4358-2.

[56] R. Géneaux et al. “Source noise suppression in attosecond transient absorption spectroscopy by edge-pixel referencing”. In: *Optics Express* 29.2 (2021), p. 951. ISSN: 1094-4087. DOI: 10.1364/oe.412117.

[57] M. Lucchini et al. “Attosecond timing of the dynamical Franz–Keldysh effect”. In: *JPhys Photonics* 2.2 (2020). ISSN: 25157647. DOI: 10.1088/2515-7647/ab70cb.

[58] F. Schlaepfer et al. “Gouy phase shift for annularly truncated beam profiles in attosecond pump-probe measurements”. In: *2017 Conference on Lasers and Electro-Optics, CLEO 2017 - Proceedings* 2017-Janua.4 (2017), pp. 1–2. DOI: 10.1364/CLEO_AT.2017.JTh2A.52.

[59] K. B. Nordstrom et al. “Excitonic dynamical franz-keldysh effect”. In: *Physical Review Letters* 81.2 (1998), pp. 457–460. ISSN: 10797114. DOI: 10.1103/PhysRevLett.81.457. arXiv: 9804254 [cond-mat].

[60] K. Yabana et al. “Time-dependent density functional theory for strong electromagnetic fields in crystalline solids”. In: *Physical Review B - Condensed Matter and Materials Physics* 85.4 (2012), pp. 1–11. ISSN: 10980121. DOI: 10.1103/PhysRevB.85.045134. arXiv: 1112.2291.